XENON-COPPER CHEMICAL BONDING: FOURIER TRANSFORM MICROWAVE SPECTROSCOPY OF XeCuX (X = F, Cl)

By

Julie M. Michaud

B. Sc. Honours (Chemistry) University of British Columbia, 2003

A THESIS SUBMITTED IN PARTIAL FULFILLMENT OF

THE REQUIREMENTS FOR THE DEGREE OF

MASTER OF SCIENCE

in

THE FACULTY OF GRADUATE STUDIES

DEPARTMENT OF CHEMISTRY

UNIVERSITY OF BRITISH COLUMBIA

December 2004

ABSTRACT

The rotational spectra of seven isotopomers of XeCuF and eight isotopomers of XeCuCl have been measured in the range of 7-22 GHz using a pulsed jet cavity Fourier transform microwave spectrometer. The molecules were prepared by laser ablation of a Cu metal rod with a pulsed Nd:YAG laser at 1064 nm and allowing the plasma to react with appropriate precursors (Xe and SF_6 or Cl_2) entrained in a carrier gas of Ar. Rotational constants, centrifugal distortion constants, internuclear distances, vibration frequencies, and ^{131}Xe, Cu and Cl hyperfine coupling constants have been evaluated.

The Xe-Cu bonds are short and the molecules are rigid. The ^{131}Xe nuclear quadrupole coupling constants in both XeCuF and XeCuCl are large (-87.8 and -81.4 MHz, respectively). The Cu nuclear quadrupole coupling constants differ radically from those of uncomplexed CuF and CuCl molecules.

Ab initio calculations have supported the experimental results with short NgM bonds and rigid molecules. Mulliken populations and MOLDEN plots have also been calculated and both are consistent with strong interactions between the noble gas and the noble metal. The local energy densities were calculated to be negative and indicate the presence of a covalent XeCu bond.

Both experimental and theoretical results are consistent with those reported earlier for other noble gas – noble metal halide molecules. The evidence is convincing for chemical bonding present between the noble gas and the noble metal in all NgMX molecules.

TABLE OF CONTENTS

LIST OF FIGURES

LIST OF TABLES

ACKNOWLEDGMENTS

I am truly grateful for the wonderful experiences that my graduate studies have provided me. I would like to sincerely thank my supervisor Dr. Mike Gerry for his guidance throughout the project. I have learned much from him about chemistry and about life in general. Working under his supervision has been an amazing learning experience and I wish it could continue. I hope that I will one day be such a great teacher and scientist.

I would like to express my gratitude to my colleagues. Everything I wanted to know about the spectrometer and more was taught to me by Dr. Steve Cooke. I owe much of my success to his patience with my never-ending questions. My many discussions with Dr. Steve Cooke and Dr. Christine Krumrey have helped me throughout my studies.

I would also like to thank my friends and family for their patience and support during my writing and my studies in general. Specifically I would like to thank Lesley Stoch and Berenice Tostado for always bringing a smile to my face from a distance via letters and phone calls. Also I would like to thank Magdalena Dymarska, without whom, my lunch hours would not have been so much fun. My sincere thanks go to Murray Tippett for his constant support, his proof-reading and his attempts at making dinners.

Chapter 1

Introduction

High resolution microwave spectroscopy is a very versatile technique which provides structural information about gaseous molecules. Rotational spectra are almost always the spectra measured and they contain the transitions between rotational energy levels of the molecules. The molecular geometry is the primary contributor to the spectral pattern, thus making microwave spectroscopy an excellent experimental technique for determining bond lengths and angles.

In high resolution microwave spectroscopy, the observed line widths of the spectra are very small (~ 7-10 kHz) and consequently small deviations from the basic spectral pattern can be easily seen. Accordingly several minute effects are observed and measured to a high precision. One such effect is centrifugal distortion in which the molecule distorts during molecular rotation. Centrifugal distortion gives a measure of molecular rigidity and can be related to vibrational frequencies and force constants. Hyperfine coupling is another effect which can be measured precisely in high resolution microwave spectroscopy. It occurs when the nuclear spin angular momentum couples with the molecular rotational angular momentum, with the result that the rotational levels split and several hyperfine components are measured in the spectra. The most common mechanisms in closed-shell molecules are nuclear quadrupole coupling and nuclear spin-rotation coupling. Both mechanisms provide information about the electron distribution at a particular nucleus. The dominant mechanism for nuclei with spin $I > \frac{1}{2}$ is nuclear quadrupole coupling, caused by an electric field gradient at the nucleus resulting primarily from an asymmetric electron distribution.

The versatility of high resolution microwave spectroscopy is shown by the extent of information that can be obtained from this one technique, often at the same time. This contrasts

drastically with what a traditional synthetic chemist might need to do. Using a microwave spectrometer it is possible simultaneously to:

- prepare and identify a molecule,
- measure its bond lengths and angles,
- determine vibration frequencies, and
- examine the electron distribution in the molecule.

To obtain comparable information a traditional synthetic chemist would have to use a large number of instruments including a mass spectrometer, an X-ray diffractometer, infrared and Raman spectrometers and a nuclear magnetic resonance spectrometer. The abundance of information provided by high resolution microwave spectroscopy allows for discussions about the nature of bonding in molecules and complexes.

Throughout its history, microwave spectroscopy has undergone many technological advances. Nuclear magnetic resonance (NMR) spectroscopy has had a similar history and shares many of its evolutionary steps with microwave spectroscopy. Both began as simple continuous wave absorption experiments, in which a radiation source or field is swept over ranges where transitions are expected.[1,2] When a transition occurs, radiation is absorbed by the sample and this is indicated by the detector. The continuous wave experiment is quite time consuming for high resolution experiments where the scans must be done very slowly and the frequency steps made very small. A major disadvantage of continuous wave experiments is the ability to probe only one frequency at a time. The traditional sample cell for continuous wave microwave spectroscopy is a wave guide 2-3 m in length which is filled with the gas to be studied.[1] This experiment is well suited for the study of a stable, steady-state gas.

The development of a more sensitive experiment was mandatory for the detection of the rotational spectra of ions or unstable and short-lived species. The development of microwave spectroscopy, following the earlier development of NMR spectroscopy, went towards the

possibility of measuring rotational transitions in the time domain. The first Fourier transform microwave (FTMW) experiment consisted of sending a high-power pulse of microwave radiation through the absorption cell.[3] Radiation induces a macroscopic rotational polarization of the sample molecules which decays once the radiation pulse is removed. In this case, the absorption cell remained a waveguide. Fourier transform techniques have the advantage that each pulse of radiation contains a range of excitation frequencies. With this technique (as with the continuous wave technique), the measured decay can be signal-averaged to improve the signal-to-noise ratio. These allow for high resolution measurements to be performed faster than with the continuous wave experiment since more than one frequency is probed at a time. The advantages in sensitivity and resolution of working in the time domain were illustrated by this technique; however it was not well suited for the study of transient and short-lived species.

The next major development was the introduction of the pulsed jet cavity FTMW spectrometer in 1981.[4] A similar spectrometer was used for the experiments described in this thesis. The microwave cell is a Fabry-Perot cavity with two spherical mirrors. Samples are injected entrained in supersonic jets of noble gas from a pulsed nozzle. In Flygare's original design the jets ran perpendicular to the axis of propagation of the microwaves. However, more recently it has been found that increased sensitivity and resolution can be obtained if the jet runs coaxial to the microwave propagation axis.[5] This arrangement has thus been used in the present work, in spite of the small drawback that each line is doubled by the Doppler effect.

Use of the jets has two major advantages. The first is that the expansion into the cavity is adiabatic, resulting in a cooling of the gas to a very low rotational temperature (~ 3 K).[6] Population differences between the levels are thus increased, improving the sensitivity of the spectroscopic experiment. The second is that beyond about 5 mm from the nozzle the sample molecules are in a collision-free environment. Therefore unstable species can be prepared at the

throat of the nozzle and stabilized in the jet. This means that the spectra of a whole new range of molecules can be studied.

The first samples to be observed were van der Waals complexes, where two or more species are held together by weak van der Waals bonds. Examples are Kr-HCl[7], Kr-CO_2[8], Ar-Ne-N_2O[9], and Ne-Kr.[10] Many more have been reported. Recently spectra of complexes containing many (~8) He atoms have been observed and are being used to obtain information on the nature of solvation.[11,12]

Another method of sample production, particularly from the UBC microwave spectroscopy laboratory, has involved laser ablation of a metal to prepare small gas phase metal-containing molecules.[13] It has been used in the work presented in this thesis. In this technique pulses from a Nd:YAG laser are focused through a glass window onto a metal rod located at the mouth of the nozzle. The resulting metal plasma reacts with suitable precursor(s) contained in the carrier gas of the jet (usually noble gas). The reaction products are stabilized in the jet, allowing for measurement of their rotational spectra.

Many small metal-containing molecules have been studied using this technique. Examples are ScBr[14], AlCN[15], MgBr[16], and ZrS.[17] Also studied have been noble metal halides, MX (M = Ag, Cu, Au; X = F, Cl, Br)[18,19,20,21,22,23,24] where some notable compounds were produced and characterized. Silver chloride, AgCl,[18] best known as a white precipitate in water, was easily prepared and studied in the gas phase by this method. A molecule that was long thought as being impossible to make, gold monofluoride, AuF, was easily prepared and studied by this laser ablation technique.[19]

In 1999, the spectrum of ArAgCl was accidentally discovered by Evans and Gerry.[25] Following this discovery, the spectra of ArAgF and ArAgBr[25] were also measured. When the spectra were analyzed, some interesting properties were found:

- The ArAg bond length was unusually short; and

- The centrifugal distortion constant was very small, indicating a rigid molecule.

Following this work, analogous studies of $ArCuX$[26] and $ArAuX$[27,28] were performed; the same unusual structural properties were observed. This prompted a systematic study of the spectra and structural properties of all noble gas – noble metal halides NgMX (Ng = Ar, Kr, Xe; M = Cu, Ag, Au; X = F, Cl, Br). The spectra of nineteen such complexes have been reported, with the only missing NgM combination being XeCu.[25,26,27,28,29,30,31,32,33,34] All the complexes are linear, and are rigid with short NgM bonds; in addition the following general properties have been found:

- The hyperfine structure indicates that the electron distributions on the noble gas, the metal and to a lesser extent the halogen are significantly altered on molecule formation;
- The interaction strength increases as the noble gas is changed from Ar to Kr to Xe and as the metal is changed from Ag to Cu to Au;
- Large Ng-M dissociation energies have been calculated *ab initio* which cannot be fully accounted for by induction energies;
- Other *ab initio* results are consistent with weak NgM chemical bonding.

Previous studies suggest that XeAuX molecules should have the strongest interactions. The recently studied $XeAuF$[34] demonstrates that this is indeed the case. The study showed clear evidence of very strong interactions between Xe and Au which seem consistent with XeAu chemical bonding. The interactions between Xe and Cu in XeCuX should be the next strongest after XeAuX.

This thesis presents the first measurements of the spectra and first characterization of XeCuF and XeCuCl. These are the first observed complexes with a Xe-Cu bond. For XeCuF, the spectra of seven isotopomers have been measured; for XeCuCl, the spectra of eight isotopomers have been measured. In both cases the bond lengths have been determined. In addition, hyperfine structure due to ^{131}Xe, Cu and Cl has been observed and will be included in

the discussion of the nature of the bonding between Xe and Cu. The experimental results and the discussion are presented in Chapter 4 and 5, respectively.

The theoretical modeling of noble gas – metal bonding has been attempted by several theoreticians.[35,36,37,38] Unfortunately, the reliability of the models could not be completely known because of a lack of experimental data for comparison. The studies of NgMX molecules provide experimental data for theoreticians to improve models of noble gas to metal interactions. In 2002, a theoretical study done by Lovallo and Klobukowski[37] modeled the NgMX molecules and compared the results to available experimental data. They calculated geometries and Ng-M dissociation energies of the NgMX (Ng = Ar, Kr, Xe; M = Cu, Ag, Au; X = F, Cl) molecules and their values agree well with the experimental data. Their geometries have been used as initial parameters for our spectral searches.

Noble gas-containing compounds are not very common; even rarer are those with noble gas – metal chemical bonds. UBC was home to the first noble gas compound, discovered by Neil Bartlett[39] in 1962. He hypothesized that PtF_6 could oxidize Xe since an analogous reaction between PtF_6 and O_2 yielded $[O_2]^+[PtF_6]^-$ and Xe has a lower ionization potential than O_2. This turned out to be correct and the first noble gas compound was made, this was $[XeF]^+[PtF_6]^-$. Although it was first discovered in 1962, it took almost 40 years to characterize its structure from X-ray powder diffraction.[40] The initial discovery did, regardless, spark the study of more noble gas containing compounds, and in particular Kr and Xe compounds with electronegative atoms (F, Cl, O, N, C and H).[41,42]

There are several neutral species known to contain noble gas – metal bonds. These include Ar-NaCl[43], Ng-BeO (Ng = Ar, Kr, Xe)[44], Ng-$M(CO)_5$ (Ng = Ar, Kr, Xe; M = Cr, Mo, W)[45] and crystalline type compounds like $[AuXe_4]^{2+}([Sb_2F_{11}]^-)_2$.[46,47] Ar-NaCl is clearly a weakly bound van der Waals complex.[43] The bonding in Ng-BeO and Ng-$M(CO)_5$ is stronger, but still quite weak, and is believed to have little covalent character.[48] In Ng-BeO, because the BeO is

highly polar the Be^{++} core is exposed to the electron cloud of the noble gas. The interaction can be attributed to strong induced dipole interactions.[44]

$[AuXe_4]^{2+}([Sb_2F_{11}]^-)_2$ is remarkable on two counts: it has no fewer than four XeAu bonds, and it can be prepared in sufficient quantity that its crystal structure can be determined. The $[AuXe_4]^{2+}$ ion is square planar, with r(XeAu) = 2.73-2.75 Å; *ab initio* calculations suggest a donation of ~0.4 electrons from each Xe to Au^{++}.[46] Its preparation involves using Xe as a reducing agent with the strong oxidizing agent AuF_3:[46]

$$6Xe + AuF_3 + 3H^+ \rightarrow [AuXe_4]^{2+} + 2Xe^+ + 3HF.$$

The compound is a prototype for several new compounds with AuXe bonds. Only one of these containg Au(I), namely $[(F_3As)AuXe]^+[Sb_2F_{11}]^-$.[49,50] In this ion, r(XeAu) = 2.61 Å which is 0.07 Å longer than r(XeAu) in XeAuF.[34]

This thesis will contain in Chapter 2 a brief description of the relevant theory used in the analysis of the results in this thesis. Chapter 3 details the experimental setup used for the experiments performed for this thesis. Chapters 4 and 5 present the experimental results and discussion, respectively. The theoretical studies of the NgMX molecules are presented in Chapter 6. A chapter summarizing the general picture of noble gas – noble metal halides concludes this thesis. The involved analysis in this thesis generated a large number of tables; they are collected at the end of each chapter to aid the reader. The tables of transition frequencies for each molecule studied are collected in Appendices A and B at the end of the thesis. The figures, however, are in the chapter near where they are first cited.

Chapter 2

Theory

The theory chapter summarizes some of the basic theory used to analyze the spectra and obtain the results reported in this thesis. This is presented to familiarize the reader with the notation and theory that will be used in the following chapters, this theory has not been developed as a part of this thesis.

Firstly, the theory relevant to the assignment and analysis of the pure rotational spectra of a linear molecule is discussed. This theory has been developed fully in several textbooks.[1,51] The discussion here will focus on:

a. The rigid rotor and the distortable rotor;
b. Selection rules and transition frequencies;
c. Hyperfine structure;
d. Bond length determination.

Secondly, a theoretical description of pulsed excitation experiments will be briefly given in this chapter.

2.1 Molecular Rotational Spectroscopy

The total Hamiltonian of the molecule, $\hat{H}_{total}$, is comprised of several parts of which the translational, electronic, vibrational, and rotational components are important for this thesis.[52] The Born-Oppenheimer approximation states that the electrons can be considered to respond instantaneously to changes in nuclear position because of the large mass difference between the nucleus and the electrons.[53] This approximation allows the components of the total Hamiltonian to be separated as follows:

$$\hat{H}_{total} = \hat{H}_{trans} + \hat{H}_{elec} + \hat{H}_{vib} + \hat{H}_{rot}. \qquad [2.1]$$

The separation of the total Hamiltonian permits simplification of the eigenfunctions, ψ, and eigenvalues, E, so they can be written as:

$$\Psi_{total} = \psi_{trans}\psi_{elec}\psi_{vib}\psi_{rot} \quad [2.2]$$

and:

$$E_{total} = E_{trans} + E_{elec} + E_{vib} + E_{rot}\,. \quad [2.3]$$

Only the rotational Hamiltonian and its accompanying eigenfunctions and eigenvalues are discussed here.

2.1.1 The Rigid Rotor

A starting point for approximating the rotational energy levels is obtained by assuming molecules are rigid rotors. This approximation models molecules as point masses connected by massless rigid rods.

The molecules discussed in this thesis have a $^1\Sigma$ electronic ground state and thus have no unbalanced electronic angular momentum.[54] For these types of molecules with no nuclear coupling, the angular momentum results solely from the end-over-end rotation of the molecule.

Classically, the molecular rotation of rigid bodies is described using these equations:[55]

$$\vec{L} = \sum_i \vec{r}_i \times \vec{p}_i \quad [2.4]$$

and

$$\vec{v}_i = \vec{\omega} \times \vec{r}_i\,. \quad [2.5]$$

The total angular momentum of the molecule is represented by $\vec{L}$; the molecule's angular velocity (which is constant for all atoms in the molecule) is denoted by $\vec{\omega}$. The position of the i^{th} atom with respect to the centre of mass is denoted by $\vec{r}_i$, its linear momentum is $\vec{p}_i$, and its linear velocity is $\vec{v}_i$. For simplicity, the coordinates of the centre of mass are $(x,y,z) = (0,0,0)$. By substituting linear velocity from equation [2.5] in the equation for linear momentum, the following equation is obtained:

$$\vec{p}_i = m_i\vec{v}_i = m_i\vec{\omega} \times \vec{r}_i\,. \quad [2.6]$$

Inserting equation [2.6] into equation [2.4] yields:

$$\vec{L} = \sum_i m_i \vec{r}_i \times (\vec{\omega} \times \vec{r}_i) . \qquad [2.7]$$

Using the trigonometric identity $A \times (B \times C) = B(A \bullet C) - C(A \bullet B)$ and expanding into vector components, equation [2.7] can be expressed in matrix form as:

$$\begin{pmatrix} L_x \\ L_y \\ L_z \end{pmatrix} = \begin{pmatrix} \sum_i m_i (y_i^2 + z_i^2) & -\sum_i m_i x_i y_i & -\sum_i m_i x_i z_i \\ -\sum_i m_i y_i x_i & \sum_i m_i (x_i^2 + z_i^2) & -\sum_i m_i y_i z_i \\ -\sum_i m_i z_i x_i & -\sum_i m_i z_i y_i & \sum_i m_i (x_i^2 + y_i^2) \end{pmatrix} \begin{pmatrix} \omega_x \\ \omega_y \\ \omega_z \end{pmatrix} \qquad [2.8]$$

which can simplify to:

$$\vec{L} = \begin{pmatrix} I_{xx} & I_{xy} & I_{xz} \\ I_{xy} & I_{yy} & I_{yz} \\ I_{xz} & I_{yz} & I_{zz} \end{pmatrix} \vec{\omega} = \underline{\underline{I}} \vec{\omega} . \qquad [2.9]$$

The 3×3 matrix in equation [2.9] is known as the inertia tensor. The moments of inertia are the diagonal matrix elements (I_{ff}), while the products of inertia are the off-diagonal elements (I_{fg}). The principal moments of inertia are the diagonal elements obtained when the inertia tensor is diagonalized.

For linear polyatomic molecules, such as those studied in this thesis, the principal moment of inertia about the molecular bond axis is zero ($I_{zz} = 0$) and the two remaining moments of inertia about the two axes orthogonal to the bond are equal ($I_{xx} = I_{yy} = I$). Thus the inertia tensor for a linear molecule reduces to a scalar and the angular momentum is written as:

$$\vec{L} = I\vec{\omega} \qquad [2.10]$$

where:

$$I = \sum_i m_i r_i^2 . \qquad [2.11]$$

The rotational kinetic energy in a classical treatment is given by:

$$E_{rot} = \frac{1}{2} I\omega^2 . \qquad [2.12]$$

By solving equation [2.10] for $\vec{\omega}$ and substituting the result into equation [2.12], the rotational kinetic energy becomes:

$$E_{rot} = \frac{L^2}{2I} . \qquad [2.13]$$

Several textbooks cover the conversion of the classical treatment into a quantum mechanical one[1,51,55] and so only the results will be presented here. The Hamiltonian operator is:

$$\hat{H}_{rot} = \frac{\hat{J}^2}{2I} = -\frac{\hbar^2}{2I}\nabla^2 \qquad [2.14]$$

where ∇^2 is the Laplacian operator. The eigenfunctions of the rotational Hamiltonian in equation [2.14] are the spherical harmonics, $Y_{JM}(\theta,\phi)$, with J = 0, 1, 2, ... and M = -J, -J+1, ..., J. The eigenvalues are given by:

$$E_{rot} = \frac{\hbar^2}{2I} J(J+1) = BJ(J+1) \qquad [2.15]$$

where B, the rotational constant, is:

$$B = \frac{\hbar^2}{2I} = \frac{\hbar^2}{8\pi^2 I}(Joules) = \frac{h}{8\pi^2 I}(Hz) . \qquad [2.16]$$

In microwave spectroscopy, the rotational constant is normally given in MHz.

2.1.2 The Distortable Rotor

The rigid rotor approximation gives a good description of the molecular rotational energy levels. However, this approximation, though a good one, is flawed because molecules are not rigidly bonded; the bonds are flexible and spring-like. This flexibility results in distortions due to centrifugal forces as the molecule rotates. The distortions change the moment of inertia and, consequently, the rotational constant. This is accounted for by the addition of centrifugal

distortion terms into the rotational energy Hamiltonian in equation [2.14]. For linear molecules, $\hat{H}$ becomes:[55]

$$\hat{H} = \hat{H}_{rot} + \hat{H}_{distort} = B\hat{J}^2 - D\hat{J}^4 + H\hat{J}^6 - \ldots \quad [2.17]$$

where D and H are quartic and sextic centrifugal distortion constants, respectively. The centrifugal distortion constants are generally several orders of magnitude smaller than the rotational constant. The eigenfunctions from the rigid rotor remain effectively constant even after correcting for distortions and the eigenvalues become:

$$E_{rot} = BJ(J+1) - DJ^2(J+1)^2 + HJ^3(J+1)^3 - \ldots . \quad [2.18]$$

In the present work only the quartic term was needed, and the remaining terms will be ignored. In this case the distortion of the molecule increases with roughly the square of the quantum number J. To calculate these constants, rotational transitions must be measured in at least two J-transitions.

For a diatomic molecule, the centrifugal distortion constant, D, can be related to the vibrational stretching frequency of the bond, ω:[56]

$$D = \frac{16B^3\pi^2\mu c^2}{k} = \frac{4B^3}{\omega^2} \quad [2.19]$$

where μ is the reduced mass of the molecule, c is the velocity of light and k is the force constant of the bond. The Kratzer relationship is yielded when equation [2.19] is solved for ω:[55]

$$\omega = \sqrt{\frac{4B^3}{D}} . \quad [2.20]$$

From the stretching frequency, the mass independent force constant, k, can be determined from the following equation:

$$\omega = \frac{1}{2\pi}\sqrt{\frac{k}{\mu}} . \quad [2.21]$$

2.1.3 Selection Rules and Transition Frequencies

Spectroscopic selection rules determine which transitions are allowed and are derived from time-dependent perturbation theory because of the time-dependent nature of the transitions.[57] The time-dependent Schrödinger equation:

$$\hat{H}\Psi = i\hbar\frac{\partial\Psi}{\partial t} \qquad [2.22]$$

where Ψ is an eigenfunction. If $\hat{H}$ is time-independent, then:

$$\Psi_n(r,t) = \psi_n e^{-iE_n t/\hbar} \qquad [2.23]$$

and

$$\hat{H}\psi_n(r) = E_n\psi_n(r); \qquad [2.24]$$

thus the system can be in a state described by $\psi_n(r)$ and $\Psi_n^*\Psi_n = \psi_n^*\psi_n$ would be time-independent. These $\psi_n(r)$ states are stationary states[57] which can be understood as isolated states.

When a molecule interacts with electromagnetic radiation, the Hamiltonian becomes:[57]

$$\hat{H} = \hat{H}_o + \hat{H}^{(1)} = \hat{H}_o - \hat{\mu}\cdot E_o\cos\omega t \qquad [2.25]$$

where $\hat{H}_o$ is the time-independent Hamiltonian of the isolated molecule, $\hat{\mu}$ is the electric dipole moment operator, E_o is the amplitude of the electric field contained in the microwave radiation of angular velocity ω. The time-dependent term, the $\hat{H}^{(1)}$ term in the above equation, can allow transitions from one stationary state to another.[57] Application of time-dependent perturbation theory shows that for a transition to be allowed between two energy levels the "transition moment" must be non zero. For electric dipole transitions between two states $|J,M\rangle$ and $|J',M'\rangle$ of a linear molecule this is given by:

$$(\mu_z)_{J,M;J',M'} = \mu_o \int_0^{2\pi} d\phi \int_0^{\pi} \sin\theta Y_{J',M'}(\theta,\phi)^* Y_{J,M}(\theta,\phi). \quad [2.26]$$

where the spherical harmonics are denoted as $Y_{J,M}(\theta,\phi)$, and μ_o is the permanent dipole moment of the molecule. The radiation is assumed to be polarized in the z-direction. The first requirement for an allowed transition is a nonzero permanent dipole moment. To obtain the selection rules for J and M, the spherical harmonics should be written in terms of their associated Legendre functions, $P_J^{|M|}(\cos\theta)$:[56]

$$Y_{J,M}(\theta,\phi) = N_{JM} P_J^{|M|}(\cos\theta) e^{iM\phi} \quad [2.27]$$

where N_{JM} is a normalization constant. When the spherical harmonics are replaced in equation [2.26], the following equation is obtained:

$$(\mu_z)_{J,M;J',M'} = \mu_o N_{JM} N_{J'M'} \int_0^{2\pi} d\phi e^{i(M-M')\phi} \int_{-1}^{1} d\cos\theta \cdot \cos\theta P_{J'}^{|M'|}(\cos\theta) P_J^{|M|}(\cos\theta). \quad [2.28]$$

The integral can be evaluated generally by the following relationship:[56]

$$(2J+1)\cos\theta P_J^{|M|}(\cos\theta) = (J-|M|+1)P_{J+1}^{|M|}(\cos\theta) + (J+|M|)P_{J-1}^{|M|}(\cos\theta). \quad [2.29]$$

The integral in equation [2.28] becomes:

$$(\mu_z)_{J,J',M} = 2\pi\mu_o N_{JM} N_{J'M} \int_{-1}^{1} d\cos\theta P_{J'}^{|M|}(\cos\theta) \left[\frac{(J-|M|+1)}{2J+1} P_{J+1}^{|M|}(\cos\theta) + \frac{(J-|M|)}{2J+1} P_{J-1}^{|M|}(\cos\theta) \right]. \quad [2.30]$$

The integral no longer depends on the change in M state, therefore the selection rule for M is $\Delta M = 0$.

To obtain the selection rule for J, the orthogonality of $P_J^M(x)$ must be considered. It is proportional to the Kroenecker delta (δ_{ij}):[56]

$$\delta_{ij} = \begin{cases} 1 \Rightarrow i = j \\ 0 \Rightarrow i \neq j \end{cases}. \quad [2.31]$$

The integral vanishes unless $J' = J + 1$ or $J' = J - 1$. Therefore, the selection rule for J is $\Delta J = \pm 1$.

Recapping, for the pure rotational transition to occur, the molecule must possess three properties:

- a permanent dipole moment;
- $\Delta J = \pm 1$; and
- $\Delta M = 0$.

When a transition from one state to another occurs, the energy of the photon that is absorbed (or emitted) equals the difference in the energies of the two states.[57] This statement corresponds to the Bohr frequency condition.

The transition frequencies in a rigid rotor spectrum correspond to the energy difference between two successive J-levels, following the selection rule $\Delta J = \pm 1$, is expressed as:

$$\Delta E_{rot} = 2B(J+1) \qquad [2.32]$$

where J is the rotational quantum number of the lower level involved in the transition. The simple spectrum is thus a comb of lines, each adjacent line separated by twice the rotational constant.

Centrifugal distortion is measured in the spectrum as a lowering of the transition frequency expected from the rigid rotor approximation.[57] The simple spectrum is a comb of lines where the separation between the lines is ~2B but the separation decreases with increasing J values. For a distortable rotor, the energy of the photon would follow:

$$E_{J+1} - E_J = 2B(J+1) - 4D(J+1)^3 \qquad [2.33]$$

and the spectrum would correspond to the comb of lines described in the previous section.

2.2 Hyperfine Structure

Coupling of the rotational angular momentum of the molecule with the spins of the nuclei composing the molecule can split the rotational levels into hyperfine levels. The spectrum shows this as splittings of the transitions into several hyperfine components.

Hyperfine interactions refer to interactions involving nuclear spin angular momentum, $\boldsymbol{I}$. The nuclear spin angular momentum couples to the total rotational angular momentum, $\boldsymbol{J}$, to form the total angular momentum, $\boldsymbol{F}$:

$$\boldsymbol{I} + \boldsymbol{J} = \boldsymbol{F}. \qquad [2.34]$$

Values of F are restricted to:

$$F = J + I, J + I - 1, J + I - 2, \ldots, |J - I|. \qquad [2.35]$$

Nuclear hyperfine interactions occur via electric and magnetic processes. In this thesis, two hyperfine mechanisms affect the spectra measured:

- Nuclear electric quadrupole coupling;
- Magnetic nuclear spin-rotation coupling.

Each will be discussed in turn.

2.2.1 Nuclear Electric Quadrupole Coupling

A quadrupolar nucleus has a spin I greater than ½ and possesses a nuclear electric quadrupole moment eQ. The nuclear electric quadrupole moment can interact with the electric charge distribution around the nucleus. In the case of a spherically symmetric electric charge distribution around the nucleus, such as with an isolated noble gas atom, there is no preferred orientation of the quadrupolar nuclei and thus no interaction energy. However, if the spherically symmetric charge distribution is distorted when a chemical bond is formed or through weak van der Waals interactions, the quadrupolar nucleus will try to orient itself in the electric field gradient caused by external charges (usually electrons). Molecular rotation causes the field gradient to change constantly, resulting in the coupling of the rotational and nuclear spin angular

momentum to produce the total angular momentum, $\boldsymbol{F}$. The different orientations of the quadrupolar nucleus result in different energies. Transitions between the hyperfine levels are governed by the additional selection rule of $\Delta F = 0,\pm 1$.

The theory of nuclear electric quadrupole coupling has been presented in detail by several scientists including Zare,[58] Edmonds,[59] Gordy and Cook,[1] Cook and de Lucia,[60] and Slichter.[61] The important results will be given in this section.

In Cartesian tensor form, the quadrupolar Hamiltonian is expressed as:[1]

$$\hat{H}_{Quad.} = \sum_{i=1}^{N} \hat{V}_i : \hat{Q}_i \qquad [2.36]$$

with the summation being for all coupling nuclei. This Hamiltonian may be expressed as the product of two second-rank spherical tensors:[1]

$$\hat{H}_{Quad.} = \sum_{i=1}^{N} \hat{V}(i) \cdot \hat{Q}(i) \qquad [2.37]$$

where $\hat{V}(i)$ and $\hat{Q}(i)$ are the electric field gradient and nuclear quadrupole tensors of the i^{th} nucleus respectively. These tensor operators are irreducible meaning they transform under rotation like spherical harmonics.

The use of irreducible tensor operators simplifies the calculation of matrix elements between states with definite angular momentum. The matrix elements can be separated into geometrically and physically dependent terms. For example, a basis $|\tau JM\rangle$ where J and M represent the quantum numbers associated with $\hat{J}^2$ and $\hat{J}_z$, and τ refers to all other observables, the Wigner-Eckart theorem[58,59] can be used to determine the matrix elements of the irreducible tensor operator, $T_q^{(k)}$ ($q = k, k\text{-}1, \ldots, -k$), of rank k:

$$\left\langle \tau' J' M' \left| T_q^{(k)} \right| \tau JM \right\rangle = (-1)^{J'-M'} \begin{pmatrix} J' & k & J \\ -M' & q & M \end{pmatrix} \left\langle \tau' J' \left\| T^{(k)} \right\| \tau J \right\rangle \qquad [2.38]$$

where the symbol in parentheses is a 3j symbol, which can be related to the Clebsh-Gordan coefficients and thus to the geometry of the molecule. The $\left\langle \tau' J' \left\| T^{(k)} \right\| \tau J \right\rangle$ term is the reduced matrix element of $T_q^{(k)}$ and represents the physically dependent term.

When two commuting tensor operators, $T^{(k)}$ and $U^{(k)}$, act on two subsystems in which $U^{(k)}$ acts on subsystem 1 and $T^{(k)}$ acts on subsystem 2, then the scalar product of these two tensors in the coupled basis, $\hat{J} = \hat{j}_1 + \hat{j}_2$, is given by:

$$\left\langle \tau_1' j_1' \tau_2' j_2' J' M' \left| T^{(k)} \cdot U^{(k)} \right| \tau_1 j_1 \tau_2 j_2 J M \right\rangle = \delta_{JJ'} \delta_{MM'} (-1)^{j_1 + j_2 + J'} \begin{Bmatrix} J & j_2' & j_1' \\ k & j_1 & j_2 \end{Bmatrix} \cdot \left\langle \tau_1' j_1' \left\| T^{(k)} \right\| \tau_1 j_1 \right\rangle \left\langle \tau_2' j_2' \left\| U^{(k)} \right\| \tau_2 j_2 \right\rangle \quad [2.39]$$

where the term in braces is a 6j symbol and the $\left\langle \tau_1' j_1' \left\| T^{(k)} \right\| \tau_1 j_1 \right\rangle$ and $\left\langle \tau_2' j_2' \left\| U^{(k)} \right\| \tau_2 j_2 \right\rangle$ factors express the reduced matrix elements of $T^{(k)}$ and $U^{(k)}$.

The Hamiltonian in equation [2.37] will be used to calculate the matrix elements for coupling by one, two and three nuclei.

2.2.1.1 Quadrupole Coupling by a Single Nucleus in a Rotating Molecule

When a single quadrupolar nucleus couples to the rotational angular momentum, the coupling scheme is given by equation [2.34].

$$\mathbf{I + J = F.} \quad [2.34]$$

For a single quadrupolar nucleus, the matrix elements of the Hamiltonian in equation [2.34] are given by:[1]

$$\left\langle \tau' J' I F \left| \hat{V}^{(2)} \cdot \hat{Q}^{(2)} \right| \tau J I F \right\rangle = (-1)^{J+I+F} \begin{Bmatrix} F & I & J' \\ 2 & J & I \end{Bmatrix} \left\langle \tau' J' \left\| V^{(2)} \right\| \tau J \right\rangle \left\langle I \left\| Q^{(2)} \right\| I \right\rangle \quad [2.40]$$

where the reduced matrix elements can be related to spectroscopic observables. The quadrupole moment, Q, is given by:[1]

$$\frac{1}{2}eQ = \langle I, M_I = I | Q^{(2)}_{q=0} | I, M_I = I \rangle \qquad [2.41]$$

which can be written as:

$$\langle I \| Q^{(2)} \| I \rangle = \frac{1}{2}eQ \begin{pmatrix} I & 2 & I \\ -I & 0 & I \end{pmatrix}^{-1}. \qquad [2.42]$$

The electric field gradient (in a space-fixed axis system), $q_{J'J}$, is given by:[1]

$$\frac{1}{2}q_{J'J} = \langle \tau', J', M'_J = J | V^{(2)}_o | \tau, J, M_J = J \rangle \qquad [2.43]$$

which can be written as:

$$\langle \tau', J' \| V^{(2)} \| \tau, J \rangle = \frac{1}{2}q_{J'J} \begin{pmatrix} J & 2 & J' \\ J & 0 & -J \end{pmatrix}^{-1}. \qquad [2.44]$$

By combining equation [2.40], [2.42] and [2.44], the general form of the quadrupolar Hamiltonian is obtained:[1]

$$\langle J' IF | \hat{H}_{Quad.} | JIF \rangle = \frac{(-1)^{J+I+F}}{4} \begin{pmatrix} J & 2 & J' \\ J & 0 & -J \end{pmatrix}^{-1} \begin{pmatrix} I & 2 & I \\ -I & 0 & I \end{pmatrix}^{-1} \begin{Bmatrix} F & I & J' \\ 2 & J & I \end{Bmatrix} eQq_{J'J} \qquad [2.45]$$

where $eQq_{J'J}$ for a linear molecule can be converted from a space-fixed axis system to a molecule-fixed axis system (eQq) by:

$$eQq_{J'J} = (-1)^J \sqrt{(2J+1)(2J'+1)} \begin{pmatrix} J & 2 & J' \\ J & 0 & -J \end{pmatrix} \begin{pmatrix} J & 2 & J' \\ 0 & 0 & 0 \end{pmatrix} eQq. \qquad [2.46]$$

The first-order quadrupole coupling energy for a single coupling nucleus in a linear molecule is given by:[1]

$$E_Q = -eQq \frac{3C(C+1) - 4I(I+1)J(J+1)}{8(2J-1)(2J+3)I(2I-1)}. \qquad [2.47]$$

where C = F(F+1) – J(J+1) – I(I+1).

The quadrupole coupling energies are proportional to the product of the nuclear quadrupole moment and the field gradient. The field gradient is a measure of the asymmetry of

the charge distribution at the nucleus: a highly asymmetric distribution produces a large field gradient, and for a spherically symmetric distribution, the field gradient vanishes to zero.

2.2.1.2 Quadrupole Coupling by Two Nuclei in a Rotating Molecule

When two nuclei have spins greater than ½ in a molecule, the rotational hyperfine structure is quite complicated.

The simplest two nuclei case, and the one described here, occurs when the coupling by one nucleus is much larger than the other. This is the so-called "series" coupling scheme:

$$\mathbf{J} + \mathbf{I}_1 = \mathbf{F}_1$$

$$\mathbf{F}_1 + \mathbf{I}_2 = \mathbf{F}. \qquad [2.48]$$

Each coupling nucleus has different matrix elements. To calculate the matrix elements for the first nucleus, equation [2.45] is used by replacing I with I_1 and F with F_1 to give:[1]

$$\left\langle J' I_1 F_1 \left| \hat{H}_Q(1) \right| J I_1 F_1 \right\rangle = \frac{(-1)^{J+I_1+F_1}}{4} \begin{pmatrix} J & 2 & J' \\ J & 0 & -J \end{pmatrix}^{-1} \begin{pmatrix} I_1 & 2 & I_1 \\ -I_1 & 0 & I_1 \end{pmatrix}^{-1} \begin{Bmatrix} F_1 & I_1 & J' \\ 2 & J & I_1 \end{Bmatrix} eQq_{J'J}(1) \qquad [2.49]$$

The complete quadrupolar Hamiltonian is the sum of the separate quadrupolar Hamiltonians for each nucleus:

$$\hat{H}_{Quad.} = \hat{H}_Q(1) + \hat{H}_Q(2) = \hat{V}(1) \cdot \hat{Q}(1) + \hat{V}(2) \cdot \hat{Q}(2). \qquad [2.50]$$

The matrix elements for the second quadrupolar nuclei are given by:[1]

$$\left\langle J' I_1 F_1' I_2 F \left| \hat{H}_Q(2) \right| J I_1 F_1 I_2 F \right\rangle = \frac{(-1)^{J'+I_1+I_2+2F_1+F}}{4} \begin{pmatrix} J & 2 & J' \\ J & 0 & -J \end{pmatrix}^{-1} \begin{pmatrix} I_2 & I_2 & 2 \\ I_2 & -I_2 & 0 \end{pmatrix}^{-1} \times \begin{Bmatrix} J' & F_1 & I_1 \\ F_1 & J & 2 \end{Bmatrix} \begin{Bmatrix} F & I_2 & F_1 \\ 2 & F_1 & I_2 \end{Bmatrix} eQq_{J'J}(2) \qquad [2.51]$$

The nuclear quadrupole coupling constants in equations [2.49] and [2.51] can be transformed into the molecular-fixed axis system using equation [2.46].

2.2.1.3 Quadrupole Coupling by Three Nuclei in a Rotating Molecule

When a molecule contains three nuclei contributing to the quadrupole coupling, the hyperfine structure of the spectra is very complex.

The coupling scheme used in this thesis for a three nuclei molecule with spins I_1, I_2 and I_3 is:

$$\begin{aligned} \boldsymbol{F_1} &= \boldsymbol{I_1} + \boldsymbol{J} \\ \boldsymbol{F_2} &= \boldsymbol{I_2} + \boldsymbol{F_1} \\ \boldsymbol{F} &= \boldsymbol{I_3} + \boldsymbol{F_2}. \end{aligned} \qquad [2.52]$$

The full quadrupole Hamiltonian for this system is:[60]

$$\hat{H}_{Quad.} = \hat{H}_Q(1) + \hat{H}_Q(2) + \hat{H}_Q(3) = \hat{V}(1)\cdot\hat{Q}(1) + \hat{V}(2)\cdot\hat{Q}(2) + \hat{V}(3)\cdot\hat{Q}(3). \qquad [2.53]$$

Again the matrix elements for each coupling nucleus need to be determined separately. The matrix elements for the first coupling nucleus are the same as in equation [2.49]. To calculate the matrix elements for the second coupling nucleus, F in equation [2.51] is replaced with F_2:[60]

$$\left\langle J' I_1 F_1' I_2 F_2 \left| \hat{H}_Q(2) \right| J I_1 F_1 I_2 F_2 \right\rangle = \frac{(-1)^{J'+I_1+I_2+2F_1+F_2}}{4} \sqrt{(2F_1+1)(2F_1'+1)} \begin{pmatrix} J & 2 & J' \\ J & 0 & -J \end{pmatrix}^{-1} \times \begin{pmatrix} I_2 & I_2 & 2 \\ I_2 & -I_2 & 0 \end{pmatrix}^{-1} \begin{Bmatrix} J' & F_1 & I_1 \\ F_1 & J & 2 \end{Bmatrix} \begin{Bmatrix} F_2 & I_2 & F_1 \\ 2 & F_1 & I_2 \end{Bmatrix} eQq_{J'J}(2) \qquad [2.54]$$

The matrix elements for the third nucleus are given by:[60]

$$\left\langle J' I_1 F_1' I_2 F_2' I_3 F \left| \hat{H}_Q(3) \right| J I_1 F_1 I_2 F_2 I_3 F \right\rangle = \frac{(-1)^{J'+I_1+I_2+I_3+F_1+F_1'+2F_2+F}}{4} \begin{pmatrix} J & 2 & J' \\ J & 0 & -J \end{pmatrix}^{-1} \begin{pmatrix} I_3 & 2 & I_3 \\ -I_3 & 0 & I_3 \end{pmatrix}^{-1} \sqrt{(2F_1+1)(2F_1'+1)(2F_2+1)(2F_2'+1)} \begin{Bmatrix} J' & F_1' & I_2 \\ F_1 & J & 2 \end{Bmatrix} \begin{Bmatrix} F_1' & F_2' & I_2 \\ F_2 & F_1 & 2 \end{Bmatrix} \begin{Bmatrix} F & I_3 & F_2' \\ 2 & F_2 & I_3 \end{Bmatrix} eQq_{J'J}(3) \qquad [2.55]$$

Once again the space-fixed axis nuclear quadrupole coupling constants can be converted into molecule-fixed axis nuclear quadrupole coupling constants using equation [2.46].

2.2.2 Nuclear Spin-Rotation Coupling

Nuclear spin-rotation coupling is a magnetic effect and can occur in closed shell molecules with any nucleus having a magnetic moment (i.e. $I \geq ½$).[62] Generally the spin-rotation coupling is a smaller energy interaction than nuclear quadrupole coupling, and a first-order treatment suffices.

The magnetic field components along the nuclear rotational angular momentum, J, originate from two mechanisms: the rotation of the molecule as a rigid charge distribution and less directly, but more importantly, failure of the electrons to follow the molecular frame creating rotationally dependent magnetic fields. Following the development of this theory from Gordy and Cook, the spin-rotation Hamiltonian has the form:[1]

$$H_{RS} = C_{J,i}\boldsymbol{I}\cdot\boldsymbol{J} \qquad [2.56]$$

where:

$$C_{J,i} = \frac{1}{J(J+1)} \sum_{g=x,y,z} C_{gg} \left\langle J,i \middle| J_g^2 \middle| J,i \right\rangle \qquad [2.57]$$

and:

$$C_{gg} = -g_N \mu_N h_{gg} \qquad [2.58]$$

where g_N is the dimensionless gyromagnetic ratio, μ_N is the nuclear magneton and h_{gg} is the component of magnetic field along the gg axis. The $\boldsymbol{I}\cdot\boldsymbol{J}$ term can have the following expression:

$$\boldsymbol{I}\cdot\boldsymbol{J} = \frac{1}{2}(\boldsymbol{F}^2 - \boldsymbol{I}^2 - \boldsymbol{J}^2) \qquad [2.59]$$

The spin-rotation coupling energy is given by:[1]

$$E_{SR} = \frac{C_{J,i}}{2}\left[F(F+1) - I(I+1) - J(J+1)\right] \qquad [2.60]$$

where $C_{J,i}$ is now:[44]

$$C_{J,i} = \frac{1}{J(J+1)}\left\langle J,i\left|C_{xx}J_x^2 + C_{yy}J_y^2 + C_{zz}J_z^2\right|J,i\right\rangle. \qquad [2.61]$$

For linear molecules in $^1\Sigma$ electronic states and the ground vibrational state, there is no resultant angular momentum about the molecular axis (the z inertial axis). Therefore $C_{xx} = C_{yy} = C_I$ and equation [2.61] becomes:[1]

$$C_J = \frac{1}{J(J+1)}\left\langle J\left|J^2\right|J\right\rangle = C_I\frac{J(J+1)}{J(J+1)} = C_I. \qquad [2.62]$$

The spin-rotation coupling energy for a linear molecule is:[1]

$$E_{SR} = \frac{C_I}{2}\left[F(F+1) - I(I+1) - J(J+1)\right] \qquad [2.63]$$

where C_I is the nuclear magnetic spin-rotation coupling constant.

2.3 Bond Length Determination

The measured transition frequencies are fit by least squares using Pickett's global least-squares fitting program SPFIT[63] to the spectroscopic constants (rotational, centrifugal distortion and hyperfine coupling constants). The high resolution of the spectrometer allows very precise determination of these constants. From the rotational constants and equations [2.11] and [2.16], the molecular geometries can be determined. Because the NgMX are linear, the NgM and MX bond lengths are the only parameters to be determined. For linear triatomics such as the molecules studied in this thesis, only one rotational constant can be obtained for a given isotopomer. The spectra and rotational constants for more than one isotopomer must be obtained to determine the two bond lengths needed. Also, least squares fitting can be used to obtain more precise geometries if the rotational constants of several isotopomers are measured.

Ideally, the measured rotational constants would be those at the potential minimum and the reported geometry would be the isotopically independent equilibrium (r_e) geometry. Unfortunately, molecules cannot exist at the potential minimum. If rotational transitions are

measured in two or more vibrational levels, the equilibrium rotational constants can be calculated using:[64]

$$B_v = B_e - \alpha_e(v+1/2) + \ldots \qquad [2.64]$$

Unfortunately, all the transitions measured in the spectra of NgMX molecules have been of the ground vibrational state only and the geometries in this state vary slightly with isotopomer. When this variation is ignored, the geometry obtained by least fit squares is the ground state effective (r_o) structure.

The isotopic variation can be partially accounted for by using the following equation for the ground state moments of inertia (I_o):[65]

$$I_o = I_{rigid}(r_{I\varepsilon}) + \varepsilon \qquad [2.65]$$

where I_{rigid} is an approximation to the equilibrium moment of inertia and ε is an additional fitting parameter in the least squares fit. The $r_{I\varepsilon}$ geometry is obtained from equation [2.65] and is believed to be a better approximation to the equilibrium values than the r_o values. Unfortunately, an isotopic dependence remains with ε.

In 1999, Watson *et al.*[66] developed the mass-dependent (r_m) geometries by accounting for the isotopic dependence of ε in the following equation for the ground state moments of inertia:

$$I_o = I_{rigid}(r_m) + cI_{rigid}^{1/2} + d\left[\frac{m_1 m_2 m_3}{m_1 + m_2 + m_3}\right]^{1/4} \qquad [2.66]$$

where c and d are fitting parameters and m_1, m_2 and m_3 are the masses of the atoms. The $r_m^{(1)}$ structures are obtained by setting $d = 0$ and fitting to the bond lengths and c. When the fit includes d also, the $r_m^{(2)}$ geometries are obtained. The $r_m^{(2)}$ bond lengths are believed to provide the most reliable approximation to the equilibrium geometry from ground state data alone.[66]

2.4 Pulsed Excitation Experiments: A Theoretical Description

The interaction of an ensemble of molecular dipoles with a microwave pulse and the transient effects of such a pulse on the system will be discussed in this section. The effects of the radiation power are rapidly oscillating superposition states and significant oscillation in the populations of the stationary states.[67,68] When a sample is irradiated with a microwave pulse of correct strength and duration, a macroscopic dipole moment is induced which oscillates in time. When the pulse is removed, microwave radiation is emitted at the rotational transition frequencies of the sample. The intensity of the emitted radiation decays as the macroscopic dipole moment decreases; the latter results from a removal of the coherence in the system as well as from molecular collisions.

These phenomena are best described using "optical Bloch equations" equivalent to those used in NMR.[69] Detailed derivations have been given by Flygare,[67,68] Shoemaker,[70] and Dreizler.[71] This section will provide some simple derivations and important results.

To derive Bloch equations, time-dependent Schrödinger theory in a density matrix formalism is an appropriate description.[71] The time-dependent Hamiltonian, introduced in section 2.1.3, is:

$$\hat{H}(t) = \hat{H}_o + \hat{H}^{(1)}(t) \qquad [2.25]$$

where $\hat{H}_o = \hat{H}_{rot}$, the time-independent rotational Hamiltonian and $\hat{H}^{(1)}(t)$, also from section 2.1.3, is a perturbation Hamiltonian for the interaction of the system with an external time-dependent electric field:[71]

$$\hat{H}^{(1)}(t) = -\hat{\mu}E_o \cos\omega t \qquad [2.25]$$

where $\hat{\mu}$ is the dipole moment operator and $E_o \cos\omega t$ expresses the time-dependent electric field.

It should be noted that the microwave radiation frequency v ($= \omega/2\pi$), is not necessarily resonant with the rotational transition frequency.

The space (q) and time (t) dependent wave functions for a two-level particle is:[71]

$$\Psi_v(q,t) = C_{v1}(t)\psi_1(q) + C_{v2}(t)\psi_2(q) \qquad [2.67]$$

where v designates the v^{th} particle, $C_{v1}(t)$ and $C_{v2}(t)$ are time-dependent coefficients. The functions $\psi_1(q)$ and $\psi_2(q)$ are solutions of:

$$\hat{H}_o\psi_i(q) = E_i\psi_i(q) \qquad [2.68]$$

The rotational transition between these levels occurs at $\omega_{12}^o = \left(E_2^o - E_1^o\right)/\hbar$. The matrix elements for the full Hamiltonian are:

$$H_{11} = E_1^o,\ H_{22} = E_2^o \text{ and } H_{12} = H_{21} = -\mu_{12}E_o\cos\omega t \qquad [2.69]$$

with $\mu_{12} = \int\phi_1\hat{\mu}\phi_2 d\tau$. The elements of the density matrix $\rho(t)$ for the same system are given by:[71]

$$\rho_{mn} = \frac{1}{N}\sum_{v=1}^{N} C_{vm}^*(t)C_{vn}(t) \qquad m,n = 1,2 \qquad [2.70]$$

and can be separated into the amplitude and phase factors:[71]

$$\rho_{mn} = \left\{\frac{1}{N}\sum_{v=1}^{N}\left|C_{vm}(t)\right|\cdot\left|C_{vn}(t)\right|\right\}\cdot\left\{\frac{1}{N}\sum_{v=1}^{N}\exp\left[i\left(\gamma_{vn}(t) - \gamma_{vm}(t)\right)\right]\right\}. \qquad [2.71]$$

The density matrix is diagonal at thermal equilibrium because the phase relation between particles is random. The population distributions of the stationary states are expressed by the diagonal elements. When external coherent radiation interacts with the system, a phase coherence develops between the wave functions of the individual particles and the off-diagonal elements may be nonzero.

The mean expectation value of an operator $\hat{A}$, $\langle A\rangle_{av}$, can be calculated in terms of the density matrix using the following equation:

$$\langle A \rangle_{av} = Tr\{A \cdot \rho\} \qquad [2.72]$$

where Tr is the trace of the matrix. For example, this equation can be used to calculate the induced macroscopic dipole moment, P, of N particles:[71]

$$P = N \cdot Tr\{\mu \cdot \rho\}. \qquad [2.73]$$

The density matrix, $\rho(t)$, has a time dependence that can be expressed as:

$$i\hbar \frac{\partial \rho}{\partial t} = \left[\hat{H}, \rho\right] = \hat{H}\rho - \rho\hat{H} \qquad [2.74]$$

where $\hat{H}$ is the matrix representation of the Hamiltonian (equation [2.25]) in the $\psi_i(q)$ basis. A set of linear differential equations is obtained for the elements of the density matrix when the matrix representations for H and $\rho(t)$ are substituted in equation [2.74]:[71]

$$\begin{aligned}
\dot{\rho}_{11} &= & -ix_{12}\cos(\omega t)(\rho_{21} - \rho_{12}) \\
\dot{\rho}_{22} &= & -ix_{12}\cos(\omega t)(\rho_{21} - \rho_{12}) \\
\dot{\rho}_{12} &= i\omega_{12}^{o}\rho_{12} & -ix_{12}\cos(\omega t)(\rho_{22} - \rho_{11}) \\
\dot{\rho}_{21} &= -i\omega_{12}^{o}\rho_{21} & +ix_{12}\cos(\omega t)(\rho_{11} - \rho_{22}) = \dot{\rho}_{12}^{*}
\end{aligned} \qquad [2.75]$$

where $\dot{\rho} \equiv \frac{\partial \rho}{\partial t}$ and $x_{12} = E_o \mu_{12} / \hbar$, analogous to the Rabi frequencies in NMR spectroscopy.[72]

To "simplify" equation [2.75], a new set of matrix elements, $\tilde{\rho}_{mn}$ $(n,m = 1,2)$ is introduced:

$$\begin{aligned}
\rho_{11} &= \tilde{\rho}_{11} \\
\rho_{22} &= \tilde{\rho}_{22} \\
\rho_{12} &= \tilde{\rho}_{12}\exp[i(\omega t)] \\
\rho_{21} &= \tilde{\rho}_{21}\exp[-i(\omega t)]
\end{aligned} \qquad [2.76]$$

Equations [2.75] are this converted to: [73]

$$\begin{aligned}
\dot{\tilde{\rho}}_{11} &= & ix_{12}(\tilde{\rho}_{21} - \tilde{\rho}_{12}) \\
\dot{\tilde{\rho}}_{22} &= & ix_{12}(\tilde{\rho}_{12} - \tilde{\rho}_{21}) \\
\dot{\tilde{\rho}}_{12} &= i(\omega_{12}^{o} - \omega)\tilde{\rho}_{12} & +ix_{12}(\tilde{\rho}_{22} - \tilde{\rho}_{11}) \\
\dot{\tilde{\rho}}_{21} &= -i(\omega_{12}^{o} - \omega)\tilde{\rho}_{21} & -ix_{12}(\tilde{\rho}_{22} - \tilde{\rho}_{11})
\end{aligned} \qquad [2.77]$$

Equation [2.77] uses the "rotating wave approximation"[73] by writing $\cos(\omega t) = \frac{1}{2}\left(e^{i\omega t} + e^{-i\omega t}\right)$ and neglecting the counter-rotating terms ($\sigma_+ e^{i\omega t}$ and $\sigma_- e^{-i\omega t}$). Some real variables connected with equation [2.77] are now introduced to simplify the notation:

$$\begin{aligned} u_{12} &= \tilde{\rho}_{12} + \tilde{\rho}_{21} \\ v_{12} &= i(\tilde{\rho}_{21} - \tilde{\rho}_{12}) \\ w_{12} &= \tilde{\rho}_{11} - \tilde{\rho}_{22} \\ s_{12} &= \tilde{\rho}_{11} + \tilde{\rho}_{22} \end{aligned} \qquad [2.78]$$

Bloch equations can now be written as a simple form of equation [2.77]:[71]

$$\begin{aligned} \dot{u}_{12} &= -\Delta\omega \cdot v_{12} \\ \dot{v}_{12} &= \Delta\omega \cdot v_{12} - x_{12} w_{12} \\ \dot{w}_{12} &= x_{12} w_{12} \end{aligned} \qquad [2.79]$$

where $\Delta\omega = \omega_{12}^{o} - \omega$.

The pulse excitation experiment can be described in terms of the Bloch equations. The experiment will be separated into the excitation and observation periods. Initially, the polarization is zero, so that $u_{12}(t_o) = v_{12}(t_o) = 0$, the population difference is ΔN_o, and $w_{12}(t_o) = \Delta N_o / N$. The excitation occurs from a near-resonant, strong, short excitation pulse, x_{12}; if $x_{12} \rangle\rangle \Delta\omega$ (i.e. the excitation pulse frequency is close to the transition frequency), then $\Delta\omega$ can be neglected in equation [2.79] to give:

$$\begin{aligned} \dot{u}_{12} &= 0 \\ \dot{v}_{12} &= -x_{12} w_{12} \\ \dot{w}_{12} &= x_{12} w_{12} \end{aligned} \qquad [2.80]$$

The solutions to the differential equations are:[71]

$$\begin{aligned} u_{12}(t) &= u_{12}(t_o) = 0 \\ v_{12}(t) &= -w_{12}(t_o)\sin(x_{12} t) \\ w_{12}(t) &= w_{12}(t_o)\cos(x_{12} t) \end{aligned} \qquad [2.81]$$

These show an oscillation of $v_{12}(t)$ and $w_{12}(t)$ between $w_{12}(t_o)$ and $-w_{12}(t_o)$.

The observation period begins at t=τ_e, the time at which the microwave pulse is switched off. The system is no longer interacting with the applied field, making $x_{12} = E_o = 0$, and equations [2.79] become:

$$\begin{aligned} \dot{u}_{12} &= -\Delta\omega \cdot v_{12} \\ \dot{v}_{12} &= \Delta\omega \cdot u_{12} \\ \dot{w}_{12} &= 0 \end{aligned} \qquad [2.82]$$

These differential equations have the solutions:

$$\begin{aligned} u_{12}(t) &= -v_p \sin(\Delta\omega t) \\ v_{12}(t) &= v_p \cos(\Delta\omega t) \\ w_{12}(t) &= w_p \end{aligned} \quad . \qquad [2.83]$$

where v_p, w_p are given by the values of v_{12} and w_{12} at the end of the pulse:

$$\begin{aligned} v_p &= -w_{12}(t_o)\sin x_{12}\tau_e \\ w_p &= w_{12}(t_o)\cos x_{12}\tau_e \end{aligned} \qquad [2.84]$$

The induced macroscopic dipole moment, P, is related to u_{12} and v_{12} by the following relationship which can be derived from equations [2.76] and [2.78]:

$$P = N\mu_{12}\left[u_{12}(t)\cos(\omega t - \phi) - v_{12}(t)\sin(\omega t - \phi)\right] \qquad [2.85]$$

where u_{12} is the real part of P and is in-phase with the microwave perturbation and v_{12} is the imaginary part of P and is 90° out-of-phase. $w_{12} = \Delta N/N$ with ΔN being the difference in population and s_{12} is the sum of population probabilities which is constant for a two-level system and will not be considered further.

The solutions of equations [2.83] are inserted into equation [2.85] to produce for the polarization (assuming $\phi = 0$):[71]

$$
\begin{aligned}
P &= N\mu_{12}\left[-v_p \sin\Delta\omega t \cos\omega t - v_p \cos\Delta\omega t \sin\omega t\right] \\
&= -N\mu_{12} v_p \sin(\Delta\omega + \omega)t \\
&= -N\mu_{12} v_p \sin\omega_{12}^{o} t \\
&= N\mu_{12} w_{12}(t_o) \sin x_{12}\tau_e \sin\omega_{12}^{o} t \\
&= \Delta N_o \mu_{12} \sin x_{12}\tau_e \sin\omega_{12}^{o} t.
\end{aligned}
\qquad [2.86]
$$

The polarization reaches a maximum when $x_{12}\tau_e = \pi/2 = \frac{E_o \mu_{12}\tau_e}{\hbar}$. This describes the condition for a so-called $\pi/2$ pulse. The polarization oscillates at the rotational transition frequency ω_{12}^{o}; it is proportional to μ_{12} and the initial population difference ΔN_o.

Relaxation effects are not taken into consideration in equation [2.85]. In reality, relaxation times T_1 (spin-lattice relaxation time) and T_2 ("spin-spin" relaxation time) measure relaxation of the polarization to zero. To account for the relaxation processes, equation [2.85] must be multiplied by exponential terms $\exp(-t/T_1)$ and $\exp(-t/T_2)$ to describe the relaxation of the polarization to its equilibrium value.

Chapter 3

Experimental Details

3.1 General Description of the FTMW Experiment

The experiments performed for this thesis were done with the Balle-Flygare type pulsed jet Fourier transform microwave spectrometer[4] depicted schematically in Figure 3.1. The sample cell consists of a Fabry-Perot microwave cavity resonator contained in a stainless steel vacuum chamber. The cell consists of two spherical mirrors 28 cm in diameter, with a radius of curvature of 38.4 cm. The mirrors are mounted on a bearing beam which is fixed to the walls of the vacuum chamber. The mirrors are held approximately 30 cm apart; to tune the cavity one of the mirrors can be moved using an Oriel Motor Mike. The bearing beam allows for smooth linear motion.

Pulses of microwaves are applied to the samples in the cell from a hook antenna in the centre of the fixed mirror. This same antenna is also used to receive any free induction decay signals from the samples. When the cavity is tuned, a microwave standing wave is created, maximizing the microwave power in the cavity. The standing wave increases the efficiency of the excitation of samples with microwave pulses because it multiplies the path length for absorption. The cavity is designed for optimal performance in the frequency range 6-26 GHz.

Samples are studied entrained as <~1% in pulsed supersonic jets of noble gas, particularly neon and argon. The jets enter the cavity through a General Valve Series 9 pulsed nozzle, mounted in the stationary mirror and connected to the gas supply. In the jets the samples are in a collision-free environment, which makes this an ideal technique for studying unstable and reactive species. Appropriate gas mixtures are used to create the species of interest, the specific precursor mixtures for each experiment will be discussed in section 4.1. The backing pressures for each gas mixture were ~6-7 atm.

The collision-free property of the jets must be maintained by evacuating the cell completely after each pulse of gas. The vacuum chamber was pumped to approximately 10^{-6} torr (10^{-9} atm) by a diffusion pump backed by a rotary pump. The repetition rate of the sample pulses, and hence of the whole spectrometer, was limited by the capacity of the pump to ~1 Hz.

An interesting feature of our spectrometer is the ablation system which allows for study of metal-containing compounds.[13] It is shown schematically in the enlarged area of Figure 3.1. A metal rod with a radius of ~2.5 mm and a length of ~4 cm sits at the mouth of the nozzle. It is ablated with a pulsed Nd:YAG laser (Neodymium-doped Yttrium Aluminum Garnet); the fundamental (1064 nm) was used in the present experiments. The laser pulse was focused through a glass window to ensure proper ablation. The metal rod is constantly rotated and translated using an Oriel Motor Mike to ensure a fresh surface for each laser pulse, thus providing the best possible signal strength.[13] The plasma of metal created with each pulse enters the mixture of precursor gases, and the ensuing reactions produce the desired species. The gas mixture is then adiabatically expanded into the cavity cell, forced in by the backing pressure.

The collisions in the throat of the nozzle convert rotational and vibrational energies (particularly the former) into translational energy, resulting in a cooling of the internal degrees of freedom. Resulting rotational temperatures in the jet are ~2-3 K, with the vibrational temperatures being somewhat higher (~200 K).[74] This very low rotational temperature ensures that only the lowest rotational energy levels are populated. The supersonic expansion reduces the translational temperature, resulting in a very narrow velocity range for the molecules and atoms in the jet.

In the setup used for these experiments the molecular expansion and the direction of microwave propagation are coaxial. This arrangement optimizes the resolution and sensitivity of the spectrometer, but has the drawback of Doppler doubling for each transition line. This doubling occurs because the molecules emit radiation both forwards and backwards with respect

to the direction of the jet. The antenna detects the splitting in the frequency due to the Doppler effect. The Doppler splitting increases as the transition frequency increases. The rest frequency of the transition is the average of the frequencies of the two Doppler components. Typical Doppler splittings are ~ 35 kHz at 10000 MHz, with the line widths ~ 7-10 kHz full width at half maximum.

Regular tests are performed on the spectrometer to ensure its accuracy and sensitivity. Experiments are performed on the extensively studied carbonyl sulfide molecule (OCS)[75] and the performance of the spectrometer is compared to that found in previous tests.

3.2 Electronics

A schematic diagram of the circuitry of the spectrometer is shown in Figure 3.2. A 486 Personal Computer is used to control the experiments, as well as to collect and process the data.

The microwave radiation is produced with a Hewlett-Packard 8340A microwave synthesizer. Although its frequency range is 10 MHz – 20 GHz, the lowest frequency used in this work was ~ 7.5 GHz. To achieve frequencies above 20 GHz a doubler was inserted into the circuitry. The synthesizer is phase locked to an external Loran signal, giving a frequency accuracy of one part om 10^{10}. This same signal is used to phase lock all components of the spectrometer.

Samples are irradiated with microwave pulses at a monochromatic frequency ν_{MW}; this is the frequency of the standing wave of the cavity, and is intended to be within the cavity bandwidth of a spectroscopic transition of the sample. The transition frequency of a molecular signal, at $\nu_{MW} + \Delta\nu$, is received at the antenna and mixed with a second microwave signal at ν_{MW} + 20 MHz. The resulting signal, at 20 MHz – $\Delta\nu$, is again mixed with another signal at 25 MHz to produce a frequency of 5 MHz + $\Delta\nu$, which is digitized by a transient recorder and stored in the computer. The experiment is repeated many times and signal averaged in the computer in

order to improve the signal-to-noise ratio. The resulting time-domain decay signal is fast Fourier transformed to produce a frequency-domain spectrum.

Decay signals were digitized at a frequency of 20 MHz (50 ns per point). 4k points are collected in the computer. An additional 4k points can be added by zero filling. From the reproducibility of the measured frequencies, their estimated accuracy is ±1 kHz.

A photograph of the spectrometer is in Figure 3.3. The important components are marked.

3.3 Experimental Sequence

The gas mixture once prepared is allowed to equilibrate for 20-30 minutes. This ensures that the composition is constant throughout the container. The gas is quickly pulsed (~ 7 Hz) through the system. Experimental data are not collected during the fast cycles as they are used to completely and uniformly fill all connecting hoses.

Following the fast cycles, the spectrometer is set to a frequency near where a transition is thought to occur. The cavity is tuned into resonance by applying a frequency sweep into the cavity and monitoring the microwave power in transmission. The oscilloscope shows an absorption in the cavity by a sharp dip in the detected power; this is referred to as a cavity mode. The cavity is tuned by moving the movable mirror with the Motor Mike until the strongest cavity mode is achieved at the excitation frequency. This indicates an "envelope" of power extending approximately ± 0.5 MHz of ν_{MW} at 10 GHz.

The experiment contains several carefully timed pulses which are controlled by the computer. A schematic diagram of the pulse sequence is shown in Figure 3.4. The experimental cycle begins with the nozzle pulsing gas for a specified period of time (molecular pulse width). The laser delay then allows the gas to travel through the nozzle. The laser is pulsed and the metal plasma is produced. The molecular pulse width and the timing of the laser pulse are crucial to the signal-to-noise ratio and small changes in their values can dramatically affect the

chances of detecting spectra of isotopomers of low natural abundances. The molecular MW delay allows the reaction products from the nozzle to expand into the cavity. The next step introduces the microwave radiation by closing the P1 switch and allowing the microwaves to enter the cavity. Since the switches reflect microwave power when opened, isolators are used to minimize the interference of the reflections with the source signal. The sample interacts with the radiation, is excited and begins to rotate coherently if the radiation is of correct wavelength and power. When the radiation pulse is turned off (P1 switch opens after the time of the microwave pulse width), the molecules emit radiation at their transition frequencies and in the process lose their coherence. The final delay is called the measurement delay. Following this, the data acquisition is started by closing the P2 switch. Alternately with the sample pulse sequence, a pulse sequence without the sample is carried out. The resulting decay is subtracted from the sample decay in order to remove as much as possible effects of energy decay from the cavity alone. The procedure is repeated every 750 ms (~ 1.33 Hz) until the desired signal-to-noise ratio is achieved. The signal-averaged decay is converted into a frequency domain spectrum using a Fourier transform.

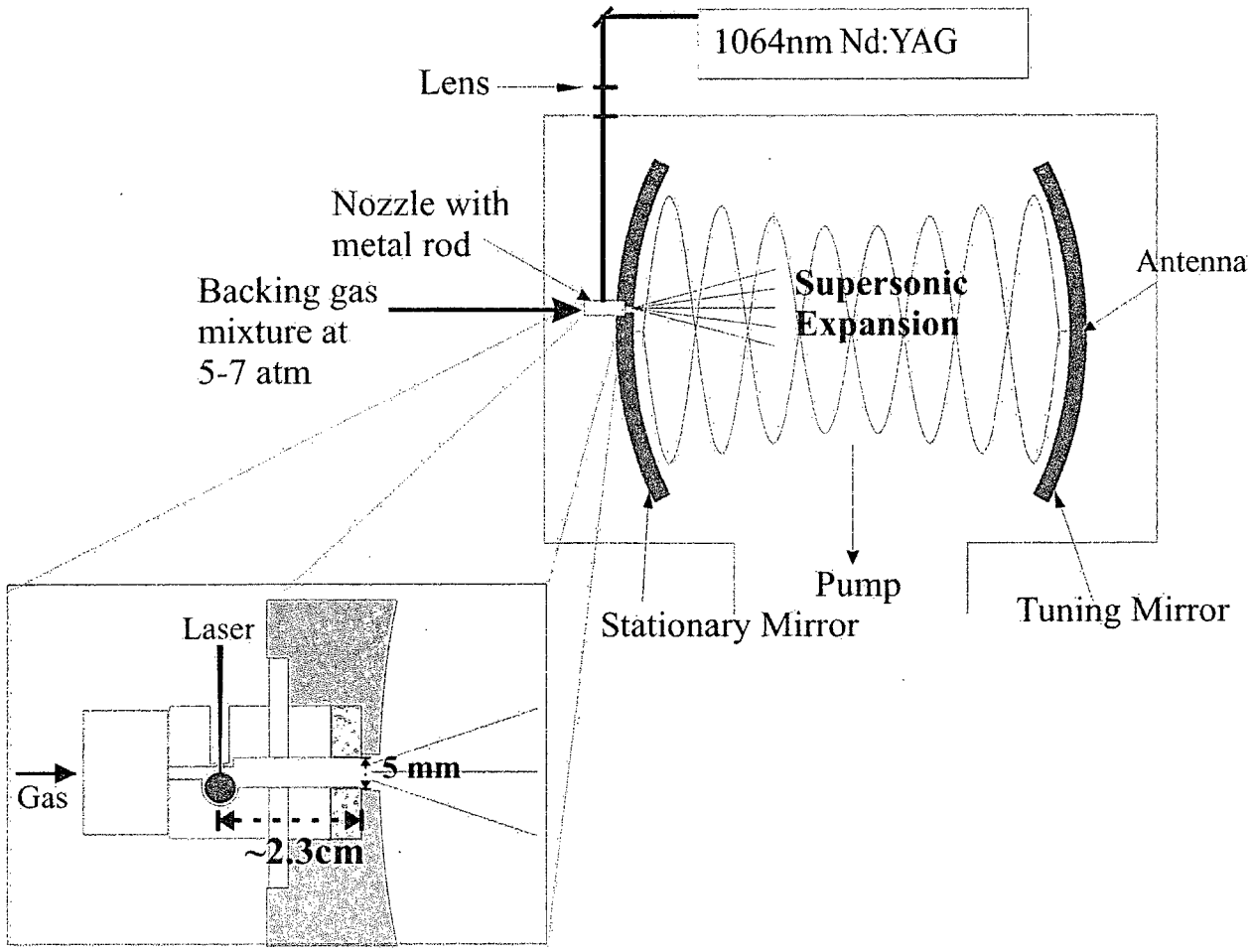

Figure 3.1 Schematic diagram showing the spectrometer and ablation system used for the experiments in this thesis.

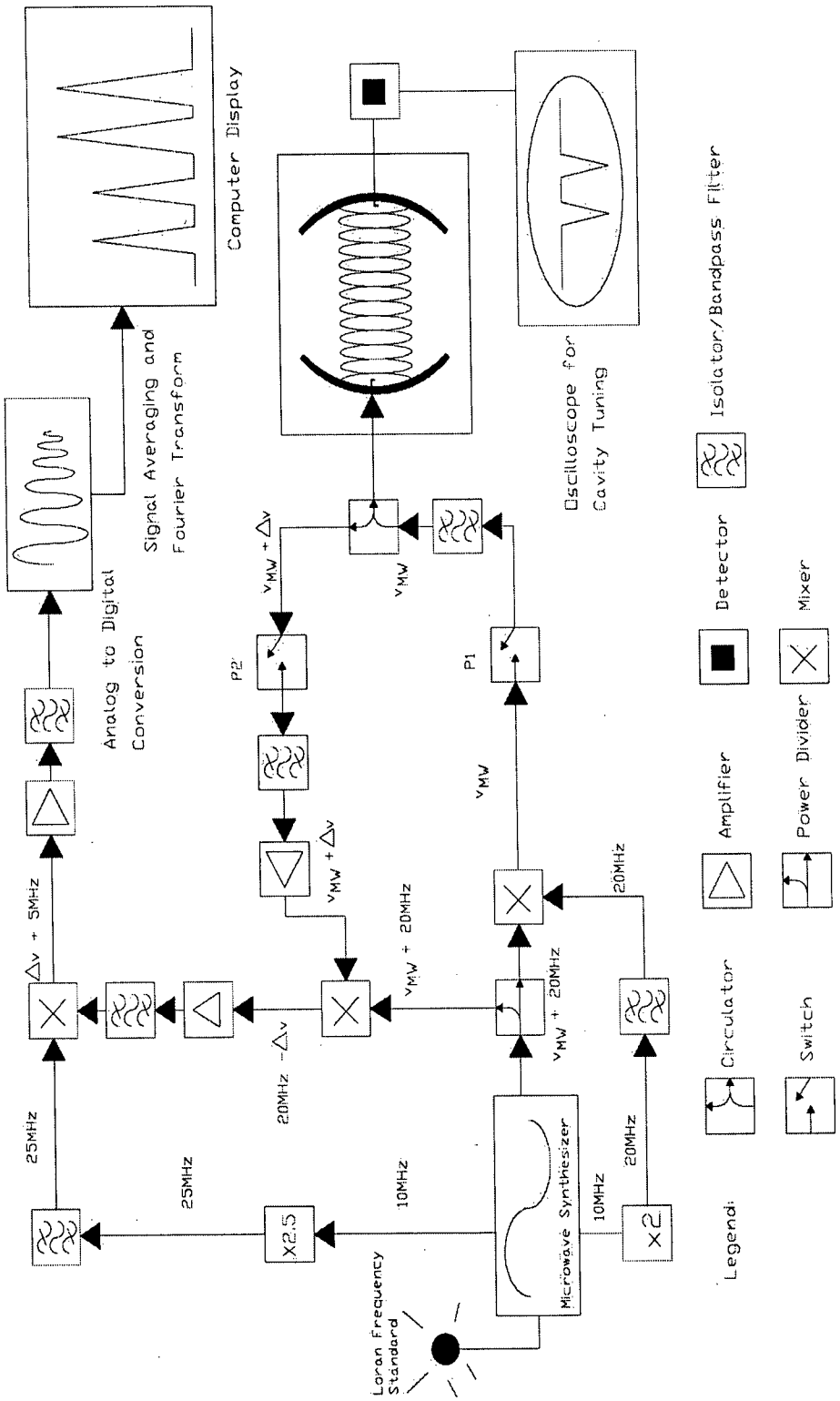

Figure 3.2 The schematic diagram of the fundamental circuitry used for our FTMW spectrometer.

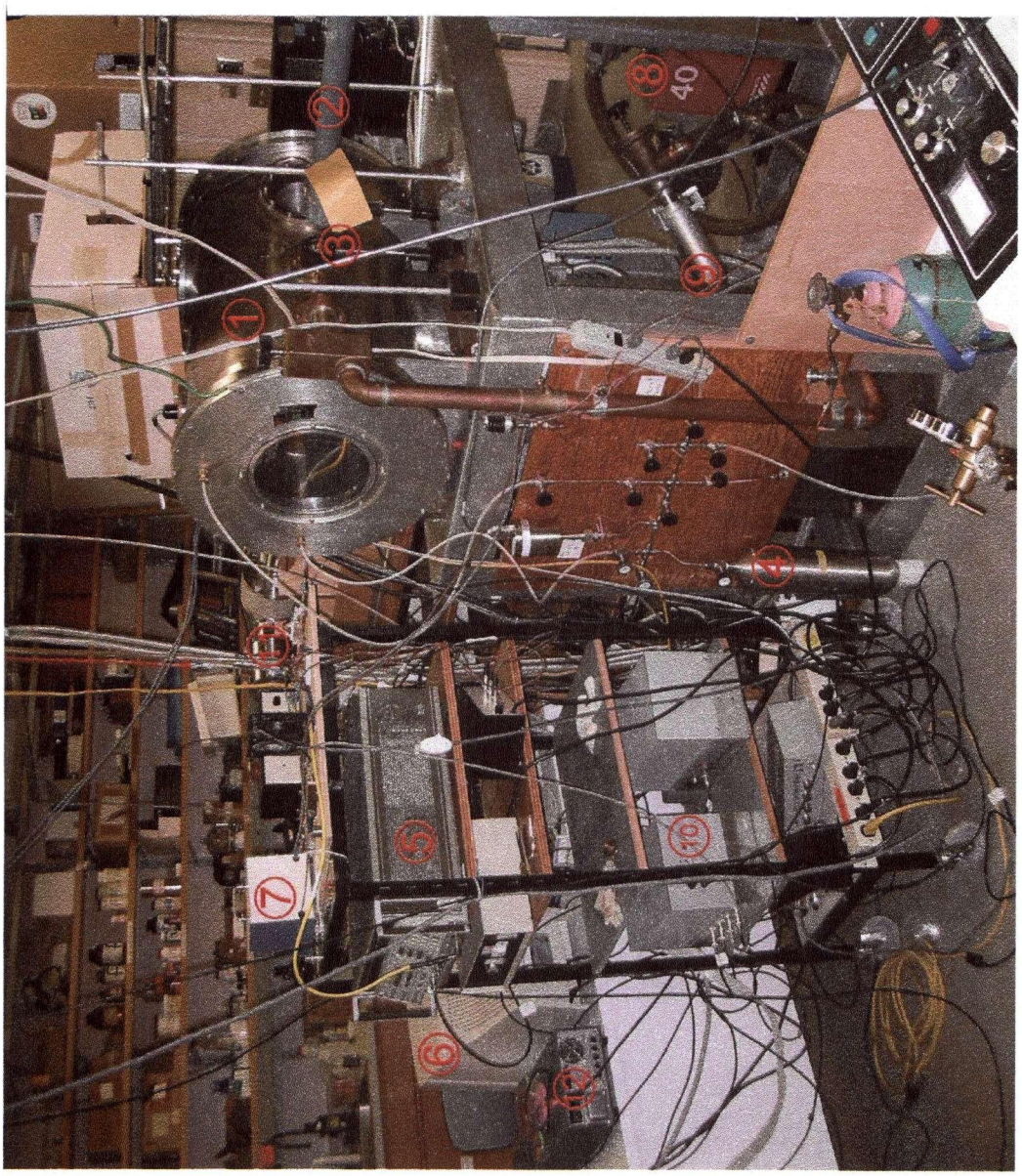

Figure 3.3 Photograph of spectrometer and its various components assigned in the legend.

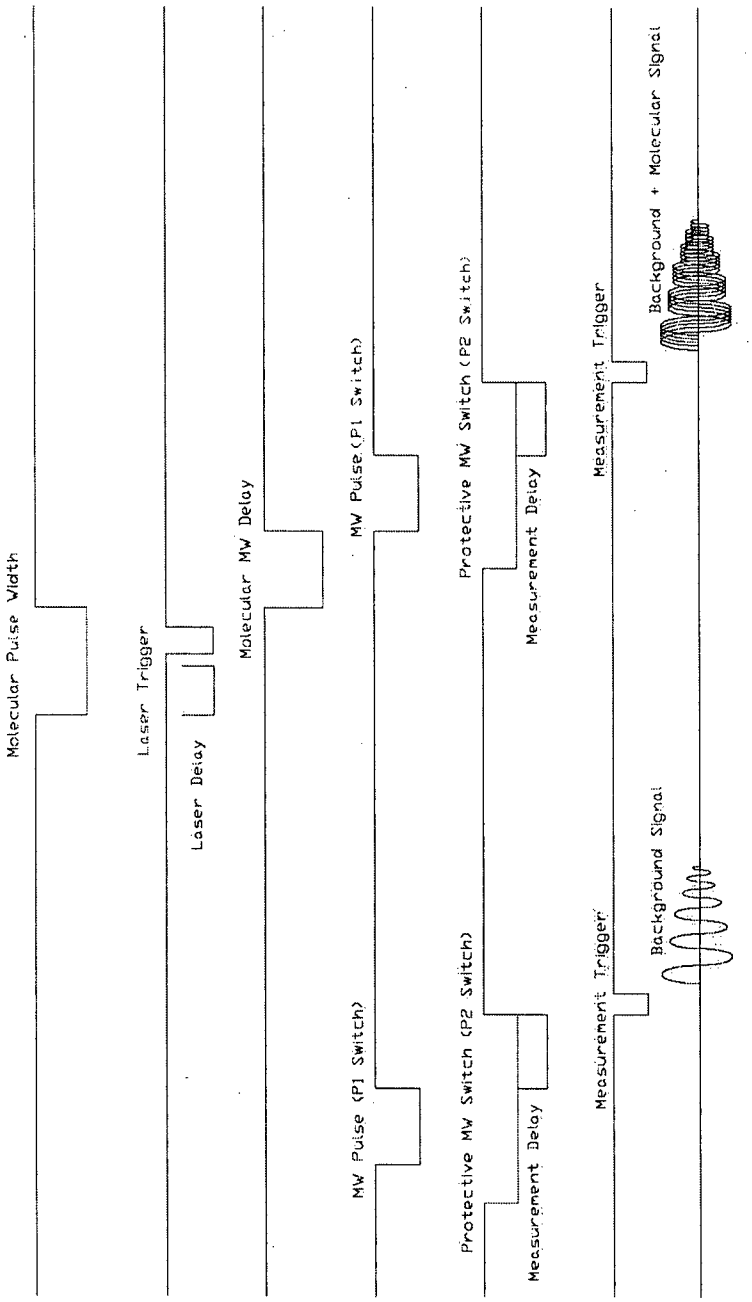

Figure 3.4 Schematic diagram of the pulse sequence used in our FTMW experiments using laser ablation.

Chapter 4

Results

4.1 Experimental Details

The experimental procedure outlined in Chapter 3 was used to measure the spectra reported in this thesis. A copper metal rod was ablated using a Nd:YAG laser at its fundamental wavelength of 1064 nm. The optimized precursor gas mixture to observe XeCuF contained 10% Xe and ~2% SF_6. Similarly, the optimized precursor gas mixture to detect XeCuCl contained 20% Xe and less than 0.1% Cl_2. The timings of the gas pulse, laser and microwave radiation pulses and various delays were first optimized using the spectrum of the CuX[18,21] monomer and $ArCuX$[26] using a gas mixture containing ~5% Xe gas in Ar, following which the search for the spectra began.

4.2 Spectra and Analyses

4.2.1 XeCuF

To shorten the preliminary search range, a prediction of a rotational constant was made from some reasonable parameters. The geometry was obtained from the *ab initio* bond lengths of Lovallo and Klobukowski.[37] It was found in $XeAgX$[33] that the experimental bond lengths (r(Xe-M) and r(M-X)) were consistently shorter than the calculated values and it was expected that the same would occur with the XeCuX bond lengths. The *ab initio* bond lengths for XeCuF were therefore adjusted to give a more reasonable geometry. The values used in the initial predictions of the rotational constant were:

r(Xe-Cu): 2.44 Å

r(Cu-F): 1.72 Å.

The rotational constant was calculated using equations [2.11] and [2.23] to be 1122 MHz for the main isotopomer of $^{132}Xe^{63}CuF$. An initial estimate for the nuclear quadrupole coupling constant of ^{63}Cu had to be made to predict the hyperfine pattern. Previous studies of noble gas – noble

metal halides showed that the ratio of the metal nuclear quadrupole coupling constant with different noble gases remained relatively constant. The nuclear quadrupole coupling constant for ^{63}Cu in XeCuF was therefore estimated by equating $[eQq(^{63}Cu)]_{ArCuF}/[eQq(^{63}Cu)]_{KrCuF}$ [References 26 and 32] and $[eQq(^{63}Cu)]_{KrCuF}/[eQq(^{63}Cu)]_{XeCuF}$. [Reference 32 and value wanted] In this way, the value for the nuclear quadrupole coupling constant for ^{63}Cu was estimated to be 45.9 MHz. A prediction of the hyperfine pattern was obtained using Pickett's global prediction program, SPCAT,[63] assuming also that the D_o would be approximately the same as for KrCuF (D_o = 0.38 kHz).[32] SPCAT diagonalizes the rotational Hamiltonian to predict the transition frequencies. The spectrum was predicted to contain four strong lines (two doublets) in a 1.3 MHz scan. The search began in the region of 8970 MHz for the J = 4-3 transition.

The first peak was found at 9009 MHz, ~40 MHz away from the initial starting search frequency. After some optimization of the timings and the gas mix, this signal was visible in fewer than 75 averaging cycles. A second component of the copper hyperfine pattern was found at 9010 MHz, ~1 MHz away from the first component. Assigning these peaks to a specific isotopomer was difficult because of the multitude of Xe isotopes with significant natural abundances (^{129}Xe, ^{131}Xe, ^{132}Xe, ^{134}Xe and ^{136}Xe being 26.4%, 21.2%, 26.9%, 10.4% and 8.9% abundant respectively).[76] The peaks had intensities consistent with either ^{129}Xe^{63}CuF or ^{132}Xe^{63}CuF. To confirm the assignment the spectra for the other isotopomer had to be measured. The second Xe isotopomer with slightly greater intensity was found at ~8937.5 MHz and was assigned to ^{132}Xe^{63}CuF and so the first peaks measured were assigned to ^{129}Xe^{63}CuF. Copper also has two naturally occurring isotopes: ^{63}Cu and ^{65}Cu (69.17% and 30.38% abundant, respectively),[76] and peaks from the weaker isotopomer were found at ~8868 MHz and assigned to ^{132}Xe^{65}CuF.

Several tests were carried out to confirm that the spectrum of XeCuF had indeed been found:

(i) The lines did not appear when the experiments were done without the laser pulse, but with all other conditions staying the same.

(ii) The lines could not be observed when either the SF_6 or Xe precursor was omitted from the gas mixture.

(iii) The complex was expected to be linear and the observed lines would be the J = 4-3 transition at ~$8B_o$. Successive (J+1) – J transitions should be separated by ~$2B_o$. The J = 5-4, 6-5, 7-6, 8-7, 9-8, and 10-9 transitions were found where expected.

(iv) Since both Xe and Cu have several isotopes, lines of several isotopomers should be resolved for each (J+1) – J transition. In total, spectra of seven isotopic species were measured for XeCuF. Assignments to the different isotopomers were also confirmed by several means:

a. Their relative frequencies could be predicted from the geometry using SPCAT[63];

b. Their intensities were consistent with their isotopic abundances. For instance, the lines from the main isotopomer, $^{132}Xe^{63}CuF$, were measurable after ~1000 averaging cycles, while lines from less abundant isotopomers required many more (e.g. 25,250 for $^{131}Xe^{63}CuF$ and 10,000 for $^{136}Xe^{63}CuF$);

c. The quadrupole moments for ^{63}Cu and ^{65}Cu (both nuclear spin I=3/2) are different (-21.2 fm^2 compared to -19.5 fm^2, respectively).[76] As mentioned in Section 2.2.1, the energy level spacings are proportional to the quadrupole moments and different hyperfine patterns can be expected. The splittings of the hyperfine components in ^{63}Cu – containing molecules should be greater because of its larger quadrupole moment; this was observed in the measured spectra.

d. The lines assigned to $^{129}Xe^{63}CuF$ did not show any additional hyperfine splitting from the I = ½ ^{129}Xe nuclei. This is consistent with the small magnetic moment of ^{129}Xe (m = -0.779763(84) μ_N)[76] and the results of previously observed

^{129}XeAgX and ^{129}XeAuF spectra.[33,34] A slight decrease in intensity was observed when comparing with the corresponding ^{132}XeCuF molecule, which has been attributed to line broadening because of the spin of ^{129}Xe;

e. ^{131}Xe has a nuclear spin (I = 3/2) and a quadrupole moment. Following the theory in Section 2.2.1.2, a second quadrupolar nucleus will couple with the angular momentum and cause additional splitting of the rotational levels and of the transition lines. The transitions assigned to the ^{131}Xe^{63}CuF isotopomer are indeed more complex. Its spectrum is described in detail in section 4.3 below.

Tables of the measured transition frequencies with their quantum number assignments for all observed isotopomers are presented in Appendix A. The coupling scheme:

$$\mathbf{J} + \mathbf{I_{Cu}} = \mathbf{F} \qquad [4.1]$$

was used for the analysis and in the corresponding Tables and Figures for all isotopomers, except ^{131}Xe^{63}CuF which will be discussed later. For the main isotopomer, ^{132}Xe^{63}CuF, it was not possible to measure the J = 8-7 transition since a cavity mode could not be obtained and as a result the cavity could not be frequency tuned. For J = 9-8 and 10-9 transitions though, the spectra could be successfully measured because of the use of a frequency doubler as explained in section 3.3.

Figures 4.1 and 4.2 show typical transitions obtained for ^{132}Xe^{63}CuF and ^{132}Xe^{65}CuF from the FTMW spectrometer. Each figure shows an entire (J+1) – J transition. The splitting between the two spectral lines in each transition results from the hyperfine coupling of Cu. It should be noted that only two lines were obtained per transition instead of the predicted four, chiefly because the Cu quadrupole splitting is first order. In addition, no spin-rotation splitting due to F was obtained. The difference in the quadrupole splitting in the two spectra is caused by the difference in the quadrupole moments of the two copper isotopes as mentioned above.

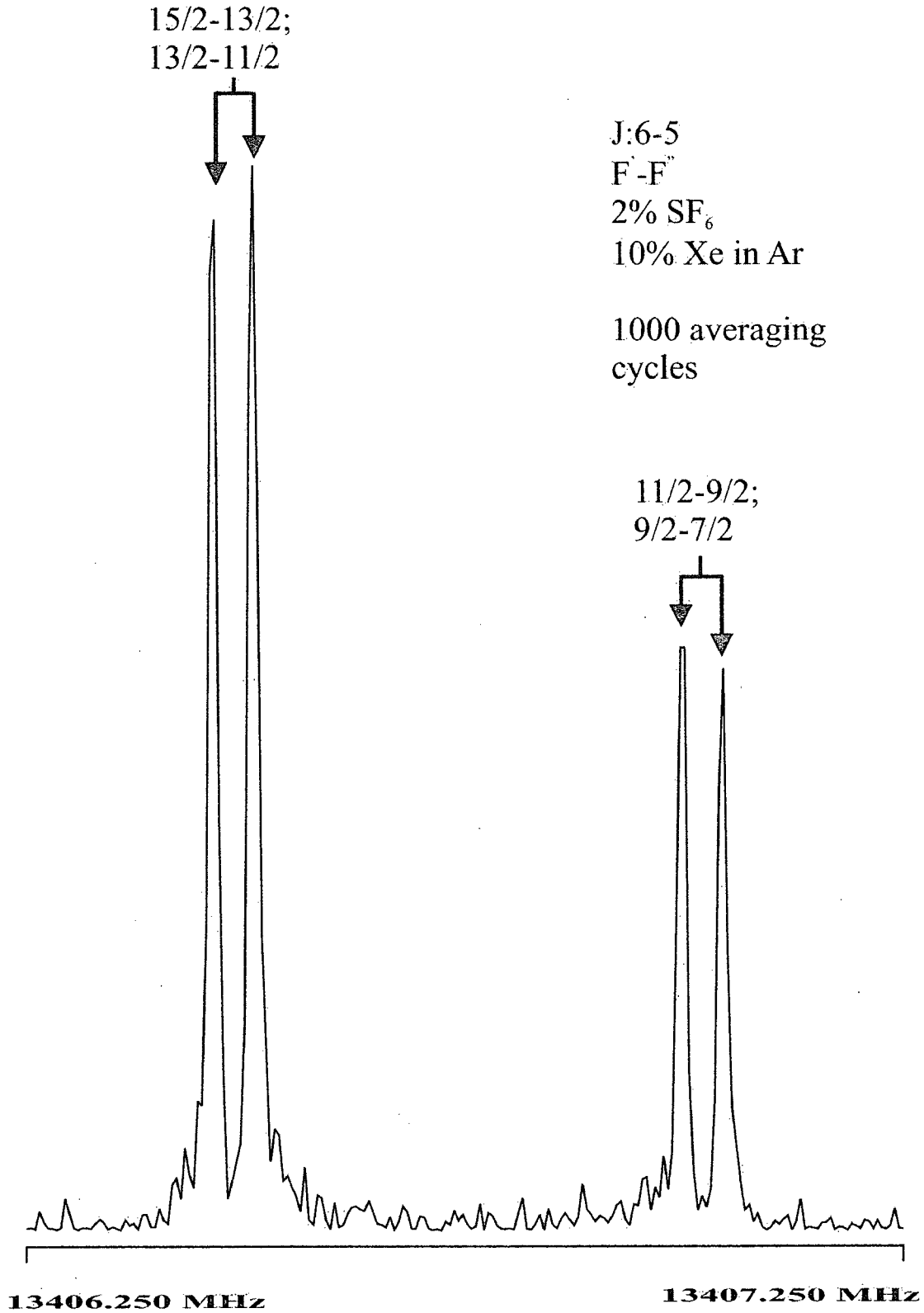

Figure 4.1 Portion of the observed hyperfine structure for $^{132}Xe^{63}CuF$ in the J = 6-5 transition. 1000 averaging cycles were taken over 4k data points; an 8k transform was used. The excitation frequency was 13406.6 MHz.

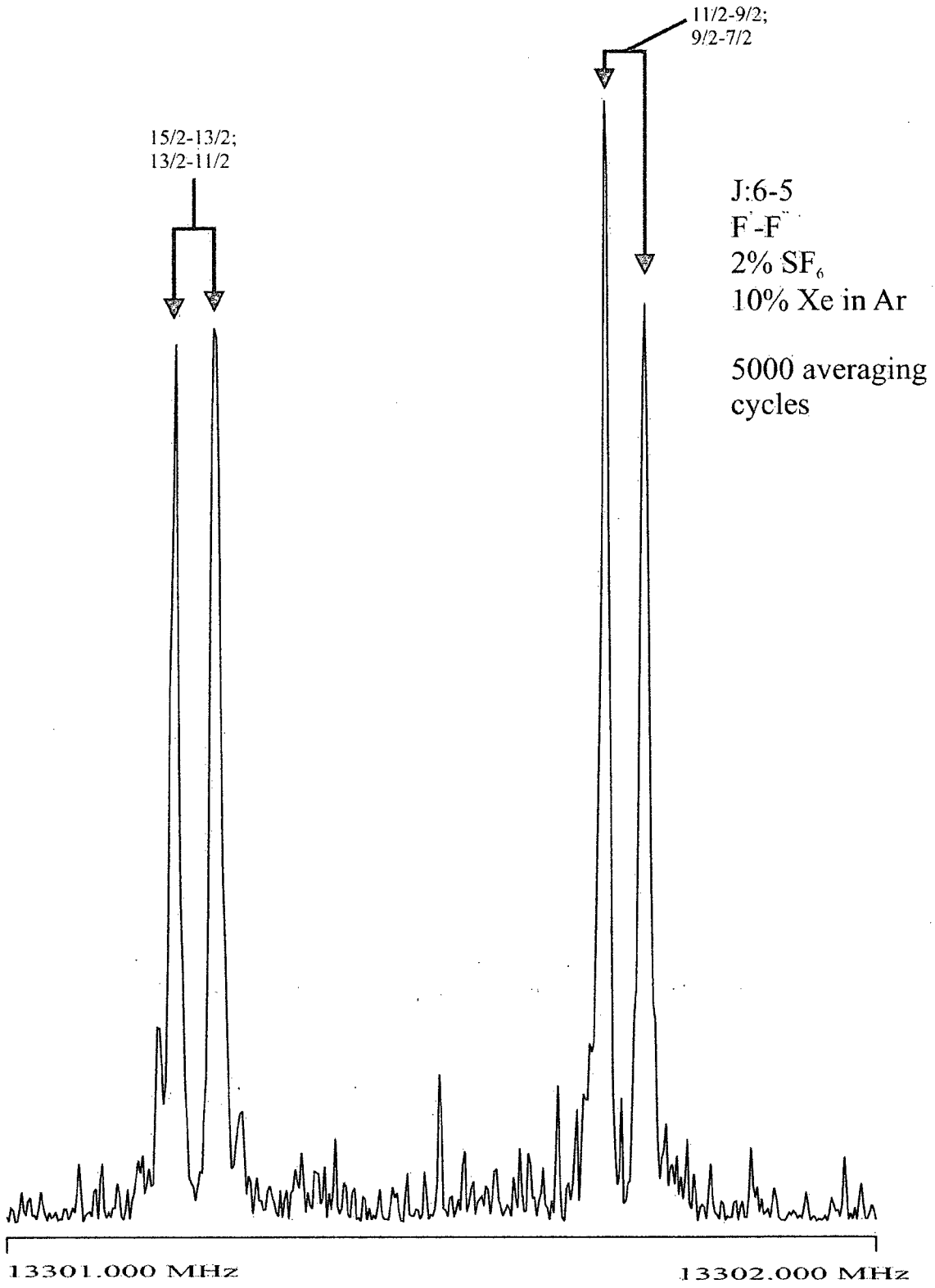

Figure 4.2 Portion of the observed hyperfine structure for $^{132}Xe^{65}CuF$ in the J = 6-5 transition. 5000 averaging cycles were taken over 4k data points; an 8k transform was used. The excitation frequency was 13301.5 MHz.

The observed transition frequencies were fit to the rotational constant B_o, centrifugal distortion constant D_o, copper nuclear quadrupole coupling constant $[eQq(\mathrm{Cu})]_o$, and copper nuclear spin-rotation constant $[C_l(\mathrm{Cu})]_o$ using Pickett's global least-squares fitting program SPFIT.[63] The fitting procedure began after measuring the transition frequencies for one (J+1) – J transition. SPCAT and SPFIT were used in conjunction to initially fit the strongest lines from the initial prediction. Ideally when hyperfine structure complicates the spectrum, outlying components to the nuclear quadrupole splitting that match prediction and experimental data should be fit first. By fitting these outlying transitions, SPFIT recalculates the molecular constants and replaces them in the input file for SPCAT. By performing another prediction with the new constants, the centre of the transition, where assigning can be difficult since a majority of transitions occurs there, begins to resemble the experimental data. Additional lines can be fit from the prediction and SPFIT run again. It is best to assign only a couple of lines at a time then recalculate the constants; otherwise it may cause unreasonable fits (giving constants of impossible values or unreasonable signs). By repeating the cycle of assigning a couple of lines and running SPFIT to recalculate the spectroscopic constants, SPCAT can be used to predict where additional transitions can be found experimentally. When all strong lines have been measured, assigned, and fit, the molecular constants are determined as accurately as possible.

The final molecular constants for XeCuF are in Table 4.1. All the constants are well-determined for the main isotopomer. Heavier isotopomers have lower B_o values as would be expected from the inversely proportional relationship between B_o and the moment of inertia. The centrifugal distortion constant is much smaller in magnitude than the rotational constant suggesting that it is a small correction to the basic spectral pattern caused by the flexibility of molecules as mentioned in Chapter 2. The centrifugal distortion constant is similar for all isotopomers, ~0.19-0.20 kHz, which suggests that the molecule is quite rigid.

The nuclear quadrupole coupling constants obtained for both Cu isotopes are quite large and well determined. The ratio of the ^{63}Cu and ^{65}Cu nuclear quadrupole coupling constants is ~1.08, in correspondence with the ratio of their quadrupole moments.[76] The nuclear spin-rotation constant was resolved for the main isotopomer. This constant is several orders of magnitude smaller than the nuclear quadrupole coupling constant and should be thought of as a very small correction to the overall spectral pattern. The nuclear spin-rotation constants for all weaker isotopomers have been fixed to that obtained in the main isotopomer. The $C_I(^{65}\text{Cu})$ was obtained by multiplying $C_I(^{63}\text{Cu})$ by the ratio of the copper magnetic moments[76] and rotational constants.

4.2.2 XeCuCl

From the results for XeCuF, the bond lengths of Lovallo and Klobukowski[37] differed significantly from the experimental bond lengths. However an *ab initio* geometry obtained in our calculations (Chapter 6) had good agreement with experiment (within 0.02 Å). It was thought that *ab initio* calculations for XeCuCl would provide similar agreement and a prediction of the rotational constant from the geometry would provide a narrower search range.

The calculations were performed at the second-order Møller-Plesset (MP2) level of theory[77] using the GAUSSIAN 98 suite of programs.[78] The basis sets used for these calculations were 3-21G(d) and 6-311** for Xe and F respectively.[79,80] The Cu atom utilized an effective core potential (ECP) leaving 19 valence electrons ($3s^2 3p^6 3d^{10} 4s^1$). The ECP and the optimized Gaussian basis set (31111s/22111p/411d) for Cu were both taken from Andrae et al.[81] Two f-functions,[82] $\alpha_f = 3.1235$ and $\alpha_f = 1.3375$, were used to augment the Cu basis set. The (631111s/52111p) McLean-Chandler basis set[83] for Cl was augmented with one d-polarization function,[82] $\alpha_d = 0.75$. The following geometry was obtained:

r(Xe-Cu) = 2.46 Å

r(Cu-Cl) = 2.045 Å

and the preliminary rotational constant obtained for the main isotopomer, $^{132}Xe^{63}Cu^{35}Cl$, from this geometry was ~759 MHz.

The nuclear quadrupole coupling constants for ^{63}Cu and ^{35}Cl (both I = 3/2) were predicted using ratios done in a similar fashion as with $eQq(^{63}Cu)$ in XeCuF. The results were $eQq(^{63}Cu) \approx 41.8$ MHz and $eQq(^{35}Cl) \approx -26.6$ MHz. Using SPCAT,[63] a prediction of the spectrum showed that over 10 lines would be expected in a ~1.5 MHz range for each (J+1) – J transition. The initial search began at 10620 MHz for the J = 7-6 transition. The first peaks were found ~110 MHz away at 10513 MHz. After the timings were optimized, the signals from the main lines were visible in fewer than 80 averaging cycles. To obtain measurable signals for the least abundant isotopomers more than 10,000 averaging cycles were required. The first peaks found were provisionally assigned to the $^{132}Xe^{63}Cu^{35}Cl$ isotopomer. The $^{132}Xe^{65}Cu^{35}Cl$ transition was easily found from the SPCAT prediction. The $^{129}Xe^{63}Cu^{35}Cl$ transition required slightly more averaging cycles than expected, but lines were found where predicted.

Similar tests as with XeCuF were performed to confirm that the spectrum of XeCuCl had indeed been found:

(i) The lines did not appear when the laser pulse was omitted, with all other conditions remaining constant.

(ii) The lines did not appear when either the Cl_2 or Xe precursor was omitted from the gas mixture.

(iii) The complex was expected to be linear and the observed lines would be the J = 7-6 transition at ~$14B_o$. Successive (J+1) – J transitions should be separated by ~$2B_o$, and the J = 5-4, 6-5, 8-7, 9-8, and 10-9 transitions were found where expected.

(iv) The lines of several isotopomers, due to different Xe, Cu, and Cl containing isotopomers, should be resolved for each (J+1) – J transition. In total spectra

from eight isotopomers were measured for XeCuCl. Assignments to these isotopomers were confirmed by several means:

a. Their relative frequencies were predicted using SPCAT;

b. Their intensities were consistent with their isotopic abundances;

c. The hyperfine patterns from ^{63}Cu and ^{65}Cu were distinguishable as with the spectra of XeCuF. Similarly, the quadrupole moments for ^{35}Cl and ^{37}Cl (both nuclear spin I = 3/2) are different (-8.11 fm^2 compared to -6.39 fm^2)[76] and the spectra of ^{35}Cl isotopomers should have a larger splitting between hyperfine components and this is observed in the spectra.

d. Similar to the results with XeCuF, no additional hyperfine components were seen due to ^{129}Xe but there was a decrease in intensity;

e. As with XeCuF, the spectra of the ^{131}Xe – containing isotopomer should have additional splitting of the spectral lines and this was indeed seen. Details are in section 4.3.

Tables of the measured transition frequencies for all observed isotopomers of XeCuCl can be found in Appendix B. The coupling scheme:

$$\mathbf{J} + \mathbf{I_{Cu}} = \mathbf{F_1} \qquad [4.2]$$

$$\mathbf{F_1} + \mathbf{I_{Cl}} = \mathbf{F}$$

was used for the analysis and in the corresponding Tables and Figures for all observed transitions, except $^{131}Xe^{63}Cu^{35}Cl$ which is discussed later. Figures 4.3, 4.4, and 4.5 show typical transitions measured for XeCuCl. The difference in the splitting between the hyperfine components and thus the quadrupole moments of the copper isotopes can be seen by comparing Figures 4.3 and 4.4. Similarly, the difference in the quadrupole moments of the chlorine isotopes can be seen when comparing Figure 4.3 with Figure 4.5.

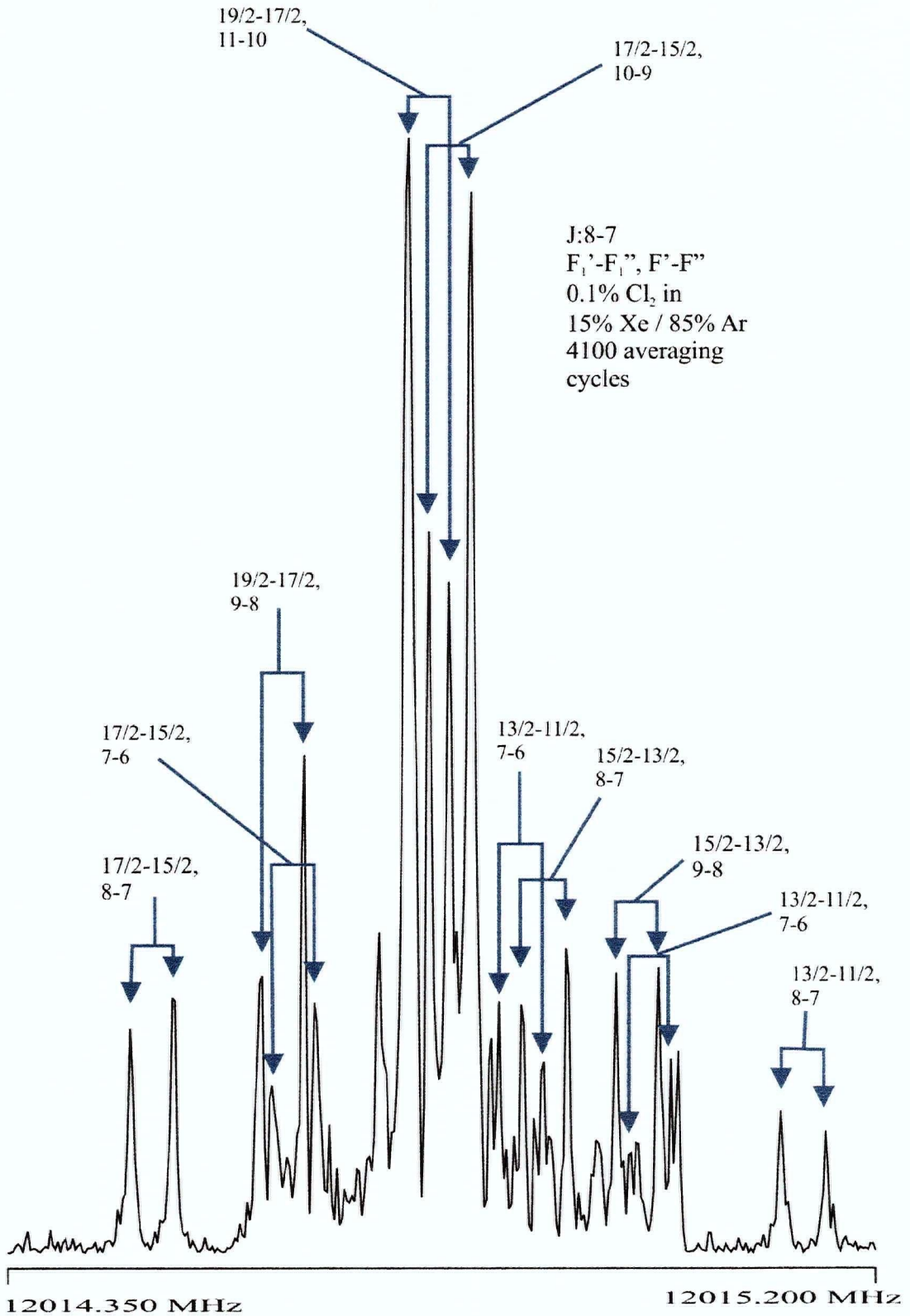

Figure 4.3 Portion of the observed hyperfine structure for $^{132}Xe^{63}Cu^{35}Cl$ in the J = 8-7 transition. 4100 averaging cycles were taken over 4k data points; an 8k transform was used. The excitation frequency was 12014.6 MHz.

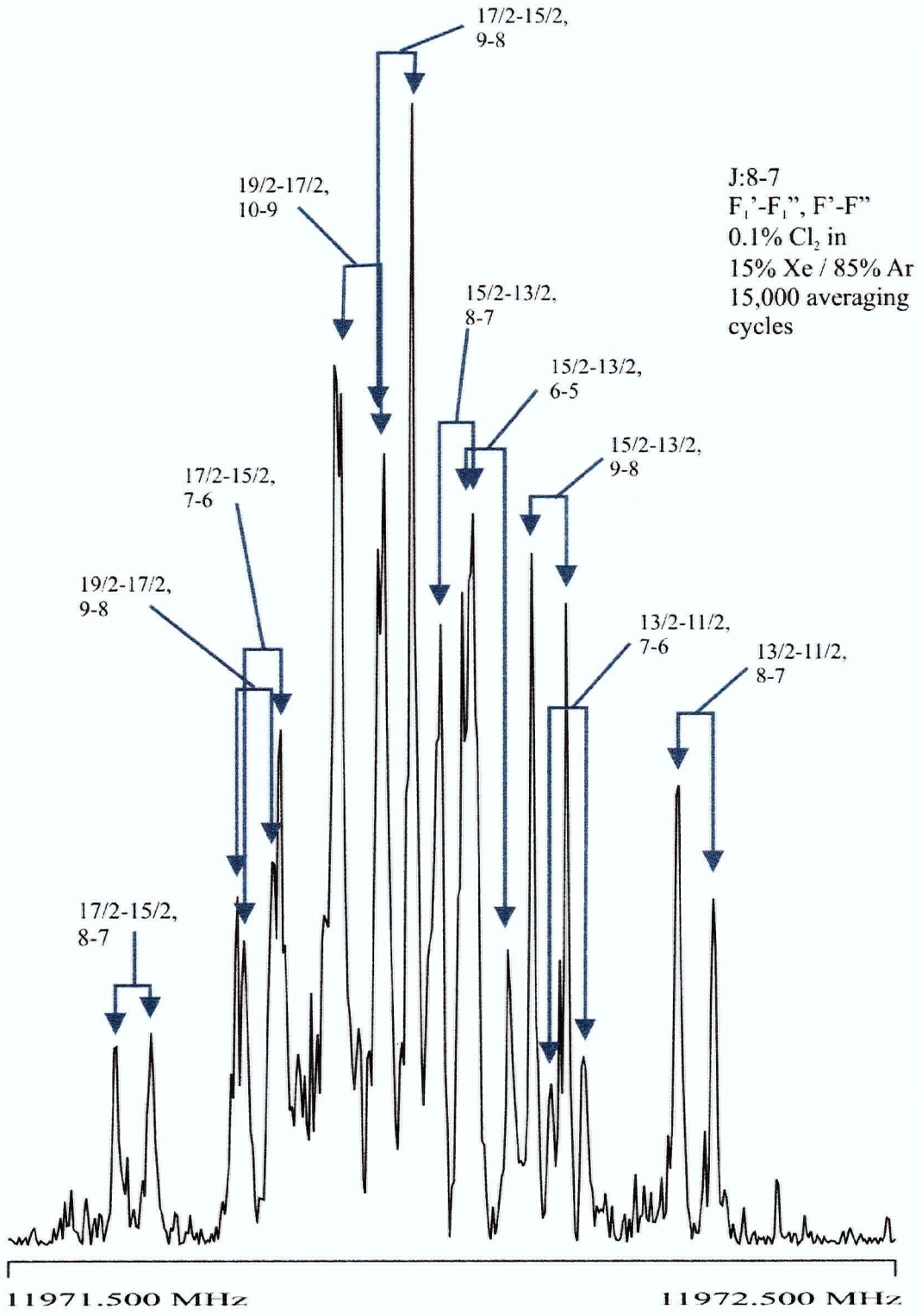

Figure 4.4 Portion of the observed hyperfine structures of $^{132}Xe^{65}Cu^{35}Cl$ in the J = 8-7 transition. 15,000 averaging cycles were taken over 4k data points; an 8k transform was used. The excitation frequency was 11972.0 MHz.

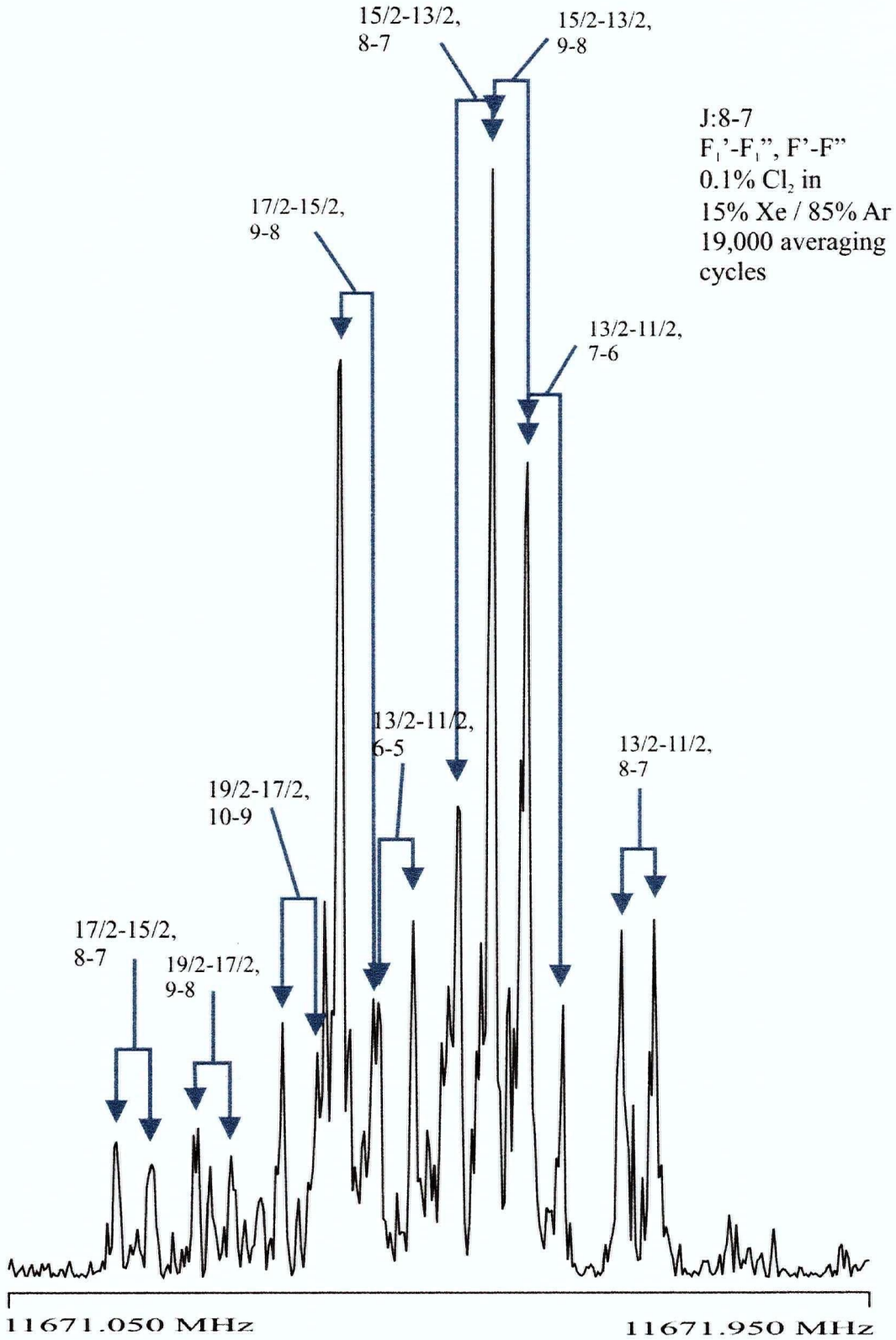

Figure 4.5 Portion of the observed hyperfine structure of $^{132}Xe^{63}Cu^{37}Cl$ in the J = 8-7 transition. 19,000 averaging cycles were taken over 4k data points; an 8k transform was used. The excitation frequency was 11671.5 MHz.

The measured transition frequencies of XeCuCl were fit to the rotational constant, B_o, centrifugal distortion constant, D_o, copper nuclear quadrupole coupling constant, $[eQq(\mathrm{Cu})]_o$, and chlorine nuclear quadrupole coupling constant, $[eQq(\mathrm{Cl})]_o$ by using Pickett's global least-squares fitting program SPFIT[63] in the same manner as with XeCuF.

The resulting molecular constants are in Table 4.2. All the constants are well-determined. The rotational constants, B_o, all seem reasonable for the assigned isotopomer. Similar to the results of XeCuF, heavier isotopomers have lower B_o values consistent with their inversely proportional relationship to the moment of inertia. The centrifugal distortion constant is very small and similar for all isotopomers, ~0.08-0.10 kHz, suggesting a quite rigid molecule. The nuclear quadrupole coupling constants for Cu are well determined and large. The ratio of the ^{63}Cu and ^{65}Cu nuclear quadrupole coupling constants is ~1.09, close to the ratio of their quadrupole moments (1.082).[76] The Cl nuclear quadrupole coupling constants are also well-determined and relatively large. The ratio of the ^{35}Cl and ^{37}Cl nuclear quadrupole coupling constants is ~1.27, also in keeping with the ratio of their quadrupole moments (1.269).[76]

4.3 ^{131}Xe Hyperfine Structure

The experimental procedure to measure the ^{131}Xe^{63}CuX spectra remained the same as described in Section 4.1. Xenon has 9 naturally occurring isotopes and ^{131}Xe (21.1% abundant)[76] is the only one with a nuclear spin greater than 1 ($I(^{131}\mathrm{Xe}) = 3/2$) and a quadrupole moment. The measurement and analysis of ^{131}Xe containing molecules provides a measurement of the ^{131}Xe nuclear quadrupole coupling constant $eQq(^{131}\mathrm{Xe})$ which is an indication of the asymmetric electron density distribution at the Xe nucleus. The strength of interactions between the noble gas and the metal can be indicated by an asymmetric electron density distribution. The signals, though weak, for both ^{131}Xe^{63}CuF and ^{131}Xe^{63}Cu^{35}Cl were visible in natural isotopic abundance (14.7% for ^{131}Xe^{63}CuF and 11.1% for ^{131}Xe^{63}Cu^{35}Cl).[76]

4.3.1 Spectrum of $^{131}Xe^{63}CuF$

The spectrum of $^{131}Xe^{63}CuF$ was very weak, and the assignment of the hyperfine components was not straightforward. The assignment method chosen was to initially set the $eQq(^{63}Cu)$ to the value obtained for the main isotopomer. An estimate for $eQq(^{131}Xe)$ in $^{131}Xe^{63}CuF$ was made by assuming the change in the eQq for the noble gas would remain constant when changing the metals. The $[eQq(^{83}Kr)]_{KrAgF}/[eQq(^{83}Kr)]_{KrCuF}$ [References 29 and 32] ratio was equated to the $[eQq(^{131}Xe)]_{XeAgF}/[eQq(^{131}Xe)]_{XeCuF}$ [Reference 33 and this work] ratio and the estimated $eQq(^{131}Xe)$ for XeCuF was -101 MHz. A prediction using SPCAT[63] was performed and the fitting began as described in Section 4.2.1. The coupling scheme for the analysis in this case was:

$$\mathbf{J} + \mathbf{I_{Xe}} = \mathbf{F_1}$$

$$\mathbf{F_1} + \mathbf{I_{Cu}} = \mathbf{F} \qquad [4.3]$$

The transition frequencies along with their quantum number assignments can be found in Appendix A. In total, three (J+1)-J transitions were measured and fit (J = 4-3, 5-4, and 6-5). Figure 4.6 shows the J = 6-5 transition for $^{131}Xe^{63}CuF$ obtained in 25,250 averaging cycles. The additional splitting in Figure 4.6 when compared to Figure 4.1 is due to the hyperfine structure from the ^{131}Xe nucleus. The frequencies were fit with SPFIT[63] to rotational and centrifugal distortion constants plus three hyperfine constants, $[eQq(^{131}Xe)]_o$, $[eQq(^{63}Cu)]_o$, and $[C_l(^{63}Cu)]_o$. The resulting constants are in Table 4.1.

4.3.2 Spectrum of $^{131}Xe^{63}Cu^{35}Cl$

The spectrum of $^{131}Xe^{63}Cu^{35}Cl$ was also very weak and was complicated additionally by the presence of three quadrupolar nuclei, hence making the assignment that much more difficult. The fitting method involved initially setting the $eQq(^{63}Cu)$ and $eQq(^{35}Cl)$ to the values obtained for the main isotopomer ($^{132}Xe^{63}Cu^{35}Cl$). An estimate of $eQq(^{131}Xe)$ in $^{131}Xe^{63}Cu^{35}Cl$ was obtained by calculating the ratio of $[eQq(^{131}Xe)]_{^{131}Xe^{107}AgF}/[eQq(^{131}Xe)]_{^{131}Xe^{107}Ag^{35}Cl}$ [Reference 33]

and comparing it to the ratio of $[eQq(^{131}\text{Xe})]_{^{131}Xe^{63}CuF}$ /$[eQq(^{131}\text{Xe})]_{^{131}Xe^{63}Cu^{35}Cl}$ [This work]. The estimated $eQq(^{131}\text{Xe})$ value was ~-82.9 MHz. SPCAT[63] produced a prediction and from that the fitting began as described in Section 4.2.1. The coupling scheme for the analysis in this molecule was:

$$\mathbf{J} + \mathbf{I_{Xe}} = \mathbf{F_1}$$
$$\mathbf{F_1} + \mathbf{I_{Cu}} = \mathbf{F_2} \qquad [4.4]$$
$$\mathbf{F_2} + \mathbf{I_{Cl}} = \mathbf{F}.$$

The transition frequencies along with their quantum number assignments can be found in Appendix B. In total, two J-transitions were measured and fit (J = 6-5 and 8-7). Unfortunately, the J = 7-6 transition of $^{131}Xe^{63}Cu^{35}Cl$ overlapped with the J = 1-0 transition of $^{65}Cu^{35}Cl$ [Reference 18] and no usable data could be acquired. The signal intensity of lower and higher J-transitions was much less; hence they could not be measured. Figure 4.7 shows the J = 8-7 transition for $^{131}Xe^{63}Cu^{35}Cl$ obtained after 25,150 averaging cycles. The spectrum is complex. The additional splitting, when compared to Figure 4.3 or 4.4, is due to the presence of the third quadrupolar nucleus (^{131}Xe). The frequencies were fit, again using SPFIT,[63] to rotational and centrifugal distortion constants plus three hyperfine constants, $[eQq(^{131}\text{Xe})]_o$, $[eQq(^{63}\text{Cu})]_o$ and $[eQq(^{35}\text{Cl})]_o$. The resulting constants are in Table 4.2.

4.4 Geometries

The rotational constants of Tables 4.1 and 4.2 have been used to determine the geometries of XeCuF and XeCuCl. Firstly, the spectra are consistent with linear structures for both complexes; therefore the parameters determined were simply the Xe-Cu and Cu-X internuclear distances. Ideally the equilibrium (r_e) bond lengths should be determined as explained in Section 2.3. However, the molecules were only observed in their ground vibrational states, the equilibrium bond lengths could only be approximated and not known precisely. To overcome these limitations, the geometries were thus determined using the

procedures outlined in Section 2.3, and the resulting geometries for XeCuF and XeCuCl are in Tables 4.3 and 4.4, respectively; r_o, r_{Ic}, $r_m^{(1)}$ and $r_m^{(2)}$ values are given. For XeCuF, an unconstrained $r_m^{(2)}$ fit produced highly correlated, poorly determined values, probably because no isotopic substitution could be done on fluorine. A fit performed with r(CuF) fixed to r_e for CuF monomer[21] produced satisfactory results. Tables 4.3 and 4.4 also compare the experimental bond lengths with the *ab initio* results done at the second-order Møller-Plesset (MP2) level of theory.[77] These *ab initio* results will be further discussed in Chapter 6. The second set of MP2 values was predicted by Lovallo and Klobukowski.[37] Both MP2 results are in moderate agreement with experiment, but agree well between themselves.

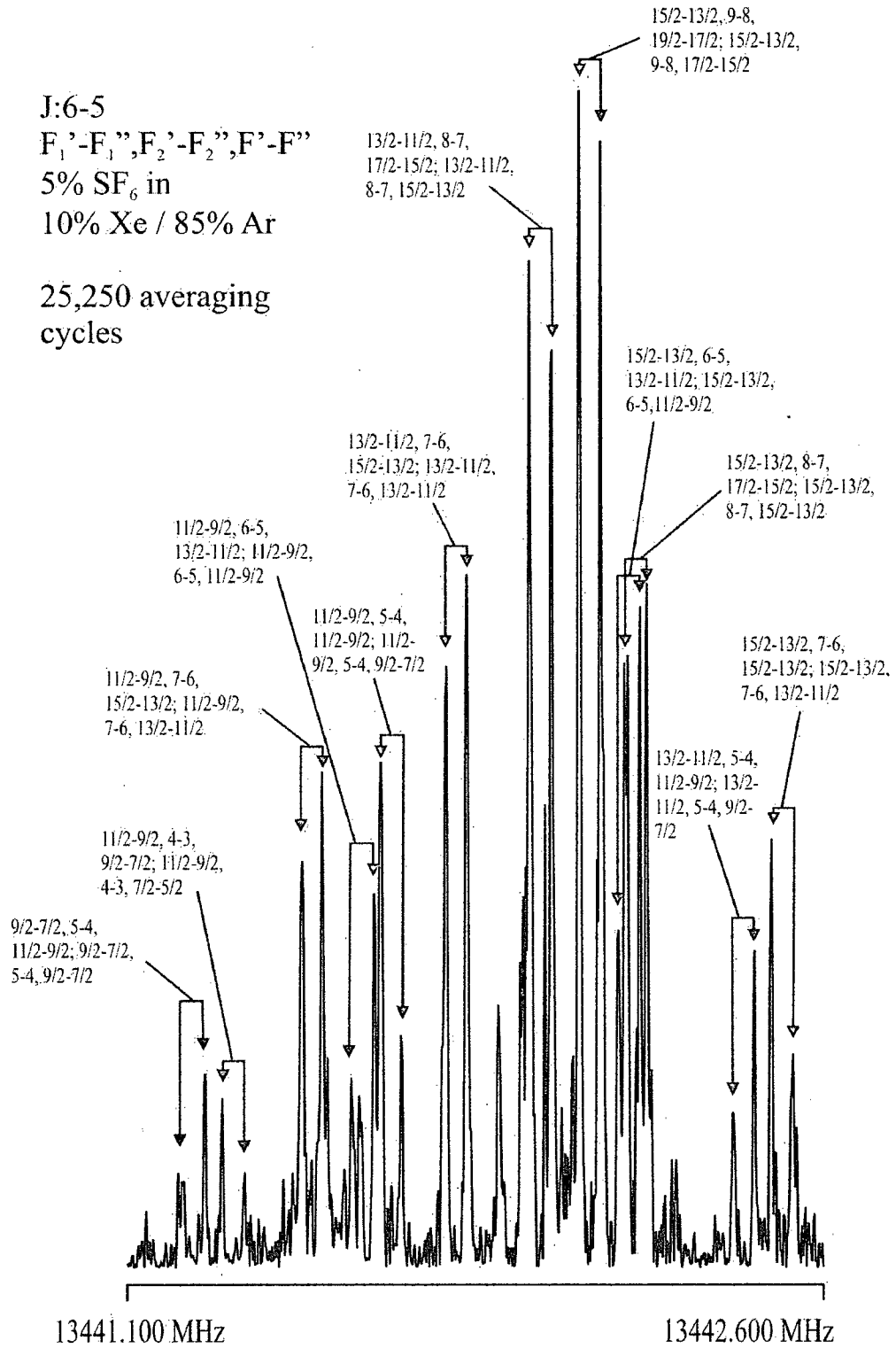

Figure 4.6 Portion of the observed hyperfine structure of $^{131}Xe^{63}CuF$ in the J = 6-5 transition. 25,250 averaging cycles were taken over 4k points; an 8k transform was used. The excitation frequency was 13442.0 MHz.

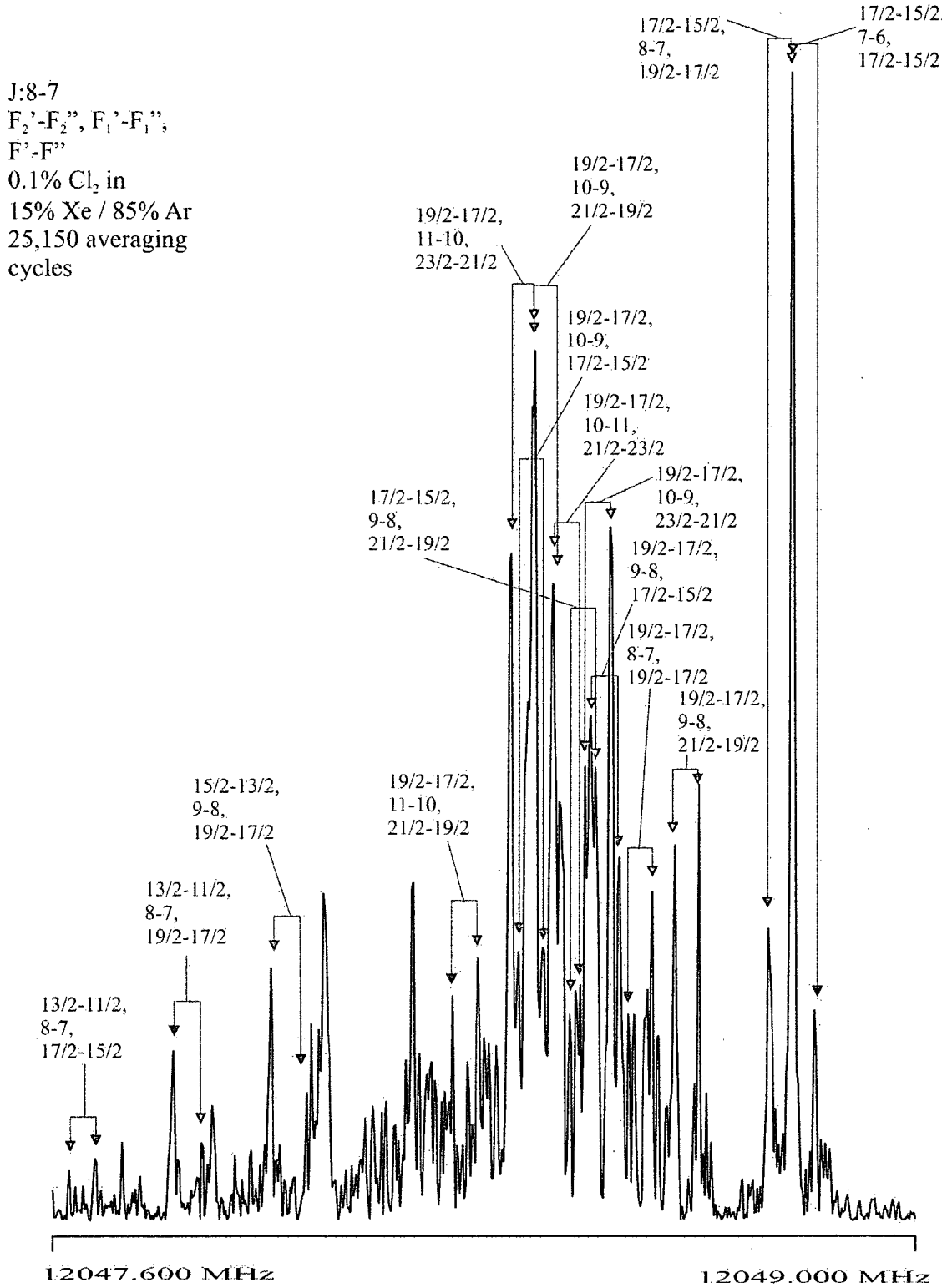

Figure 4.7 Portion of the observed hyperfine structure of $^{131}Xe^{63}Cu^{35}Cl$ in the J = 8-7 transition. 25,150 averaging cycles taken over 4k data points; an 8k transform was used. The excitation frequency was 12048.5 MHz.

Table 4.1 Spectroscopic Constants of XeCuF

Parameter	$^{129}Xe^{63}Cu^{19}F$	$^{131}Xe^{63}Cu^{19}F$	$^{132}Xe^{63}Cu^{19}F$	$^{134}Xe^{63}Cu^{19}F$
B_o(MHz)	1126.1926(3)	1120.1761(2)	1117.2361(1)	1111.4750(3)
D_J(kHz)	0.204(5)	0.207(3)	0.1967(8)	0.192(5)
eQq(Cu)(MHz)	47.62(8)	47.77(6)	47.76(11)	47.77(8)
eQq(^{131}Xe)(MHz)	-	-87.78(7)	-	-
C_I(Cu)(kHz)	4.29*	4.29*	4.29(95)	4.29*

	$^{136}Xe^{63}Cu^{19}F$	$^{129}Xe^{65}Cu^{19}F$	$^{132}Xe^{65}Cu^{19}F$
B_o(MHz)	1105.8760(3)	1117.4820(3)	1108.4624(3)
D_J(kHz)	0.193(5)	0.204(5)	0.193(5)
eQq(Cu)(MHz)	47.66(8)	44.06(8)	44.18(8)
C_I(Cu)(kHz)	4.29*	4.59*	4.59*

[a]Numbers in parentheses are one standard deviation in units of the last significant figure.
[b]Fixed at the value for $^{132}Xe^{63}Cu^{19}F$.
[c]Fixed at the value for $^{132}Xe^{63}Cu^{19}F$, scaled by the ratio of the ^{65}Cu and ^{63}Cu magnetic moments and rotational constants.

Table 4.2 Spectroscopic Constants of XeCuCl

Parameter	$^{129}Xe^{63}Cu^{35}Cl$	$^{131}Xe^{63}Cu^{35}Cl$	$^{132}Xe^{63}Cu^{35}Cl$	$^{134}Xe^{63}Cu^{35}Cl$
B_o(MHz)	757.30669(9)	753.0300(2)	750.93467(5)	746.8318(2)
D_J(kHz)	0.0794(7)	0.104(2)	0.0782(4)	0.073(1)
eQq(Cu)(MHz)	41.81(9)	41.6(1)	41.57(6)	41.6(2)
eQq(Cl)(MHz)	-26.10(6)	-26.4(1)	-26.01(4)	-25.90(7)
$eQq(^{131}Xe)$(MHz)	-	-81.4(2)	-	-
	$^{136}Xe^{63}Cu^{35}Cl$	$^{129}Xe^{65}Cu^{35}Cl$	$^{132}Xe^{65}Cu^{35}Cl$	$^{132}Xe^{63}Cu^{37}Cl$
B_o(MHz)	742.8423(2)	754.6708(2)	748.2566(1)	729.4729(3)
D_J(kHz)	0.076(1)	0.073(2)	0.078(1)	0.070(2)
eQq(Cu)(MHz)	41.3(2)	38.7(2)	38.1(1)	41.2(2)
eQq(Cl)(MHz)	-25.92(7)	-26.04(9)	-26.04(6)	-20.5(1)

[a]Numbers in parentheses are one standard deviation in units of the last significant figure.

Table 4.3 Geometry[a] of XeCuF

Method	r(Xe-Cu)	r(Cu-F)	Comments
r_o	2.4327(5)[b]	1.754(1)	
$r_{I\varepsilon}$	2.43231(3)	1.7507(1)	ε = 0.493(12) uÅ^2
$r_m^{(1)}$	2.43099(5)	1.7498(1)	c = 0.0463(12) u$^{1/2}$Å
$r_m^{(2)}$	2.42978(5)	1.744923[c]	c = 0.149(2) u$^{1/2}$Å; d = -0.244(6) u$^{1/2}$Å^2
MP2	2.456	1.732	
MP2[d]	2.459	1.737	

[a]Bond distances in Å.
[b]Numbers in parentheses are one standard deviation in units of the last significant figure.
[c]In the $r_m^{(2)}$ geometry the CuF internuclear distance was fixed at r_e of CuF.[21]
[d]Values predicted in Reference 37.

Table 4.4 Geometry[a] of XeCuCl

Method	r(Xe-Cu)	r(Cu-Cl)	Comments
r_o	2.471(7)[b]	2.058(1)	
$r_{I\varepsilon}$	2.4687(5)	2.0589(4)	$\varepsilon = 0.80(11)$ uÅ^2
$r_m^{(1)}$	2.4672(6)	2.0577(4)	$c = 0.062(8)$ u$^{1/2}$Å
$r_m^{(2)}$	2.4669(4)	2.0572(3)	$c = 0.104(13)$ u$^{1/2}$Å; $d = -0.144(42)$ u$^{1/2}$Å^2
MP2	2.4939	2.0482	
MP2[c]	2.497	2.060	
r_e(CuCl)[d]		2.051177	

[a]Bond distances in Å.
[b]Numbers in parentheses are one standard deviation in units of the last significant figure.
[c]Reference 37.
[d]Reference 18.

Chapter 5

Discussion of Experimental Results

The discussion will focus on both XeCuF and XeCuCl and how they contribute to the overall picture of bonding in the noble gas – noble metal halides. These molecules nearly complete the series and are two of the most strongly bonded; therefore the nature of noble gas to noble metal bonding can be discussed.

5.1 Molecular Structure

The geometry is the first indicator of the strength of interactions in any molecule or complex. Unfortunately, it is not possible to determine the type of bonding (covalent or van der Waals, etc...) based solely on the obtained geometry,[84] however important trends can be obtained. Table 5.1, a variation of Table 7 in Reference 31, presents the newly obtained Xe-Cu bond lengths, along with the Ng-M bond lengths of all NgMX molecules observed to date and for some related complexes. The *ab initio* results from our calculations and from Reference 37 are also given for comparison.

From this Table it is evident that the Xe-Cu bond lengths follow the trend established by the other NgMX molecules. The Xe-Cu bond length in XeCuF is shorter than in XeCuCl as with the other NgMX molecules. This is partially caused by the difference in electronegativities of the halides. Since fluorine is the most electronegative atom in the Periodic Table, it has the greatest power to attract electrons to itself.[85] As a result, the metal centre becomes more exposed to the noble gas cloud resulting in a shorter Ng-M bond length. The electronegativities decrease as the group is descended, and therefore chlorine and bromine have less ability to attract electrons to themselves leaving more of the metal centre shielded from the noble gas electron cloud and longer bond lengths are measured. The Xe-Cu bonds are slightly longer than the corresponding Kr-Cu and Ar-Cu bonds, as expected from studies on NgAgX and NgAuX. The Xe-Cu bonds are also shorter than Xe-Au and Xe-Ag, again confirming trends from previous

experiments and *ab initio* calculations. For all NgMX molecules, the bond lengths are quite short in comparison to the van der Waals complexes: Ar-NaCl,[43] ArHg,[86] Kr-HF,[87] and Xe-HF.[88] The short bond lengths are reproduced by both sets of *ab initio* calculations. The *ab initio* values for the Xe-Cu bond lengths are slightly greater than the experimental values, following the result of the other Xe-M molecules. All the *ab initio* values are consistent with an increase in bond strength as the noble gas is changed from Ar to Kr to Xe and as the metal is changed from Ag to Cu to Au. *Ab initio* calculations were performed on MNg_2^+ [35, 36] and on MNg^+ [89,90] and the geometry results from the studies are included in Table 5.1. The Ng-M bond lengths in MNg_2^+ and MNg^+ are comparable to the Ng-M bond length in NgMX.

Table 5.1 also shows the M-X bond lengths in NgMX and in the MX monomers. It can be seen that the experimental M-X bond lengths in the NgMX molecules are close to the monomer values. This suggests that the majority of the electron distribution changes occur between the noble gas and the noble metal. The *ab initio* results obtained from Reference 37 show a good agreement with experimental results.

Comparing the bond lengths in various NgMX is difficult due to the difference in sizes of the noble gases and noble metals. Table 5.2 is an expansion of Table 11 in Reference 31 and shows a comparison of experimental Ng-M bond lengths with values calculated from standard parameters. The first limit, which can be considered as the van der Waals limit, is the sum of the noble gas van der Waals radius[91] and the M^+ ionic radius.[31,92] The second limit, considered as the covalent limit, is the sum of noble gas and M(I) covalent radii.[48,93,94] Both of these limits are simply benchmark values and should not be considered as hard and fast rules. The NgMX molecules in Table 5.2 are grouped according to the metal, with the column of experimental bond lengths set between the van der Waals and covalent limits. The experimental bond lengths are expressed as a range since the bond lengths for all the halide molecules (X = F, Cl, Br) are being expressed. The shortest bond length in the range corresponds to the fluoride and the

longest bond length to the chloride (or bromide if measured). For all molecules in the series (except XeAuF),[34] the experimental bond length values are less than the van der Waals limit and greater than the covalent limit. It should be noted that the experimental bond length for the van der Waals complex of Ar-NaCl[43] is larger than the van der Waals limit as it has been defined for these purposes. The dots (...) in the table indicate when the experimental value is approaching one limit or the other. Table 5.2 clearly demonstrates the increase in strength of the bonding as the noble gas is changed from Ar to Kr to Xe. The ArAgX[25] bond lengths approach the van der Waals limit and the XeAgX[33] values are nearer the covalent limit. This trend is visible with the copper (and gold) molecules also. The bonding in XeCuX molecules is stronger than the KrCuX[32] and ArCuX[26] molecules. The trend of the strength of the interactions as the metal is changed is also visible. When comparing the XeMX, all the molecules are approaching the covalent limit, however XeAgX is 0.07-0.12 Å away while XeCuX is 0.06-0.10 Å away and XeAuX is shorter than the limit by 0.03 Å. The trend shows that the strength of interactions increases as the metal is changed from Ag to Cu to Au. This follows the results from previous studies. The experimental bond lengths for XeCuF and XeCuCl are very close to the covalent limit values. The short bond lengths in all NgMX molecules suggest than the interactions between the noble gas and the noble metal cannot be explained by van der Waals interactions alone.

5.2 Centrifugal Distortion Constants, Vibration Frequencies and Force Constants

Centrifugal distortion constants give an indication of the rigidity of a molecule. A large centrifugal distortion constant implies that the molecule is not rigid, but "floppy" and this is the expected result for a van der Waals complex. A small centrifugal distortion constant indicates a highly rigid molecule and is consistent with a strongly bound molecule. Table 5.3 contains, among other constants, the centrifugal distortion constants for the NgMX series and related complexes; this table is a variation of Table 7 in Reference 31. The centrifugal distortion

constants obtained for XeCuF and XeCuCl are consistent with the previous studies. These constants are smaller by at least an order of magnitude than the values obtained for the van der Waals complexes. This indicates that the XeCuF and XeCuCl are highly rigid molecules like the other NgMX.

The stretching frequencies ω(XeCu) were obtained from the centrifugal distortion constants using the pseudo-diatomic equation [2.20] . This approximation, as stated in Section 2.1.3, assumes the M-X unit is more rigid than the Ng-M bond. To evaluate the validity of this statement, the force constant for the Ng-M bond, k(Ng-M), should be much smaller when compared to the value for the M-X bond, k(M-X). For XeCuF, k(XeCu) (94 Nm^{-1}) is less than a third of k(CuF) (332 Nm^{-1})[95] indicating that the pseudo-diatomic approximation should be valid. Force constants will be discussed in more detail later in this section. The results for ω(XeCu) along with comparison to *ab initio* values are also in Table 5.3. The agreement between experimental and *ab initio* values supports the use of the pseudo-diatomic approximation to obtain the experimental values.

The XeCuF and XeCuCl molecules fit the established overall pattern: the ω(XeCu) frequencies are less than the corresponding ω(KrCu) [Reference 32] and ω(ArCu) [Reference 31], very close to those of ω(XeAu) [Reference 34], and greater than the ω(XeAg) [Reference33] values. The stretching frequencies for all NgMX molecules are much greater than the ω(ArNa) value for the Ar-NaCl van der Waals bond.[43] These ω(NgM) values are approaching those at the low-end for chemical bonds. The stretching frequencies for the M-X bond from the monomer are compared in Table 5.3 to the *ab initio* results of the monomers. The agreement between these two values is good.

Both centrifugal distortion constants and stretching frequencies have a mass dependence that complicates comparisons. Evaluating the stretching force constants k(NgM), using equation [2.21], again assuming a pseudo-diatomic approximation removes the mass dependence and

provides a clearer picture of the rigidity of the molecules. The values obtained for the stretching force constants are also given in Table 5.3. The values obtained for the XeCuF and XeCuCl molecules fit the established trends. The Xe-Cu bond in XeCuF is more rigid than in XeCuCl. The Xe-Cu bond is also more rigid than the Kr-Cu and Ar-Cu bonds.

The rigidity in the Au molecules is the greatest, followed by the Cu molecules and then by the Ag molecules. The force constants in the NgMX molecules are two orders of magnitude greater than k(Ar-Na) in Ar-NaCl.[43]

5.3 Copper Nuclear Quadrupole Coupling Constants

A measure of the field gradient (q) near a quadrupolar nucleus and consequently the distribution of electron density can be obtained from nuclear quadrupole coupling constants (eQq) as explained in section 2.2.1. Of major importance to the discussion of noble gas to metal bonding is the effect of the formation of NgMX on the nuclear quadrupole coupling constants.

The nuclear quadrupole coupling constants for both ^{63}Cu and ^{65}Cu were determined for XeCuF and XeCuCl. The nuclear quadrupole coupling constants for ^{63}Cu and ^{65}Cu are in ratio of their nuclear quadrupole moments,[76] as mentioned in section 4.2. Consequently, only the ^{63}Cu values will be considered in this discussion.

The $eQq(^{63}Cu)$ constants for XeCuX are presented in Table 5.4 along with $eQq(^{63}Cu)$ constants for a range of related molecules. Some trends can be clearly seen from this table. The nuclear quadrupole coupling constant of ^{63}Cu changes significantly when the noble gas is added to the monomer and as it is changed from Ar to Kr to Xe. The nuclear quadrupole coupling constant of ArCuF[26] is nearly double that of CuF[21] and those of KrCuF[32] and XeCuF are even larger. However, the changes to the nuclear quadrupole coupling constants as the noble gas is added are better considered as additive rather than multiplicative. For example, addition of Ar to CuX increases $eQq(^{63}Cu)$ by ~16-17 MHz, and addition of Kr increases it by ~20 MHz, while

addition of Xe increases it by ~25-26 MHz. These changes are ~38%, ~45% and ~56% of the change when X^- is added to form $XCuX^-$ ions.[96,97]

Similarly, addition of Ar, Kr and Xe cause changes of ~30%, ~37% and ~47% of those obtained when CO is added to form OCCuX compounds.[98] There are clearly very large redistributions of the electron density at Cu when the noble gases are added to form NgCuX. Since both $XCuX^-$ and OCCuX are fully chemically bonded for all X, these nuclear quadrupole coupling constant results suggest that the bonding in XeCuX can not be explained exclusively by van der Waals interactions.

The trend from the Cu containing molecules is also found in the Au containing molecules. The fractional changes of the $eQq(^{63}Cu)$ are very close to those of $eQq(^{197}Au)$ on addition of Ng to AuX.[19,20] The change in the nuclear quadrupole coupling constants on addition of Ar and Kr to AuX are ~33% and ~42% of those found when X^- is added to form $XAuX^-$ ions.[96] An estimate of the changes in the nuclear quadrupole coupling constants on addition of Xe cannot be made since the values of $eQq(^{197}Au)$ in $FAuF^-$ and XeAuCl have not yet been determined. The change in the nuclear quadrupole coupling constants on addition of Ar, Kr and Xe to AuX are ~27%, ~35% and ~50% of those found when CO is added to form OCAuX.[99] The Cu-containing molecules have the same fundamental properties as those containing Au.

5.4 Chlorine Nuclear Quadrupole Coupling Constants

The nuclear quadrupole coupling constants for ^{35}Cl and ^{37}Cl are in the ratio of their quadrupole moments,[76] as mentioned in Section 4.2; therefore the discussion will only consider the ^{35}Cl values.

The ^{35}Cl nuclear quadrupole coupling constants are presented in Table 5.5 along with the values obtained for related species. While it appears that their absolute changes on complex formation are less dramatic than for the $eQq(^{63}Cu)$ values, their fractional changes are comparable. For example, the change on forming XeCuCl from $CuCl^{18}$ is approximately ~48%

of the change on forming $ClCuCl^-$ ions.[96] This is comparable to, if a little smaller than, the fractional change in the ^{63}Cu constant (~56%). The same pattern occurs when comparing the change on forming XeCuCl from $CuCl$[18] to the change to form $OCCuCl$[98] (~57% for $eQq(^{35}Cl)$ and ~47% for $eQq(^{63}Cu)$).

For van der Waals complexes, the small changes in the ^{35}Cl nuclear quadrupole coupling constants have historically been interpreted in terms of a large amplitude bending. The following equation is used to calculate the angle between the MCl unit and the *a*-inertial axis, β, from the halogen nuclear quadrupole coupling constant in the complex and monomer, eQq and eQq_o, respectively:

$$eQq = [eQq_o + \Delta(eQq)]\left\langle \frac{3\cos^2\beta - 1}{2} \right\rangle. \qquad [5.2]$$

The $\Delta(eQq)$ term is the coupling constant change caused by electron rearrangement on complex formation and is assumed to be zero for van der Waals complexes. The angle β is related to θ, the angle of bend of the complex, by:

$$\langle \sin^2\theta \rangle \approx (1+\delta^2)\langle \sin^2\beta \rangle \qquad [5.3]$$

where $\delta = I_{MCl}/I_{NgMCl}$. The Cl coupling constant in XeCuCl gives a value of θ in the range of ~21°, which seems rather improbable given the apparent rigidity of the molecule from previous experimental evidence. This again suggests that the bonding in these NgMX molecules cannot be entirely explained using typical equations for van der Waals interactions.

5.5 ^{131}Xenon Nuclear Quadrupole Coupling Constants

The nuclear quadrupole coupling constants for the noble gas provide important information about the electron distribution at the noble gas on molecule formation. The noble gas provides a clear picture of charge rearrangement since the unbound Xe atom is spherically symmetric and has an $eQq(^{131}Xe) = 0$. Any changes in this value are indicative of the distortion of the noble gas electron cloud upon molecule formation.

The values of $eQq(^{131}Xe)$ in XeCuF and XeCuCl are entirely in keeping with those of XeAgX[33] and XeAuF.[34] Since $eQq(^{131}Xe)$ in XeCuCl follows the same trends as with XeCuF and the spectrum of XeAuCl has yet to be measured, the discussion will primarily be focused on the $eQq(^{131}Xe)$ value obtained in XeCuF. Table 5.7 is an extension of Table 10 in Reference 32 and presents the ^{83}Kr and ^{131}Xe nuclear quadrupole coupling constants for various Kr and Xe containing species. The nearly non-polar van der Waals complexes containing noble gas – noble gas bonds[10,100] have very small noble gas nuclear quadrupole coupling constants. This indicates that little rearrangement of the electron distribution occurs at the Kr or Xe centre. The hydrogen bonded complexes are more polar and slightly more charge rearrangement occurs at the Kr and Xe nuclei, as indicated by a slightly larger eQq value. The interaction with Xe is greater than with Kr as shown by a fractional change from the hydrogen bonded complexes of 1.0% and 0.6% to Xe ($[Kr]4d^{10}5p^{5}6s^{1}$)[101] and Kr^{+} [Reference 102] values respectively.

The NgMX molecules have considerably larger $eQq(^{83}Kr)$ and $eQq(^{131}Xe)$ values compared to van der Waals and hydrogen bonded complexes. This indicates a much stronger interaction between the noble gas and the metal centre. However, the nuclear quadrupole coupling constants for both ^{83}Kr and ^{131}Xe are still quite far from those of Kr^{+} and of Xe ($[Kr]4d^{10}5p^{5}6s^{1}$) respectively. From the $eQq(^{83}Kr)$ and $eQq(^{131}Xe)$ values, it can be clearly seen that the strength of interaction increases as the metal is changed from Ag to Cu to Au.

To ensure that the large Xe nuclear quadrupole coupling constants obtained for XeCuX are not purely electrostatics, it is appropriate to calculate the $eQq(^{131}Xe)$ values resulting from the polarization of the spherical electron distribution on Xe by the external charges on MX. The nuclear quadrupole coupling constants of ^{131}Xe are proportional to the field gradient at the nucleus V_{zz}. The relationship between the nuclear quadrupole coupling constant and V_{zz} is:[103,104,105]

$$(eQq) = -eQV_{zz} \qquad [5.4]$$

where (eQq) is to be considered a single unit, and e is the positive elementary charge.

This model considers a spherical atom in the presence of external charges. In this case, V_{zz} is predicted using:[103-105]

$$V_{zz} = (1+\gamma^{Xe})E_{zz} + \varepsilon^{Xe}E_z^2 + \ldots \qquad [5.5]$$

where E_z and E_{zz} ($\equiv dE_z/dr$) are, respectively, the field and field gradient at the Xe nucleus due solely to the external charges. The electrons are polarized by the external charges and this greatly magnifies the field gradient. This phenomenon is measured by γ, the Sternheimer antishielding constant (usually ~100), and ε, an additional constant. The designations γ^{Xe} and ε^{Xe} result because both γ and ε are characteristics of each element.

For XeCuX, E_z and E_{zz} due to CuX alone are given by the following equations:

$$E_z = -\frac{eq_{Cu}}{4\pi\varepsilon_0 r(XeCu)^2} - \frac{eq_X}{4\pi\varepsilon_0 r(XeX)^2} \qquad [5.6]$$

and

$$E_{zz} = \frac{eq_{Cu}}{2\pi\varepsilon_0 r(XeCu)^3} + \frac{eq_X}{2\pi\varepsilon_0 r(XeX)^3} \qquad [5.7]$$

where q_{Cu} and q_X are the effective charges on the Cu and X ions, and r(XeCu) and r(XeX) are the distances between Xe and Cu or X nuclei in the complex. A calculation to obtain the effective charges requires the MX dipole moment. For most metal halides, including CuF,[21] the dipole moment can be obtained from experimental results. For other metal halides, such as CuCl,[18] the dipole moments were estimated from the ionic characters (i_c) calculated from the halogen nuclear quadrupole coupling constants as described in Reference 31. The dipole moment calculated from the ionic character was obtained using the method of Gordy and Cook, taking into account the ionic polarizability using: [Reference 1, Equations 14.166 and 14.168]:

$$eri_c = \mu\left(1 + \frac{\alpha_{M^+}}{\left[r^2 + (r_M/2)^2\right]^{3/2}} + \frac{\alpha_{X^-}}{\left[r^2 + (r_X/2)^2\right]^{3/2}}\right) \qquad [5.8]$$

where e is the elementary charge, r is the bond length, α_{M^+} and α_{X^-} are the ionic polarizabilities. The values of i_c are taken from Reference 20 and α_{M^+} and α_{X^-} were obtained from Gordy and Cook for some of the values [Reference 1 Tables 14 and 15], while the values for Cu^+ and Au^+ were taken from Reference 31.

The dipole moments are shown in Table 6.1. From the dipole moment, the ionic charges, q_{eff} (in elementary charge units), can be estimated using this equation:

$$q_{eff} = 0.2082\frac{\mu}{r} \qquad [5.9]$$

where the dipole moment, μ, is in the units of Debye and the experimental bond length, r, in Angstroms. For XeCuF and XeCuCl, E_{zz} is ~ - 1.0 x 10^{19} V m^{-2}.

To apply equation [5.5], the values of γ^{Xe} and ε^{Xe} are required. There are several studies whose γ^{Xe} differ significantly. Keenan *et al.*[106] used a value of γ^{Xe} = 138. It should be noted that for a p^6 atom such as Xe, convention states that a positive γ is accompanied by a negative ε.[105] Baiocchi *et al.*[88] determined γ^{Xe} to be 157-159 by assuming that V_{zz} in Xe-HF and Xe-HCl could be obtained solely from the first term of equation [5.5]. A larger value of 177 was calculated by Feiock *et al.*[107] From this range of values, $138 \leq \gamma^{Xe} \leq 177$, the first term in equation [5.5] was calculated for XeCuF and XeCuCl using the average γ^{Xe} of 158.

Keenan *et al.*[106] also estimated the value of ε^{Xe} to be -11.1 V^{-1}. Since γ^{Xe} was used as a range, the same should be done for ε^{Xe} and the range used for all XeMX is $-5 \leq \varepsilon^{Xe} \leq -15$ V^{-1}.[33,34] Using this, the second term in equation [5.5] was determined to be approximately an order of magnitude smaller than the first term. Given the uncertainty associated with γ^{Xe} and the first term of equation [5.5], the second term can be ignored in semi-quantitative discussions. The expected eQq values can now be calculated using equation [5.4]. The resulting values are in Table 5.7 along with the experimental eQq values. The entire picture represented by equation

[5.5] accounts for less than 60% of the measured *eQq* values, suggesting again that electrostatics cannot be the sole explanation for the large noble gas *eQq* values.

Table 5.1 Ng-M Experimental[a] (expt) and *ab initio* (calc.) Bond Lengths (Å) of the Noble Gas-Noble Metal Halides and Related Complexes

Complex	*r*(Ng-M) (expt)	*r*(Ng-M) (calc.)[b]	*r*(M-X) (expt)[c]	*r*(M-X) (calc.)[b]
ArCuF[d]	2.22[e]	2.19 (2.24)	1.753 (1.745)[f]	1.722 (1.727)
ArCuCl[d]	2.27[e]	2.24 (2.30)	2.050 (2.051)[g]	2.038 (2.053)
ArCuBr[d]	2.29[e]	2.26	2.173 (2.173)[f]	2.168
$ArCu^{+}$[i]		2.36		
$ArCuAr^{+}$[j]		2.34		
KrCuF[k]	2.32	2.28 (2.32)	1.745[f,l]	1.73 (1.730)
KrCuCl[k]	2.36	2.31 (2.37)	2.051 (2.051)[g]	2.041 (2.055)
$KrCu^{+}$[i]		2.46		
$KrCuKr^{+}$[j]		2.42		
XeCuF[m]	2.43	2.46 (2.46)	1.745[l]	1.732 (1.737)
XeCuCl[m]	2.47	2.49 (2.50)	2.057 (2.051)[g]	2.048 (2.060)
ArAgF[n]	2.56[e]	2.56 (2.59)	1.986 (1.983)[f]	1.958 (1.972)
ArAgCl[n]	2.61[o]	2.59 (2.63)	2.269 (2.281)[g]	2.257 (2.272)
ArAgBr[n]	2.64[p]		2.380 (2.393)[q]	
KrAgF[r]	2.59	2.60 (2.61)	1.957 (1.983)[f]	1.964 (1.969)
KrAgCl[s]	2.64	2.63 (2.65)	2.268 (2.281)[g]	2.270 (2.271)
KrAgBr[t]	2.66	2.69	2.382 (2.393)[q]	2.397
XeAgF[u]	2.66	2.74 (2.68)	1.983[l]	1.961 (1.969)
XeAgCl[u]	2.70	2.78 (2.73)	2.270 (2.281)[g]	2.268 (2.274)
ArAuF[v]	2.39[e]	2.39 (2.40)	1.918[l,w]	1.949 (1.909)
ArAuCl[x]	2.47[e]	2.46 (2.47)	2.198 (2.199)[y]	2.218 (2.196)
ArAuBr[v]	2.50[e]	2.49	2.316 (2.318)[y]	2.332
$ArAuAr^{+}$[z]		2.54		
KrAuF[s]	2.46[aa]	2.45 (2.45)	1.918[l]	1.952 (1.913)
KrAuCl[x]	2.52	2.51 (2.52)	2.212 (2.199)[y]	2.223 (2.201)
$KrAuKr^{+}$[z]		2.57		

XeAuF[bb]	2.54[aa]	2.56 (2.54)	1.918[l]	1.910 (1.922)
Ar-NaCl[cc]	2.89			
ArHg[dd]	4.05			
Ar-HF[ee]	2.92			
Kr-HF[ff]	2.93			
Xe-HF[gg]	3.07			

[a] $r_m^{(2)}$ structures unless otherwise noted. [b] Values in parentheses were obtained from Reference 37. The other values were obtained from the references given with the molecular formulas. [c] Values in parentheses are the experimental r_e bond length obtained in MX monomer. [d] Reference 26. [e] r_o structure. [f] Reference 21. [g] Reference 18. [i] Reference 90. [j] Reference 35. [k] Reference 32. [l] r(M-X) fixed to r_e(M-X) in monomer. [m] This work. [n] Reference 25. [o] r_d structure. [p] r_s structure. [q] Reference 108. [r] Reference 29. [s] Reference 30. [t] Reference 31. [u] Reference 33. [v] Reference 28. [w] Reference 19. [x] Reference 27. [y] Reference 20. [z] Reference 36. [aa] $r_m^{(1)}$ structure. [bb] Reference 34. [cc] Reference 43. [dd] Reference 86. [ee] Reference 109. [ff] Reference 87. [gg] Reference 88.

Table 5.2 Comparison of Noble Gas-Noble Metal Bond Lengths (Å) in NgMX Complexes with Values Estimated from Standard Parameters

Standard Parameters:			
atom/ion	van der Waals radius (r_{vdW})[a]	ionic radius (r_{ion})	covalent radius (r_{cov})
Ar	1.88		0.94-0.95[b] (0.98)[c]
Kr	2.00		1.09-1.11[b]
Xe	2.18		1.30-1.31[b]
Cu^+/Cu(I)		0.60[d]	1.06[e]
Ag^+/Ag(I)		0.81[d]	1.28[e]
Au^+/Au(I)		0.77[d]	1.27[e]
Na^+		0.79[d]	

Bond Lengths (r(Ng-M in NgMX)):				
	r_{vdW}(Ng)+r_{ion}(M^+)	Experimental		r_{cov}(Ng)+r_{cov}(M(I))
ArCuX	2.48	2.22-2.30[f]		2.04
KrCuX	2.60	2.32-2.36[g]	...[h]	2.16
XeCuX	2.78	2.43-2.47[i]	...	2.37
ArAgX	2.69 ...	2.56-2.64[j]		2.26
KrAgX	2.81	2.59-2.66[k]		2.38
XeAgX	2.99	2.65-2.70[l]	...	2.58
ArAuX	2.65	2.39-2.50[m]	...	2.25
KrAuX	2.77	2.46-2.52[n]	...	2.37
XeAuF	2.95	2.54[o]	...	2.57
Ar-NaCl	2.67	2.89[p]		

[a] Reference 91. [b] Reference 93. [c] Reference 48. [d] These are the values for coordination number 2. All are calculated from $r(M^+) = r(MF) - r(F^-)$. The values for Cu^+ and Ag^+ are from Reference 92; those for Au^+ and Na^+ are from Reference 32. [e] Reference 110. [f] Reference26. [g] Reference 32. [h] Dots show which sum of radii is closer to the experimental bond lengths. [i] This work. [j] Reference 25. [k] Reference 29, 30, and 31. [l] Reference 33. [m] Reference 27 and 28. [n] Reference 31 and 28. [o] Reference 34. [p] Reference 43.

Table 5.3 Centrifugal Distortion Constants (D_J), Stretching Frequencies (ω), and Force Constants (k) of Noble Gas-Noble Metal Halides and Related Complexes

Complex	D_J/kHz $\times 10^2$	ω(NgM)/cm^{-1} e (a)[a]	ω(MX)/cm^{-1} a (m)[b]	k(NgM) /Nm^{-1}[c]	k(MX)* / Nm^{-1}[d]
ArCuF[f]	94	224 (228)	674 (621[g])	79	332[h]
ArCuCl[f]	34	197 (190)	456 (418[i])	65	228[j]
ArCuBr[f]	12	170 (164)	350 (313[k])	53	202[l]
KrCuF[m]	38	185 (198)	669 (621[g])	84	332[h]
KrCuCl[m]	15	162 (148)	441 (418[i])	70	228[j]
XeCuF[n]	20	178(169)	656(621[g])	94	332[h]
XeCuCl[n]	8	155(146)	445(418[i])	80	228[j]
ArAgF[o]	95	141 (127)	541 (513[p])	36	250[q]
ArAgCl[o]	35	135 (120)	357 (344[r])	34	186[s]
ArAgBr[o]	11	124	(251[t])	30	169[u]
KrAgF[v]	31	125 (113)	544 (513[p])	48	250[q]
KrAgCl[w]	13	117 (105)	352 (344[r])	43	186[s]
KrAgBr[x]	4	106 (89)	255 (247[t])	38	169[u]
XeAgF[y]	14	130 (108)	546 (513[p])	64	250[q]
XeAgCl[y]	6	120 (99)	356 (344[r])	58	186[s]
ArAuF[z]	51	221 (214)	583 (544[aa])	97	302[bb]
ArAuCl[cc]	21	198 (184)	413 (383[dd])	78	257[ee]
ArAuBr[z]	6	178 (165)	286 (264[dd])	65	231[ff]
KrAuF[gg]	16	176 (184)	(544[aa])	110	302[bb]
KrAuCl[cc]	8	161 (163)	409 (383[dd])	94	257[ee]
XeAuF[hh]	7	164 (165)	(544[aa])	137	302[bb]
Ar-NaCl[ii]	900	21		0.6	
ArHg[jj]		(22)			
Ar-HF[kk]	7210	42			
Kr-HF[ll]	3190	43			
Xe-HF[mm]	1820	45			

[a]e = experimental values which for the NgMX complexes have been derived from the centrifugal distortion constants using a diatomic approximation. a = ab initio values.
[b]c = *ab initio* values obtained for the MX bond in the complexes. m = the values obtained for the MX monomers from experimental results.
[c]Force constant k derived from ω(Ng-M) using a diatomic approximation.
[d] Force constant k obtained for MX monomer, calculated from ω(M-X) using equation [2.21].
[e] Reference 26. [f] Reference 21. [g] Reference 111. [h] Reference 112.
[i] Reference 32. [j] This work. [k] Reference 25. [l] Reference 113.
[m] Reference 114. [n] Reference 115. [o] Reference 29. [p] Reference 30.
[q] Reference 31. [r] Reference 33. [s] Reference 27. [t] Reference 116, with apparent typographical error corrected. [u] Reference 28. [v] Reference 20.
[w] Reference 34. [x] Reference 43. [y] Reference 86. [z] Reference 109.
[aa] Reference 87. [bb] Reference 88.

Table 5.4 ^{63}Cu Nuclear Quadrupole Coupling Constants (MHz) in NgCuX Complexes and Related Species

Molecule	$eQq(^{63}Cu)$		
	X = F	X = Cl	X = Br
CuX	21.956[a]	16.16908[b]	12.8510[b]
ArCuX	38.056[a]	33.186[a]	29.92[a]
KrCuX	41.77[c]	36.52[c]	-
XeCuX	47.76(11)[d]	41.57(6)[d]	-
$XCuX^-$	-	61.4[e]	57.7[f]
OCCuX	75.41[g]	70.83[g]	67.53[g]

[a]Reference 26. [b]Reference 24. [c]Reference 32. [d]This work. [e]Reference 96. [f]Reference 117. [g]Reference 98.

Table 5.5 ^{35}Chlorine Quadrupole Coupling Constants (MHz) in CuCl, NgCuCl and Related Species

Parameter	CuX	ArCuX	KrCuX	XeCuX	$XCuX^-$	OCCuX
$eQq(^{35}Cl)$	-32.12729[a]	-28.032[b]	-27.30[c]	-26.01[d]	-19.3[e]	-21.474[f]

[a]Reference 18. [b]Reference 26. [c]Reference 32. [d]This Work.
[e]Reference 117. [f]Reference 98.

Table 5.6 ^{83}Kr and ^{131}Xe Nuclear Quadrupole Coupling Constants (MHz) for Various Kr- and Xe-Containing Species[a]

Molecule	$eQq(^{83}Kr)$	Reference	Molecule	$eQq(^{131}Xe)$	Reference
Kr	0		Xe	0	
Kr-Ne	-0.52	10	Xe-Ne	0.39	100
Kr-Ar	-0.85	10	Xe-Ar	0.72	100
Kr-HCl	5.20	118	Xe-HCl	-4.9	106
KrCuF	128.79	32	XeCuF	-87.8	this work
KrAgF	105.10	29	XeAgF	-82.8	33
KrAuF	185.94	31	XeAuF	-134.5	34
KrD^+	549	119	XeH^+	-369.5	120
Kr^+	915	102	$Xe([Kr]4d^{10}5p^5 6s^1)$	-505	101

[a] The quadrupole moments (Reference 121) of ^{83}Kr and ^{131}Xe are +25.9(1) fm^2 and -11.4(1) fm^2, respectively.

Table 5.7 ^{131}Xe Nuclear Quadrupole Coupling Constants Resulting from Polarization Due to External Charges

Complex	μ^a	$q_{eff}{}^b$	E_{zz} (M)	E_{zz} (F)	$E_{zz}{}^c$	eQq (MHz) Calculated[d]	eQq (MHz) experimental
XeCuF	5.77	0.69	-1.385	0.273	-1.112	-51	-87.8
XeCuCl	5.2	0.53	-1.017	0.165	-0.852	-39	-81.4
XeAgF[e]	6.22	0.65	-0.992	0.187	-0.805	-35	-82.8
XeAgCl[e]	6.08	0.56	-0.812	0.130	-0.681	-30	-78.2
XeAuF[f]	3.4	0.37	-0.646	0.120	-0.526	-23	-134.5

[a] μ is the dipole moment (Debye) of the MX monomer.
[b] Fractional charge of the M^+ and F^- ions (Calculated from equation [5.9]).
[c] E_{zz} is the sum of the field gradients at the Kr nucleus due to the M^+ and F^- ions alone (E_{zz}(M) and E_{zz}(X), respectively). Units are 10^{20} Vm^{-2}.
[d] Calculated using eqs. [5.4] and [5.5] with $\gamma^{Xe} = 158$; the second term of eq. [5.5] is negligible. The uncertainty for the Xe coupling constants is ± ~4 MHz.
[e] Reference 33.
[f] Reference 34.

Chapter 6

Ab Initio Calculations

The results of several calculations were used to help interpret the experimental results. The first of these was the *ab initio* results of Lovallo and Klobukowski,[37] which predicted geometries and dissociation energies. However, these did not study these molecules in enough depth. Reference 37 did not present vibrational frequencies, nor any information on electron distributions. Accordingly a second set of *ab initio* calculations was performed which produced not only new values for the geometries and dissociation energies, but also the extra information needed. In addition, some semi-empirical calculations of induction energies were performed in an effort to understand the values of the dissociation energies. This chapter describes the results from all of these calculations and the implications drawn from them.

The new *ab initio* calculations were performed at the second order Møller-Plesset (MP2) level of theory,[77] using the GAUSSIAN 03 suite of programs.[122] They produced geometries, vibrational frequencies, dissociation energies, Mulliken and Natural Bond Orbital populations, MOLDEN plots of electron densities and local energy densities. These results are discussed in the following sections.

The basis sets used in the new calculations were the following. The simple 6-311** basis set was used for the F atom.[80] For the chlorine atom the (631111s/52111p) McLean-Chandler basis set[83] was used augmented with one d-polarization function ($\alpha_d = 0.75$).[82] The basis set for the Cu atom used an effective core potential (ECP) which left 19 valence electrons ($3s^2 3p^6 3d^{10} 4s^1$). The ECP and the optimized Gaussian basis set (31111s/22111p/411d) were taken from Andrae et al.[81] The Cu basis set was augmented with two f-functions, $\alpha_f = 3.1235$ and $\alpha_f = 1.3375$.[82] For Xe the pseudopotential from the Stuttgart/Köln group was used along with the corresponding basis set. The ECP46MWB scheme was used with the contraction (6s6p3d1f)/[4s4p3d1f][123,124] to complete the Xe basis set.

Basis set superposition error (BSSE) was accounted for with the counterpoise correction method of Boys and Bernardi.[125,126] Although these basis sets and programs are different from those of Reference 37, comparable results were obtained for the geometries and dissociation energies as indicated in the sections below.

6.1 Geometries and Vibration Frequencies

The geometries of both XeCuF and XeCuCl were constrained to be linear. The bond lengths from the present calculations are compared with the experimental values and those of Lovallo and Klobukowski[37] in Table 5.1 (page 74), along with corresponding parameters of other noble gas – noble metal halides and related molecules and ions.

The main parameter of interest is the Ng-M bond length. The values of r(Xe-Cu) from the present work and from Reference 37 agree well. However, in both cases the agreement with experiment could be better. This extends to other Ng-Cu bonds and to Ng-Ag bonds; however, perhaps surprisingly, the agreement between theory and experiment is better for NgAu bonds. An encouraging result, even with disagreements with experiments, is that in all cases the *ab initio* calculations predict short NgM bonds in the NgMX molecules. The agreement between theory and experiment is much better for the M-X bonds. However, for XeCuCl, the *ab initio* value from Reference 37 agrees better with experiment than the present one.

The *ab initio* stretching frequencies ω(Xe-Cu) obtained for the XeCuX molecules are compared in Table 5.3 (page 77) with the values obtained from experiment. Corresponding values for several related compounds are also included in the Table. Comparison of the *ab initio* ω(NgM) values with those derived from the distortion constants reveals that in general the calculated values are slightly smaller than those derived from experiment. This is possibly the result of using the pseudo-diatomic approximation for the latter. Nonetheless, the agreement is excellent.

The *ab initio* ω(MX) values for the metal halide bonds shown in Table 5.3 agree well with the experimental values for the MX monomers, though they are slightly smaller.

Overall the results of the *ab initio* calculations have provided a satisfactory model of the NgMX molecules. It is to be hoped that as theoreticians produce more sophisticated and accurate basis sets (particularly for the large atoms) better agreement with experiment will be obtained.

6.2 Dissociation Energies

XeCu bond dissociation energies D_e in for XeCuX have been calculated in the present work. They are compared with those for Reference 37 in columns 6 and 7 of Table 6.1. In addition, Table 6.1, which is an extension of Table 12 in Reference 31, contains corresponding NgM dissociation energies for other NgMX molecules previously studied.

In order to account for BSSE, D_e for XeCuX has been calculated using the so-called Bootstrap method in the following equation:[125]

$$D_e = \varepsilon(NgMX) - \varepsilon(BqMX) - \varepsilon(NgBqBq) + \left[\varepsilon(MX, r_c) - \varepsilon(MX, r_e)\right]. \qquad [6.1]$$

Here ε (NgMX) is the energy of the complex using its full basis set, ε (BqMX) is the energy of MX including the orbitals of the noble gas as part of the basis set, ε (NgBqBq) is that of the noble gas with the MX orbitals as part of its basis set, and the term $\left[\varepsilon(MX, r_c) - \varepsilon(MX, r_e)\right]$ is the difference in the energy of MX at the bond length in the molecule (r_c) and the equilibrium bond length in the monomer (r_e). This is in effect the application of the counterpoise correction.

The trends in the NgM dissociation energies can be easily seen in Table 6.1. The values for ArM are somewhat smaller than the corresponding values for KrM, which in turn are significantly smaller than the XeM values. Also, the dissociation energies increase as the metal is changed from Ag to Cu to Au, with Au-containing molecules showing some very large values.

The values calculated for the NgMX molecules are much larger than the dissociation energy calculated for the van der Waals complex Ar-NaCl.[43]

The NgM dissociation energies from our laboratory, including those of XeCuX, agree well with those of Lovallo and Klobukowski,[37] in general to within a few kJ mol^{-1}. This is especially true for the complexes containing Cu and Au. In these cases the values are large, and approach the values expected for chemical bonds. The average values of D_e(KrF) and D_e(XeF) in KrF_2 and XeF_2 are 49 kJ mol^{-1} and 134 kJ mol^{-1}, respectively.[93]

The *ab initio* NgM dissociation energies in Table 6.1 increase roughly monotonically with the stretching force constants in Table 5.3. Such a relationship is to be expected if the Ng-M bond can be described by a Morse potential. This potential has the form:[53]

$$U(r-r_e) = D_e(1-e^{-\beta(r-r_e)})^2 \qquad [6.2]$$

where r is the bond length, r_e is the equilibrium bond length, D_e is the dissociation energy and β is the Morse potential constant (empirical). The force constant is related to D_e and β by the following equation:

$$k = 2D_e\beta^2. \qquad [6.3]$$

Accordingly, if the Morse potential model holds for the NgMX molecules, then experimental k and the *ab initio* D_e should be directly proportional. Figure 6.1 shows a plot of the experimental force constants versus the dissociation energies calculated by Lovallo and Klobukowski.[37] A linear relationship exists for the NgMX molecules, but each noble gas-containing molecule has a different β value indicated by a different slope in the plot. Therefore, the measurement of rotational constants and centrifugal distortion constants (used in calculating the force constant) provide an indirect, approximate measurement of D_e.

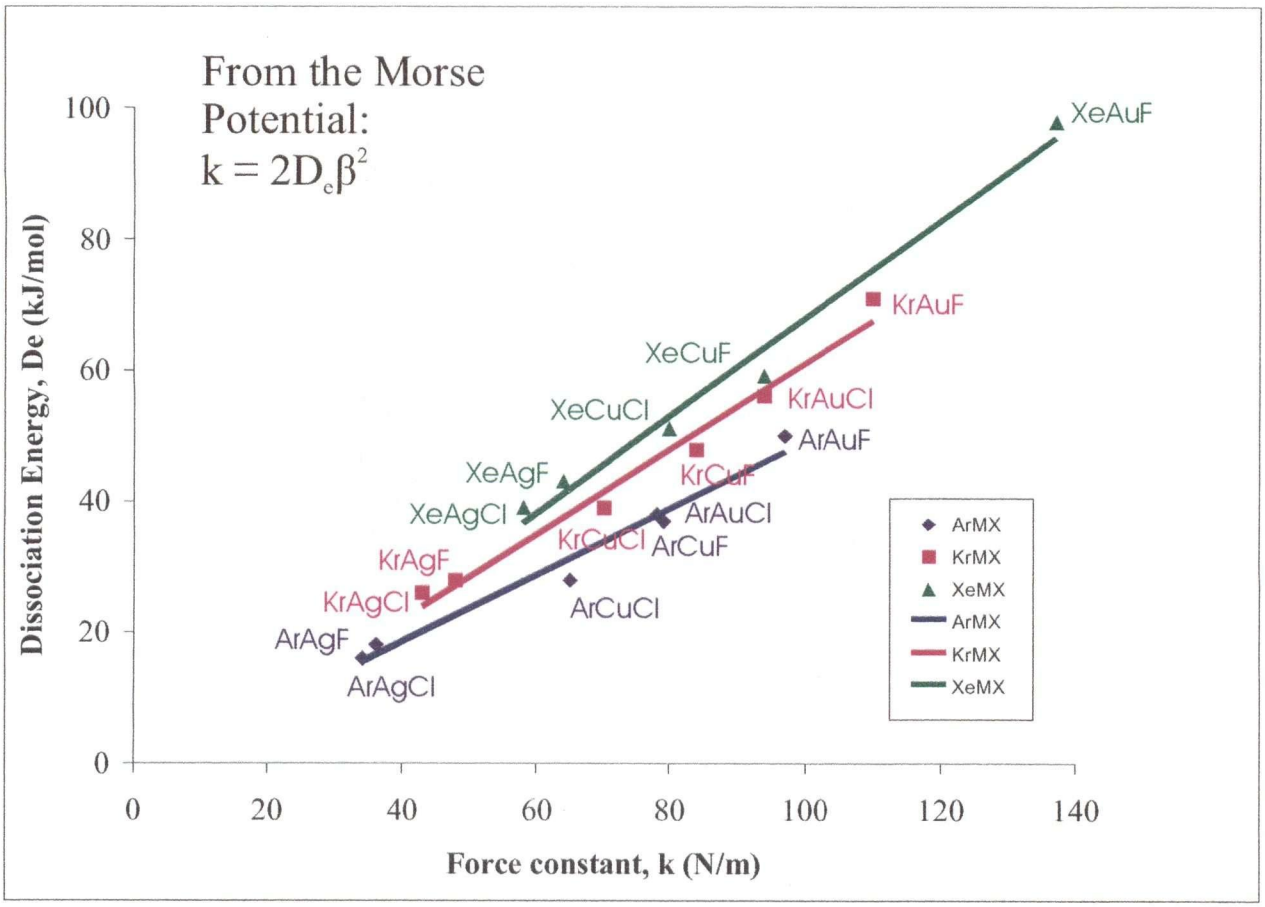

Figure 6.1 Plot of *ab initio* dissociation energies,[37] D_e, versus experimental force constant obtained in Section 5.2 for the Ng-M bond in the NgMX molecules.

In a discussion of the nature of the NgM bonding the possibility must be considered that the large D_e values arise through purely electrostatic interactions between the noble gas and the metal halide. The present work deals primarily with XeCuX. The leading term is the induction energy between the noble gas and the noble metal halide.

Two approaches have been taken. One considers a dipole-induced dipole interaction and the second considers a charge-induced dipole term where the charge is that of the positive charge of the metal ion.The dipole moments and charges used in these calculations were the same values as those used in the Sternheimer shielding calculation in Chapter 5. The dipole-induced dipole energy is calculated using the following equation: [Reference 127, equation 10.16]

$$E_{ind} = -2\left(\frac{\alpha}{4\pi\varepsilon_o}\right)\frac{\mu^2}{4\pi\varepsilon_o r^6} \qquad [6.4]$$

where the $\left(\frac{\alpha}{4\pi\varepsilon_o}\right)$ is the polarizability of the noble gas, the μ is the MX dipole moment and r is the distance from the noble gas nucleus to the centre of the charge of MX dipole $\left(= r_{NgM} + r_{MX}/2\right)$. The dipole-induced dipole induction energies are included in Table 6.1 for all NgMX molecules and for Ar-BeO and Ar-NaCl. It should be noted that this value accounts for 20% or less of the calculated dissociation energy in the NgMX molecules.

Equation [6.4] is valid when the contributions from both ends of the permanent dipole are approximately the same and this generally occurs at long distances. The effects in the NgMX molecules can probably be more realistically accounted for by considering the individual charges at each end of the dipole. Since the Ng-X distance is much larger than the Ng-M distance, only the Ng-M contribution will be considered as an upper limit. The contribution from the Ng-X end of the dipole would be of opposite sign and approximately 10% of the Ng-M contribution.

The charge-induced dipole induction energy is calculated as in Reference 31 by: [Reference 127, equation 10.14]

$$E_{ind} = -\left(\frac{\alpha}{4\pi\varepsilon_o}\right)\frac{q_{eff}^2}{8\pi\varepsilon_o r^4} \qquad [6.5]$$

where the terms have the same definitions as previously stated except that now r is the Ng-M internuclear distance. The charge-induced dipole contributions are shown in Table 6.1; it can be seen that they too do not fully account for the *ab initio* D_e for all NgMX. For the Ar-NaCl and Ar-BeO van der Waals complexes, the charge-induced dipole induction energies more than fully account for the calculated dissociation energies.

Some notes should be made about these induction energies. First of all, the equations used assume a long-distance approximation which may not be entirely valid and the induction energies may be greater by about 50%. This would make the values for NgAgX roughly the D_e values. However, for NgCuX (especially XeCuX) the values would still be lower than the D_e values, and those of NgAuX would be much lower. Secondly, there are several other, smaller, attractive contributions to E_{ind}, plus dispersion terms. However, they are all counterbalanced by a significant repulsion energy term[128] Overall, the charge-induced dipole term is probably as good a value as any to use for the comparison with D_e.

6.3 Populations

The populations of the orbitals for both XeCuF and XeCuCl have been calculated. Of particular interest are the changes in the orbital populations on molecule formation. These are determined by calculating the orbital populations of the noble gas and the metal halide when they are separated and then when they are in the NgMX molecule. Any changes in the orbital populations can be attributed to electron distribution rearrangement on complex formation. Two methods were used to calculate orbital populations.

6.3.1 Mulliken Populations

Mulliken populations are an analysis method of Self-Consistent-Field (SCF) wave functions introduced by Mulliken. This method distributes the electrons of an n-electron

molecule into net populations n_r in the basis functions χ_r and overlap populations $n_{r\text{-}s}$ for all pairs of basis functions possible.[129] The sum of the populations of occupied molecular orbitals produces the Mulliken net population and the overlap populations. The sum of the net populations and the overlap populations equals the total number of electrons in the molecule.

The Mulliken populations calculated for XeCuF and XeCuCl are shown in Table 6.2. The populations of certain orbitals on the noble gas and the metal incur significant changes on molecule formation. The $n_{p\sigma}$ orbital on the noble gas loses electron density and the metal n_s and $n_{p\sigma}$ orbitals gain approximately the same amount of electron density. This can be interpreted as the donation of electron density from the noble gas to the metal. The populations of the orbitals on the halides do not show significant gain or loss of electron density on molecule formation. Table 6.2 also shows the charge on each atom in the molecule and the significant change that occurs on molecule formation. The charge on the Xe increases from 0 to 0.15-0.21. This implies significant charge redistribution on molecule formation.

In Table 6.3, the changes in Mulliken populations are shown for the entire noble gas – noble metal halide series studied to date. The changes are presented for key orbitals that have shown to have significant charge redistribution on molecule formation. This table shows a loss of electron density at $n_{p\sigma}$ orbital on the noble gas and a gain at the n_s and $n_{p\sigma}$ orbitals on the metal for all NgMX molecules. The amount of the donation increases as the noble gas is changed from Ar to Kr to Xe and as the metal is changed from Ag to Cu to Au.

6.3.2 Natural Bond Orbital Population

The natural population analysis was introduced by Reed *et al.* in 1985 as an improvement on the Mulliken population analysis.[129] First a set of orthonormal natural atomic orbitals (NAOs) is calculated and from them is calculated a set of orthonormal natural bond orbitals (NBOs). Each NBO is classified as a core, lone pair or bond orbital.[129] A population analysis is

done using the NBOs. According to Reference 129, the net atomic charge obtained by natural bond analysis method show less basis set dependence than the Mulliken populations.

Table 6.4 shows the NBO populations obtained for XeCuF and XeCuCl. The changes of the orbital populations upon molecule formation follow trends similar to those established with the Mulliken population analysis. There is a donation of electron density from the noble gas to the noble metal. However, in this case the metal gains the electron density only in the n_s orbital only instead of in both the n_s and the $n_{p\sigma}$ orbitals as suggested in the Mulliken populations. The magnitude of the electron donation from the noble gas to the metal is somewhat smaller than in the Mulliken population analysis but remains significant nonetheless.

Table 6.5 shows the changes in NBO populations for certain orbitals of some of the noble gas – noble metal halides studied. The noble gas donates electron density from the $n_{p\sigma}$ orbital to the n_s and $n_{p\sigma}$ orbitals on the metal for all the molecules in the Table. The donation increases as the noble gas is changed from Ar to Kr to Xe, consistent with experimental results. Similarly, the donation increases as the metal is changed from Ag to Cu to Au. The donation from the noble gas to the metal in all cases is significant and is consistent with a weak chemical bond being present between the noble gas and the noble metal.

Recent improvements in population analysis methods such as the NBO population analysis have suggested that the Mulliken populations should no longer be used.[129] However, this study has found no significant qualitative difference in the results obtained from using either the Mulliken population or the Natural Bond Orbital population method. The trends seen in both methods are similar and consistent with the experimental results.

6.4 MOLDEN Plots

Electron density contour plots were generated from the results of the GAUSSIAN 03 calculations using the MOLDEN 3.4 program.[130] In particular, plots were generated for the valence molecular orbitals for XeCuF and XeCuCl. Two such plots are in Figure 6.2 for XeCuF

and Figure 6.3 for XeCuCl. The values of the contours are n = ~0.02 with n = 1-13 or n = 1-25; the different colours indicate opposite signs for the MO wave functions. Large orbital overlap between Xe and Cu is found for both molecules, consistent with the possibility of XeCu covalent bonding. In both cases, the σ-overlap, between Xe ($5p_z$) and Cu ($3d_{z^2}$) is significantly greater than the π-overlap between Xe ($5p_x$) and Cu ($3d_{xz}$), suggesting that any covalent bonding arises primarily from the σ-overlap.

6.5 Local Energy Densities

As will be discussed in the next chapter, both the experimental and theoretical results suggest that the Ng-M bonds in NgMX (and in the present Xe-Cu in XeCuX) are rather stronger than van der Waals bonds. The evidence thus far seems consistent with weak covalent bonding.

The conventional picture of a covalent bond is that shared electron density is localized between the bound nuclei, to become the "glue" which holds the atoms together. However, it is non trivial to find a specific, experimental or theoretical, criterion from which a distinction between covalent and noncovalent bonds can be made. Possible *ab initio* criteria for whether a covalent bond is present have been discussed in a 1990 review by Frenking and Cremer.[84]

The simplest method by far to do this (and possibly the least ambiguous) was first suggested by Cremer and Kraka.[131] This involves evaluating the so-called local energy density distribution ($H(r)$) at the bond critical point (r_B) along the path of maximum energy density (MED) between the atoms. $H(r)$ is in turn written as:[131,132]

$$H(r) = G(r) + V(r) \qquad [6.6]$$

where $G(r)$ is the local kinetic energy density distribution and $V(r)$ is the local potential energy density distribution. If $H(r)$ is negative at the bond critical point then the potential energy dominates and electron density will accumulate to give a covalent bond. On the other hand, if $H(r)$ is zero or positive the interaction will be closed shell, as in ionic bonding, van der Waals bonding or hydrogen bonding.[132] The bond critical point is the point at which there are equal

contributions to the molecular orbitals from the atoms involved in the bond. The required values were obtained from the wave functions from results of the *ab initio* calculations using Bader's program AIMPAC, obtained from Reference 133. The MED path is the straight NgM intermolecular path. This program also identifies the bond critical point and the value of $H(r)$ at that point.

Table 6.6 presents the local energy density distributions at the bond critical bond in Hartree $Å^{-3}$ for XeCuF and XeCuCl along with the values obtained for other related molecules. *H(r)* is negative for both XeCuX molecules indicating a weak XeCu covalent bond. In fact, *H(r)* is negative for all NgCuX and XeAuF shown in the table, suggesting that all contain a NgM covalent bond. The magnitude of the negative *H(r)* term increases as the noble gas is changed from Ar to Kr to Xe. Also XeAuF has a significantly larger negative *H(r)* value which is consistent with previous assumptions stating that the XeAu bonding would be strongest.

Frenking and Cremer[84] also point out that a negative *H(r)* value should be expected when the *ab initio* dissociation energy is significantly greater than the charge-induced dipole induction energy. This is the case for all NgMX molecules.

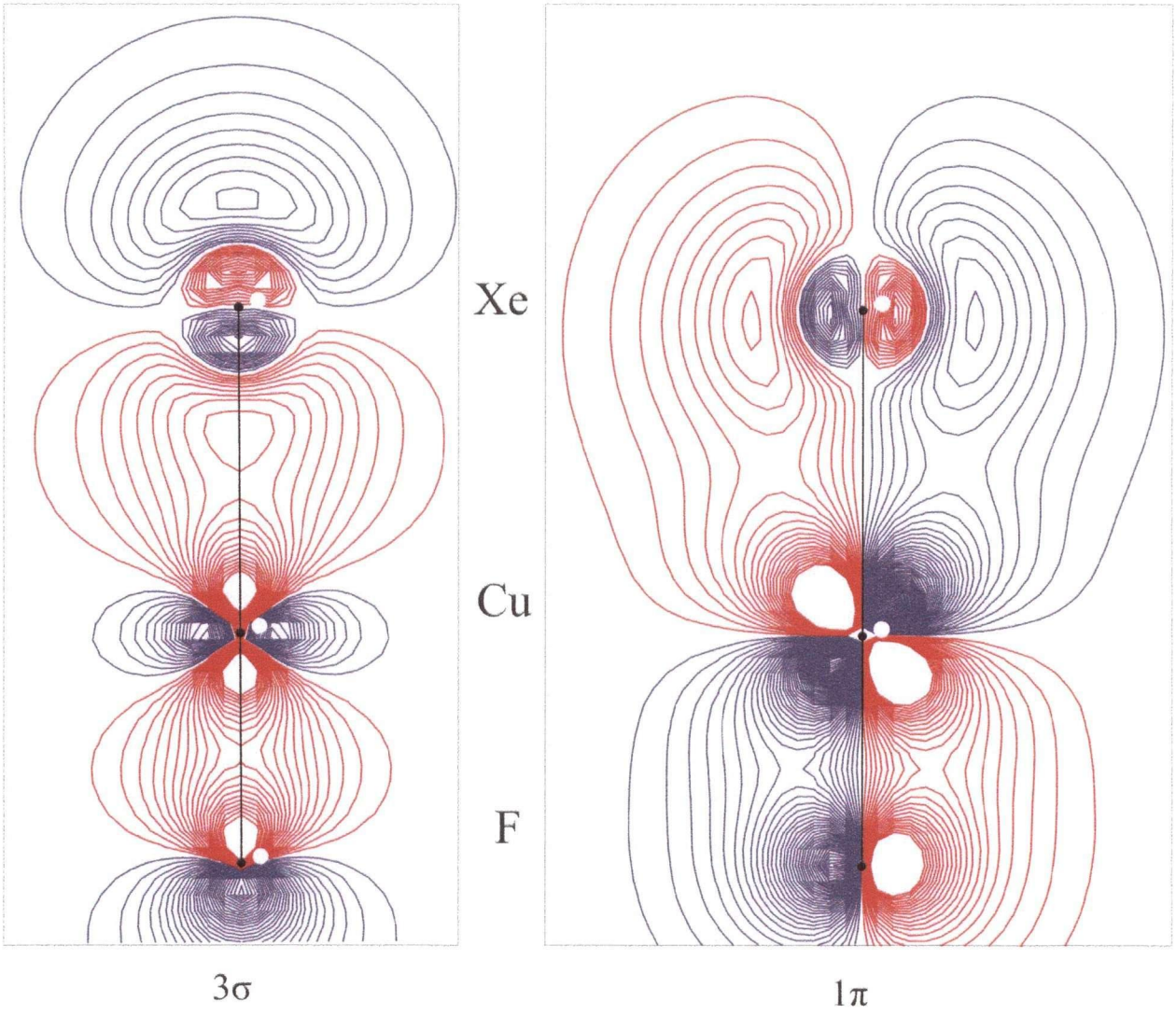

Figure 6.2 MOLDEN contour diagrams of two occupied valence molecular orbitals of XeCuF; in each case, the value of the contours is n = 0.02 with n = 1-13. The different colours indicate opposite signs of the wave functions.

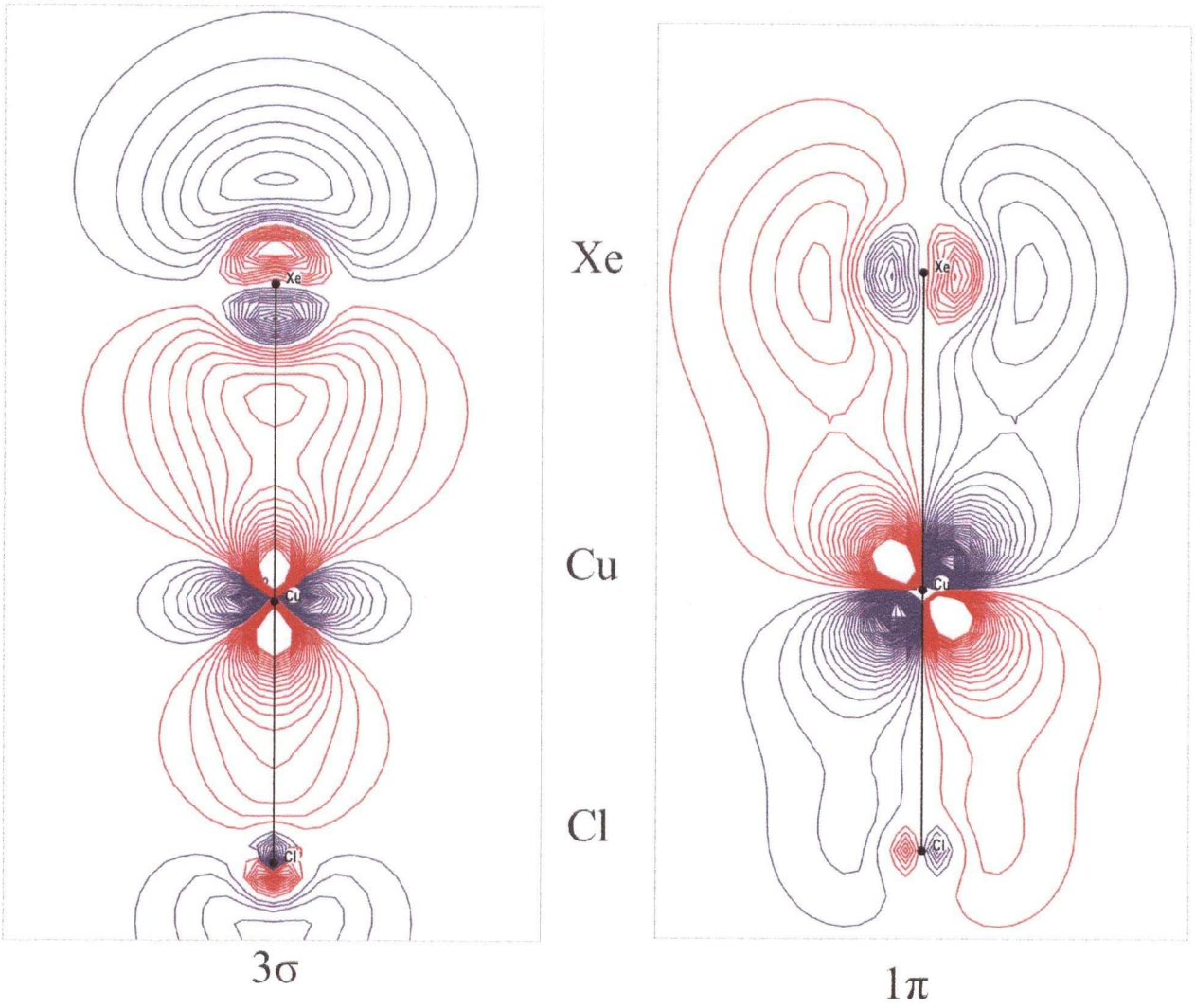

Figure 6.3 MOLDEN contour diagrams of two occupied valence molecular orbitals of XeCuCl; in each case, the value of the contours is n = 0.02 with n = 1-25. The different colours indicate opposite signs of the wave function.

Table 6.1 Comparison of MX Dipole Moments and Effective Atomic Charges, Induction Energies and *ab initio* Ng-M Dissociation Energies of NgMX Complexes

Complex	MX		$-E_{ind}$		D_e[e]	
	μ[a]	q_{eff}[b]	dip.–ind.dip.[c]	chg.–ind.dip.[d]	Our work[f]	Lovallo and Klobukowski[g]
ArCuF	5.77[h]	0.69	8	22	44[i]	37
ArCuCl	5.2[i]	0.53	4	13	33[i]	28
KrCuF	5.77[h]	0.69	9	28	45[j]	48
KrCuCl	5.2[i]	0.53	5	16	37[j]	39
XeCuF	5.77[h]	0.69	12	38	63[k]	59
XeCuCl	5.2[i]	0.53	7	21	55[k]	51
ArAgF	6.22[h]	0.65	4	11	14[g]	18
ArAgCl	6.08[l]	0.55	3	8	14[l]	16
KrAgF	6.22[h]	0.65	5	16	17[g]	28
KrAgCl	6.08[m]	0.55	4	11	15[g]	26
KrAgBr	5.62[n]	0.49	3	8	17[g]	
XeAgF	6.22[h]	0.65	8	24[n]	36[o]	43
XeAgCl	6.08[m]	0.55	6	16[n]	33[o]	39
ArAuF	3.4[i]	0.37	2	5	55[i]	50
ArAuCl	3.1[i]	0.29	1	3	42[i]	38
KrAuF	3.4[j]	0.37	3	6	58[i]	71
KrAuCl	3.1[i]	0.29	1	4	44[i]	56
XeAuF	3.4[i]	0.37	4	11	101	97
Ar-NaCl	9.00[p]	0.79	4	10	8[q]	
Ar-BeO	7.2[r]	0.84	26	84	45[r]	

[a] μ is the dipole moment (Debye) of the MX monomer.
[b] q_{eff} is the effective charge of the metal ion to produce the value of μ at the molecular bond length. It is in fractions of an elementary charge. Values from Reference 31.
[c] Dipole-induced dipole induction energy (kJ mol^{-1}).
[d] Charge-induced dipole induction energy (kJ mol^{-1}).

[e] D_e in kJ mol^{-1}.
[f] Values account for BSSE unless otherwise noted.
[g] Reference 37. [h] Reference 21. [i] Reference 31. [j] Reference 32.
[k] Present work. [l] BSSE unaccounted for. [m] References 134. [n] Reference 135.
[m] Reference 33. [o] References 136 and 137. [p] Reference 43. [q] Reference 44.

Table 6.2 Mulliken Valence Orbital Populations (n) for Xe, CuF, XeCuF, CuCl and XeCuCl

Orbital Population	Xe+CuF	XeCuF		Xe+CuCl	XeCuCl
Xe			Xe		
q	0	0.21		0	0.15
n_s	2.00	1.95		2.00	1.98
$n_{p\sigma}$	2.00	1.83		2.00	1.85
$n_{p\pi}$	4.00	3.98		4.00	3.99
$n_{d\sigma}$	2.00	2.00		2.00	2.01
$n_{d\pi}$	4.00	4.02		4.00	4.01
$n_{d\delta}$	4.00	4.00		4.00	4.00
Cu			Cu		
q	0.64	0.41		0.49	0.35
n_s	0.22	0.41		0.32	0.36
$n_{p\sigma}$	0.05	0.09		0.12	0.22
$n_{p\pi}$	0.11	0.10		0.10	0.09
$n_{d\sigma}$	1.93	1.91		1.96	1.94
$n_{d\pi}$	4.05	4.08		4.04	4.05
$n_{d\delta}$	4.00	4.00		4.00	4.00
F			Cl		
q	-0.64	-0.62		-0.49	-0.50
n_s	1.99	2.00		2.01	1.98
$n_{p\sigma}$	1.81	1.81		1.68	1.66
$n_{p\pi}$	3.84	3.81		3.93	3.85

Table 6.3 Changes in Mulliken populations on complex formation

	Ng		M		
	Δn_s	$\Delta n_{p\sigma}$	Δn_s	$\Delta n_{p\sigma}$	$\Delta n_{d\sigma}$
ArCuF[a]	0	-.08	.12	.02	-.05
ArCuCl[a]	0	-.08	.07	.04	-.04
ArCuBr[a]	0	-.08	.08	.04	-.02
KrCuF[b]	-.01	-.12	.12	.04	-.04
KrCuCl[b]	-.02	-.12	.09	.07	-.03
XeCuF[c]	-.05	-.17	.19	.04	-.02
XeCuCl[c]	-.02	-.15	.05	.10	-.02
ArAgF[d]	0	-.04	.07	0	-.02
ArAgCl[d]	0	-.04	.05	-.01	-.02
ArAgBr[d]	0	-.04	.03	-.01	-.01
KrAgF[e]	0	-.07	.09	.01	-.03
KrAgCl[f]	0	-.06	.08	-.01	-.03
KrAgBr[g]	0	-.06	.05	-.01	-.02
XeAgF[h]	0	-.04	.07	0	-.04
XeAgCl[h]	0	-.04	.10	-.03	-.04
ArAuF[i]	0	-.12	.18	.05	-.09
ArAuCl[j]	-.02	-.12	.13	.04	-.05
ArAuBr[i]	-.02	-.11	.17	.05	-.04
KrAuF[g]	-.02	-.19	.22	.07	-.09
KrAuCl[j]	-.03	-.17	.17	.07	-.06
XeAuF[k]	-.06	-.24	.14	.19	-.10

[a] Reference 26. [b] Reference 32. [c] Present work. [d] Reference 25.
[e] Reference 29. [f] Reference 30. [g] Reference 31. [h] Reference 33.
[i] Reference 27. [j] Reference 28. [k] Reference 34.

Table 6.4 Natural Bond Orbital Populations (n) for Xe, CuF, XeCuF, CuCl and XeCuCl

Orbital Population	Xe+CuF	XeCuF		Xe+CuCl	XeCuCl
Xe			Xe		
q	0	0.08		0	0.08
n_s	2.00	1.98		2.00	1.98
$n_{p\sigma}$	2.00	1.93		2.00	1.92
$n_{p\pi}$	4.00	4.00		4.00	4.00
$n_{d\sigma}$	2.00	2.00		2.00	2.01
$n_{d\pi}$	4.00	4.00		4.00	4.00
$n_{d\delta}$	4.00	4.00		4.00	4.00
Cu			Cu		
q	0.87	0.77		0.84	0.73
n_s	0.16	0.30		0.17	0.31
$n_{p\sigma}$	0.01	0.01		0.01	0.01
$n_{p\pi}$	0.03	0.04		0.01	0.01
$n_{d\sigma}$	1.93	1.90		1.97	1.94
$n_{d\pi}$	3.99	3.99		4.00	3.99
$n_{d\delta}$	4.00	4.00		4.00	4.00
F			Cl		
q	-0.87	-0.85		-0.84	-0.81
n_s	1.99	1.97		1.98	1.96
$n_{p\sigma}$	1.91	1.90		1.87	1.86
$n_{p\pi}$	3.97	3.97		3.99	3.99

Table 6.5 Changes in Natural Bond Orbital populations on complex formation

	Ng		M		
	Δn_s	$\Delta n_{p\sigma}$	Δn_s	$\Delta n_{p\sigma}$	$\Delta n_{d\sigma}$
ArCuF[a]	-.009	-.04	.13	0	-.051
ArCuCl[a]	-.010	-.04	.11	0	-.028
KrCuF[b]	-.012	-.05	.14	0	-.045
KrCuCl[b]	-.014	-.06	.13	0	-.028
XeCuF[c]	-.015	-.07	.14	0	-.035
XeCuCl[c]	-.017	-.08	.15	0	-.023
XeAgF[d]	-.01	-.05	.12	0	-.03
XeAgCl[d]	-.01	-.06	.12	0	-.02
XeAuF[e]	-.03	-0.14	.21	0	-0.05

[a] Reference 26. [b] Reference 32. [c] Present work. [d] Reference 33.
[e] Reference 34.

Table 6.6 Calculated Local Energy Densities (*H(r)*) for several NgMX molecules

	H(r) Hartree $Å^{-3}$
ArCuF[a]	-0.015
ArCuCl[a]	-0.015
KrCuF[a]	-0.040
KrCuCl[a]	-0.039
XeCuF[b]	-0.070
XeCuCl[b]	-0.067
XeAgF[a]	-0.054
XeAgCl[a]	-0.046
XeAuF[c]	-0.18

[a] Unpublished results. [b] Present work. [c] Reference 34.

Chapter 7

Conclusion

The rotational spectra of XeCuF and XeCuCl were measured and the rotational, centrifugal distortion and hyperfine constants were obtained. The supporting theoretical study produced geometries, stretching frequencies, dissociation energies, and information on the electron distributions of the molecules.

The XeCu bond has been found to be much stronger than typical van der Waals bonds. The first indicator of strong interactions is the unusually short XeCu bond, which is reproduced by the *ab initio* results. The experimental XeCu bond length is much shorter than the van der Waals limit and is approaching the covalent limit. Such short NgM bond lengths were first noticed with the $ArAgX$[25] molecules, and have continued to be found for all NgMX molecules.[25-34] The NgM bond lengths increase as the noble gas is changed from Ar to Kr to Xe and as the metal is changed from Ag to Cu to Au.

The second indicator is the small centrifugal distortion constants, which are much smaller than those expected for van der Waals complexes. Similar small values have been found for all the NgMX molecules. They imply that all the NgM bonds, including XeCuF and XeCuCl, are much more rigid than van der Waals bonds. The stretching frequencies for the XeCu bond, obtained from the centrifugal distortion constants and the rotational constants using a diatomic approximation, are larger than values typically found in van der Waals complexes, and approach values for weak chemical bonds. They too are consistent with values for all other NgMX complexes, and are reproduced by *ab initio* calculations. The large mass-independent stretching force constants obtained for XeCuF and XeCuCl imply a strong interaction between Xe and Cu. The XeCu force constant is larger than the value for KrCu and much larger than the value for ArCu. This indicates that the interaction strength increases as the noble gas is changed from Ar

to Kr to Xe. The XeCu force constant is larger than the corresponding XeAg value, however it is smaller than the corresponding XeAu value, implying that the interaction strength increases as the metal is changed from Ag to Cu to Au. For all NgMX molecules, the NgM force constants are larger than typical values for van der Waals complexes.

The XeCu dissociation energies obtained from *ab initio* calculations for XeCuF and XeCuCl are large and are approaching the value expected for a covalent bond. These large values cannot be fully accounted for by induction energies. Indeed, the dissociation energies calculated for all NgMX molecules are large, and none can be accounted for by induction energies. The dissociation energies clearly illustrate that the interaction strength increases as the noble gas is changed from Ar to Kr to Xe and as the metal is changed from Ag to Cu to Au. XeAuF has the largest dissociation energy of the NgMX molecules. van der Waals complexes have much smaller dissociation energies that can be more than fully accounted for by induction energies. The dissociation energies for the NgMX molecules have a directly proportional relationship with the experimental force constants assuming a Morse potential. Thus the experimental measurement of the rotational and centrifugal distortion constants is a rough, indirect measurement of the dissociation energy.

The nuclear quadrupole coupling constants obtained for ^{131}Xe, Cu and Cl in the XeCuX molecules are large and show a significant electron density rearrangement on molecule formation. The xenon nuclear quadrupole coupling constants of XeCuF and XeCuCl are much larger than those obtained for xenon-containing van der Waals complexes. The nuclear quadrupole coupling constant of xenon increases as the metal is changed from Ag to Cu to Au. The same trend is seen with the ^{83}Kr nuclear quadrupole coupling constants. For all KrMX and XeMX molecules, the difference between the nuclear quadrupole coupling constants for ^{83}Kr and ^{131}Xe in the atom and the NgMX molecule is very large and suggests a major rearrangement of electron distribution at the noble gas. This change is a large fraction of the difference between to

the nuclear quadrupole coupling constants for Kr^+ and Xe ($[Kr]4d^{10}5p^5 6s^1$) [Reference 102 and 101], respectively. The large values obtained for ^{83}Kr and ^{131}Xe cannot be explained purely by electrostatic interactions. This suggests that the bonding in NgMX molecules cannot be explained purely by van der Waals interactions.

The nuclear quadrupole coupling constants obtained for Cu and Cl increase in magnitude as the noble gas is changed from Ar to Kr to Xe. The same is true for the nuclear quadrupole coupling constants obtained for Au and Br in NgMX molecules. The fractional changes of the metal nuclear quadrupole coupling constants from the MX monomer values to the NgMX values are a significant percentage of the changes to the values of the XMX^- ions and the OCMX molecules [References 117 and 98], all covalently bound. The results suggest the electron distribution rearrangement could be due to the presence of some degree of covalent bonding.

The significant electron density rearrangement seen in the nuclear quadrupole coupling constants can also be seen in the *ab initio* Mulliken and NBO populations of XeCuF and XeCuCl. There is a considerable donation of electron density from the Xe to the Cu when the molecule is formed. The charges on the noble gas and the metal also change substantially. All NgMX molecules show the donation of electron density and the change in charges on molecule formation. The magnitude of the donations increase as the noble gas is changed from Ar to Kr to Xe and as the metal is changed from Ag to Cu to Au.

Visually, the sharing of electron density between the Xe to the Cu can be seen in the contours of electron density in valence molecular orbitals generated by MOLDEN. There is considerable orbital overlap between the Xe and the Cu atoms. The σ-sharing is greater than the π-sharing. These plots have been generated for most of the NgMX molecules[26-34] and the orbital overlap seems to increase roughly with the other properties, with XeAuF having the stongest interactions. The plots are consistent with the picture expected for covalently bonded molecules.

It should be noted that a colleague has been unable to construct plots with similar sharing for MOs for the van der Waals Ar-BeO and Ar-NaCl complexes.

The local energy densities for XeCuF and XeCuCl provide a strong indication of the presence of covalent bonding. The values at the bond critical point are negative and, according to Frenking and Cremer,[84] this indicates that a covalent bond is present between the Xe and the Cu. A negative value was expected because the *ab initio* dissociation energy was larger than the empirically calculated induction energy. The reported values of the local energy densities for NgMX molecules are all negative indicating covalent bonds are present in all of those molecules. The magnitudes of the values increase as the noble gas is changed from Ar to Kr to Xe and as the metal is changed from Ag to Cu to Au. By this criterion XeAuF is the most strongly bound while the Ag-containing molecules are weakly bound, but all are covalent.

Overall there is a strong, consistent body of evidence, both experimental and theoretical, that the NgMX molecules contain NgM covalent bonds. The most strongly bonded is XeAuF, with XeCuF and XeCuCl next in line. The fundamental properties of all the molecules are the same, with the variations being only a matter of degree. There is not a sudden change in any property as the noble gas or metal is changed, suggesting that all the molecules should show similar bonding. Since XeAuF, XeCuF and XeCuCl are covalently bonded, the inference is that all the molecules have some degree of NgM covalent bonding.

References

1 Gordy, W.; Cook, R. L. *Microwave Molecular Spectra No. XVIII in Techniques of Chemistry*, 3rd ed. Wiley-Interscience Publishers, New York, 1970.

2 Abraham, R. J.; Fisher, J.; Loftus, P. *Introduction to NMR spectroscopy*. John Wiley & Sons: Chicester. 1988.

3 Ekkers, J.; Flygare, W. H. *Rev. Sci. Instrum.* **1976**, *47*, 448.

4 Balle, T. J.; Flygare, W. H. *Rev. Sci. Instrum.* **1981**, *52*, 33.

5 Grabow, J.-U.; Stahl, W. *Z. Naturforsch. Teil A* **1990**, *45*, 1043.

6 Smalley, R. E.; Wharton, L.; Levy, D. H. *Acc. Chem. Res.* **1977**, *10*, 139.

7 Campbell, E. J.; Buxton L. W.; Keenan, M. R.; Flygare, W. H. *Phys. Rev. A.* **1981**, *24*, 812.

8 Iida, M.; Ohshima, Y.; Endo, Y. *J. Chem. Phys.* **1993**, *97*, 357.

9 Ngari, M. S.; Xu, Y.; Jäger, W. *Mol. Phys.* **2001**, *99*, 13.

10 Xu, Y.; Jäger, W.; Djauhari, J.; Gerry, M. C. L. *J. Chem. Phys.* **1995**, *103*, 2827.

11 Tang, J.; Xu, Y.; McKellar, A. R. W.; Jäger, W. *Science* **2002**, *297*, 2030.

12 Xu, Y.; Jäger, W. *J. Chem. Phys.* **2003**, *119*, 5457.

13 Walker, K. A. Ph. D. thesis, University of British Columbia, 1998.

14 Lin, W.; Evans, C. J.; Gerry, M. C. L. *Phys. Chem. Chem. Phys.* **2000**, *2*, 43.

15 Walker, K. A.; Gerry, M. C. L. *Chem. Phys. Lett.* **1997**, *9*, 278.

16 Walker, K. A.; Gerry, M. C. L. *J. Chem. Phys.* **1997**, *107*, 9835.

17 Beaton, S. A.; Gerry, M. C. L. *J. Chem. Phys.* **1999**, *110*, 10715.

18 Hensel, K. D.; Styger, C.; Jäger, W.; Merer, A. J.; Gerry, M. C. L. *J. Chem. Phys.* **1993**, *99*, 3320.

19 Evans, C. J.; Gerry, M. C. L. *J. Am. Chem. Soc.* **2000**, *122*, 1560.

20 Evans, C. J.; Gerry, M. C. L. *J. Mol. Spectrosc.* **2000**, *203*, 105.

21 Hoeft, J.; Lovas, F. J.; Tiemann, E.; Törring, T. *Z. Naturforsch.* **1970**, *25a*, 35.

22 Manson, E. L.; DeLucia, F. C.; Gordy, W. *J. Chem. Phys.* **1975**, *63*, 2724.

23 Brice, B. A. *Phys. Rev.* **1931**, *38*, 658.

24 Low, R. J.; Varberg, T. D.; Connelly, J. P.; Auty, A. R.; Howard, B. J.; Brown, J. M. *J. Mol. Spectrosc.* **1993**, *161*, 499.

25 Evans, C. J.; Gerry, M. C. L. *J. Chem. Phys.* **2000**, *112*, 1321.

26 Evans, C. J.; Gerry, M. C. L. *J. Chem. Phys.* **2000**, *112*, 9363.

27 Evans, C. J.; Rubinoff, D. S.; Gerry, M. C. L. *Phys. Chem. Chem. Phys.* **2000**, *2*, 3843.

28 Evans, C. J.; Lesarri, A.; Gerry, M. C. L. *J. Am. Chem. Soc.* **2000**, *122*, 6100.

29 Walker, N. R.; Reynard, L. M.; Gerry, M. C. L. *J. Mol. Struct.* **2002**, *612*, 109.

30 Reynard, L. M.; Evans, C. J.; Gerry, M. C. L. *J. Mol. Spectrosc.* **2001**, *206*, 33.

31 Thomas, J. M.; Walker, N. R.; Cooke, S. A.; Gerry, M. C. L. *J. Am. Chem. Soc.* **2004**, *126*, 1235.

32 Michaud, J. M.; Cooke, S. A.; Gerry, M. C. L. *Inorg. Chem.* **2004**, *43*, 3871.

33 Cooke, S. A.; Gerry, M. C. L. *Phys. Chem. Chem. Phys.* **2004**, *6*, 3248.

34 Cooke, S. A.; Gerry, M. C. L. Accepted to *J. Am. Chem. Soc.* **2004**

35 Bauschlicher, C. W., Jr.; Partridge, H.; Langhoff, S. R. *Chem. Phys. Lett.* **1990**, *165*, 272.

36 Pyykkö, P. *J. Am. Chem. Soc.* **1995**, *117*, 2067.

37 Lovallo, C. C.; Klobukowski, M. *Chem. Phys. Lett.* **2002**, *368*, 589.

38 Schröder, D.; Schwarz, H.; Hrušák, J.; Pyykkö, P. *Angew. Chem. Int. Ed. Engl.* **1994**, *33*, 212.

39 Bartlett, N. *Proc. Chem. Soc.* **1962**, *1962*, 218.

40 Graham, L.; Graudejus, O.; Jha, N. K.; Bartlett, N. *Coor. Chem. Rev.* **2000**, *197*, 321.

41 Petterson, M.; Lundell, J.; Räsänen, M. *Eur. J. Inorg. Chem.* **1999**, *1*, 729.

42 Christie, K. O. *Angew. Chem. Int. Ed.* **2001**, *40*, 1419.

43 Mizoguchi, A.; Endo, Y.; Ohshima, Y. *J. Chem. Phys.* **1998**, *109*, 10539.

44 Thompson, C. A.; Andrews, L. *J. Am. Chem. Soc.* **1994**, *116*, 423.

45 Ehlers, A. W.; Frenking, G.; Baerends, E. J. *Organometallics* **1997**, *16*, 4896.

46 Seidel, S.; Seppelt, K. *Science* **2000**, *290*, 117.

47 Drews, T.; Seidel, S.; Seppelt, K. *Angew. Chem. Int. Ed.* **2002**, *41*, 454.

48 Pyykkö, P. *Science* **2000**, *290*, 117.

49 Hwang, I.-C.; Seidel, S.; Seppelt, K. *Angew. Chem. Int. Ed. Engl.* **2003**, *42*, 4392.

50 Seppelt, K. *Z. Anorg. Allg. Chem.* **2003**, *629*, 2427.

51 Townes, C. H.; Schawlow, A. L. *Microwave Spectroscopy*, McGraw-Hill, New York, 1955.

52 Strandberg, M. W. P. *Microwave Spectroscopy*. Methuen Publishing, London, 1954. Chapter 1.

53 McQuarrie, D. A. *Quantum Chemistry*. University Science Books, California, 1983. Chapter 9.

54 Gordy, W.; Cook, R. L. *Microwave Molecular Spectra No. XVIII in Techniques of Chemistry*, 3rd ed. Wiley-Interscience Publishers, New York, 1970. Chapter IV.

55 Bernath, P. F. *Spectra of Atoms and Molecules*. Oxford University Press, Oxford, 1995. Chapter 6.

56 McQuarrie, D. A. *Quantum Chemistry*. University Science Books, California, 1983. Chapter 6.

57 McQuarrie, D. A. *Quantum Chemistry*. University Science Books, California, 1983. Chapter 10.

58 Zare, R. N. *Angular Momentum*. Wiley: New York, 1988.

59 Edmonds, A. R. *Angular Momentum in Quantum Mechanics*. Princeton: New Jersey , 1974.

60 Cook, R. L.; DeLucia, F. C. *Amer. J. Phys.* **1971**, *39*, 1433.

61 Slichter, C. P. *Principles of Magnetic Resonance*. Springer Verlag: Berlin, 1978.

62 Kroto, H. W. *Molecular Rotation Spectra*. John Wiley & Sons, London, 1975. Chapter 10.

63 Pickett, H. M. *J. Mol. Spectrosc.* **1991**, *148*, 371.

64 Allen, H. C. Jr.; Cross, P. C. *Molecular Vib-Rotors: The Theory and Interpretation of High Resolution Infrared Spectra*. Wiley & Sons, New York. 1963.

65 Rudolph, H. D. *Struct. Chem.* **1991**, *2*, 581.

66 Watson, J. K. G.; Roykburg, A.; Ulrich, W. *J. Mol. Spectrosc.* **1999**, *196*, 102.

67 Flygare, W. H. *Molecular Structure and Dynamics*, Prentice-Hall, New Jersey, 1978. p.423.

68 McGurk, J. C.; Schmalz, T. G.; Flygare, W. H. *Adv. Chem. Phys.* **1974**, *25*, 1.

69 Shea, J. A.; Read, W. G.; Campbell, E. J. *J. Chem. Phys.* **1983**, *79*, 2559.

70 Shoemaker, R. L. in *Laser and Coherent Spectroscopy*, Ed. J. I. Steinfeld, Plenum Press, New York, 1978. p.197

71 Dreizler, H. *Mol. Phys.* **1986**, *59*, 1.

72 Leskowitz, G. M., Ph. D. Thesis, California Institute of Technology, 2003.

73 Shoemaker, R. L. in *Laser and Coherent Spectroscopy*, Ed. J. I. Steinfeld, Plenum Press, New York, 1978. pp. 209-210.

74 Smalley, R. E.; Wharton, L.; Levy, D. H. *Acc. Chem. Res.* **1977**, *10*, 139.

75 Suenram, R. D. (301)-975-216, National Institute of Standards and Technology, July 1997.

76 Mills, I.; Cvitaš, T.; Homann, K.; Kallay, N.; Kuchitsu, K. *Quantities, Units and Symbols in Physical Chemistry*. Blackwell Scientific Publications. **1983**. Chapter 6.

77 Møller C.; Plesset, M. S. *Phys. Rev.* **1934**, *46*, 618.

78 Frisch, M. J.; Trucks, G. W.; Schlegel, H. B.; Scuseria, G. E.; Robb, M. A.; Cheeseman, J. R.; Zakrzewski, V. G.; Montgomery, J. A.; Stratmann, R. E.; Burant, J. C.; Dapprich, S.; Milliam, J. M.; Daniels, A. D.; Rudin, K. N.; Strain, M. C.; Farkas, O.; Tomasi, J.; Barone, V.; Cossi, M.; Cammi, R.; Mennucci, B.; Pomelli, C.; Adamo, C.; Clifford, S.;

Ochterski, J.; Peterson, G. A.; Ayala, P. Y.; Cui, Q.; Morokuma, K.; Malick, D. K.; Rabuck, A. D.; Raghavachari, K.; Foresman, J. B.; Cisolowski, J.; Ortiz, J. V.; Stefanov, B. B.; Liu, G.; Liashenko, A.; Piskorz, P.; Komaroni, I.; Gomperts, R.; Martin, R. L.; Fox, D. J.; Keith, T.; Al-Lahma, M. A.; Peng, C. Y.; Nanayakkara, A.; Gonzalez, C.; Challacombe, M.; Gill, P. M. W.; Johnson, B. G.; Chen, W.; Wong, M. W.; Andres, J. L.; Head-Gordon, M.; Replogle, E. S.; Pople, J. A. *Gaussian 98*, revision A.6; Gaussian Inc.: Pittsburgh PA, 1998.

79 Dobbs, K. D.; Hehere, W. J. *J. Comp. Chem.* **1986**, *7*, 359.

80 Petersson, G. A.; Benneth, A.; Tensfeldt, T. G.; Al-Laham, M. A.; Shirley, W. A.; Mantzaris, J. *J. Chem. Phys.* **1988**, *89*, 2193.

81 Andrae, D.; Häusermann, V.; Dolg, M.; Stoll, H.; Preus, H.; *Theor. Chim. Acta* **1990**, *27*, 213.

82 Antes, I.; Dapprich, S.; Frenking, G.; Schwerdtfeger, P. *Inorg. Chem.* **1996**, *35*, 2089.

83 McLean, A. D.; Chandler, G. S. *J. Chem. Phys.* **1980**, *72*, 5639.

84 Frenking, G.; Cremer, D. *Structure and Bonding* **1990**, *73*, 18-95.

85 Housecroft, C. E.; Sharpe, A. G. *Inorganic Chemistry*. Prentice Hall, 2001. Chapter 1.

86 Ohshima, Y.; Iida, M.; Endo, Y. J. Chem. Phys. **1990**, 92, 3990.

87 Buxton, L. W.; Campbell, E. J.; Keenan, M. R.; Balle, T. J.; Flygare, W. H. J. Chem. Phys. **1981**, 54, 173.

88 Baiocchi, F. A.; Dixon, T. A.; Joyner, C. H.; Klemperer, W. *J. Chem. Phys.* **1981**, *75*, 2041.

89 Bauschlicher, C. W., Jr.; Langhoff, S. R. *Chem. Phys. Lett.* **1989**, *158*, 409.

90 Bauschlicher, C. W., Jr.; Partridge, H.; Langhoff, S. R. *J. Chem. Phys.* **1989**, *91*, 4733.

91 Pyykkö, P. *P. Chem. Rev.* **1997**, *97*, 597.

92 Huheey, J. E.; Keiter, E. A.; Keiter, R. L. *Inorganic Chemistry, Principles of Structure and Reactivity*, 4th ed.; Harper-Collins: New York, 1993.

93 Bartlett, N.; Sladky, F. O. In *Comprehensive Inorganic Chemistry*; Bailar, J. C.; Emeléus, H. J.; Nyholm, R.; Trotman-Dickenson, A. F., Eds.; Pergamon: Oxford, 1973.

94 Pyykkö, P. *Chem. Rev.* **1988**, *88*, 579.

95 Thomas, J. M. B. Sc. Honours Thesis. University of British Columbia (2002)

96 Bowmaker, G. A.; Brockliss, L. D.; Whiting, R. *Aust. J. Chem.* **1973**, *26*, 29.

97 Bowmaker, G. A.; Boyd, P. D. W.; Sorrensen, R. J. *J. Chem. Soc., Faraday Trans. 2* **1985**, *81*, 1627.

98 Walker, N. R.; Gerry, M. C. L. *Inorg. Chem.* **2001**, *40*, 6158.

99 Evans, C. J.; Reynard, L. M.; Gerry, M. C. L. *Inorg. Chem.* **2001**, *40*, 6123.

100 Xu, Y.; Jäger, W.; Gerry, M. C. L. *J. Chem. Phys.* **1993**, *99*, 919.

101 Faust, W. L.; McDermott, M. N. *Phys. Rev.* **1961**, *123*, 198.

102 Holloway, J. H.; Schrobilgen, G. J.; Bukshpan, S.; Hilbrants, W.; deWaard, H. *J. Chem. Phys.* **1997**, *66*, 2627.

103 Foley, H. M.; Sternheimer, R. M.; Tycko, D. *Phys. Rev.* **1954**, *93*, 734 and references therein.

104 Fowler, P. W.; Lasseretti, P.; Steiner, E.; Zanasi, R. *Chem. Phys.* **1989**, *133*, 121.

105 Fowler, P. W. *Chem. Phys.* **1989**, *156*, 494.

106 Keenan, M. R.; Buxton, L. W.; Campbell, E. J.; Balle, T. J.; Flygare, W. H. *J. Chem. Phys.* **1980**, *73*, 3523.

107 Feiock, F. D.; Johnson, W. R. *Phys. Rev.* **1969**, *187*, 39.

108 Hoeft, J.; Lovas, F. J.; Tiemann, E.; Törring, T. *Z. Naturforsch.* **1971**, *26a*, 240.

109 Harris, S. J.; Novick, S. E.; Klemperer, W. *J. Chem. Phys.* **1974**, *60*, 3208.

110 Pyykkö, P. *Chem. Rev.* **1988**, *88*, 579.

111 Manson, E. L.; DeLucia, F. C.; Gordy, W. *J. Chem. Phys.* **1975**, *62*, 1042.

112 Manson, E. L.; DeLucia, F. C.; Gordy, W. *J. Chem. Phys.* **1975**, *63*, 2724.

113 Barrow, R. F.; Clements, R. M. *Proc. R. Soc. London, Ser. A* **1971**, *322*, 243.

114 Brice, B. *Phys. Rev.* **1931**, *35*, 960.

115 Brice, B. *Phys. Rev.* **1931**, *38*, 658.

116 Andreev, S.; Bel Bruno, J. J. *Chem. Phys. Lett.* **2000**, *329*, 490.

117 Bowmaker, G. A.; Boyd, P. D. W.; Sorrenson, R. J. *J. Chem. Soc. Faraday Trans. 2* **1985**, *81*, 1627.

118 Campbell, E. J.; Buxton, L. W.; Keenan, M. R.; Flygare, W. H. *Phys. Rev. A: At. Mol. Opt. Phys.* **1981**, *24*, 812.

119 Warner, H. E.; Conner, W. T.; Woods, R. C. *J. Chem. Phys.* **1984**, *81*, 5413.

120 Peterson, K. A.; Petrmichl, R. H.; McClain, R. L.; Woods, R. C. *J. Chem. Phys.* **1991**, *95*, 2352.

121 Pyykkö, P. *Molec. Phys.* **2001**, *99*, 1617.

122 Gaussian 03, Revision B.5, Frisch, M. J.; Trucks, G. W.; Schlegel, H. B.; Scuseria, G. E.; Robb, M. A.; Cheeseman, J. R.; Montgomery, Jr., J. A.; Vreven, T.; Kudin, K. N.; Burant, J. C.; Millam, J. M.; Iyengar, S. S.; Tomasi, J.; Barone, V.; Mennucci, B.; Cossi, M.; Scalmani, G.; Rega, N.; Petersson, G. A.; Nakatsuji, H.; Hada, M.; Ehara, M.; Toyota, K.; Fukuda, R.; Hasegawa, J.; Ishida, M.; Nakajima, T.; Honda, Y.; Kitao, O.; Nakai, H.; Klene, M.; Li, X.; Knox, J. E.; Hratchian, H. P.; Cross, J. B.; Bakken, V.; Adamo, C.; Jaramillo, J.; Gomperts, R.; Stratmann, R. E.; Yazyev, O.; Austin, A. J.; Cammi, R.; Pomelli, C.; Ochterski, J. W.; Ayala, P. Y.; Morokuma, K.; Voth, G. A.; Salvador, P.; Dannenberg, J. J.; Zakrzewski, V. G.; Dapprich, S.; Daniels, A. D.; Strain, M. C.; Farkas, O.; Malick, D. K.; Rabuck, A. D.; Raghavachari, K.; Foresman, J. B.; Ortiz, J. V.; Cui, Q.; Baboul, A. G.; Clifford, S.; Cioslowski, J.; Stefanov, B. B.; Liu, G.;

Liashenko, A.; Piskorz, P.; Komaromi, I.; Martin, R. L.; Fox, D. J.; Keith, T.; Al-Laham, M. A.; Peng, C. Y.; Nanayakkara, A.; Challacombe, M.; Gill, P. M. W.; Johnson, B.; Chen, W.; Wong, M. W.; Gonzalez, C.; and Pople, J. A.; Gaussian, Inc., Wallingford CT, 2004.

123 http://www.theochem.uni-stuttgart.de/pseudopotentials. **2003**, Pseudopotentials of the Stuttgart/Köln group.

124 Nicklass, A.; Dolg, M.; Stoll, H.; Preuss, H. *J. Chem. Phys.* **1995**, *102*, 8942.

125 Boys, S. F.; Bernardi, F. *Mol. Phys.* **1970**, *19*, 553.

126 Levine, I. N. *Quantum Chemistry.* 5th ed. Prentice Hall; New Jersey. 2000. Chapter 17.

127 Berry, R. S.; Rice, S. A.; Ross, J. *The Structure of Matter: An Introduction to Quantum Mechanics*, 2nd ed.; Oxford: New York, 2002.

128 Bellert, D.; Breckenridge, W. H. *Chem. Rev.* **2002**, *102*, 1595.

129 Levine, I. N. *Quantum Chemistry.* 5th ed. Prentice Hall; New Jersey. 2000. Chapter 15.

130 Schaftenaar, G. *MOLDEN 3.4,* CAOS/CAMM Center, The Netherlands, 1998.

131 Cremer, D.; Kraka, E. *Angew. Chem.* **1984**, *96*, 612; see also Cremer, D.; Kraka, E. *Angew. Chem. Int. Ed. Engl.* **1984**, *23*, 627.

132 Cremer, D.; Kraka, E. *Croat. Chem. Acta* **1984**, *57*, 1259.

133 Bader, R. F. W. *www.chemistry.mcmaster.ca/aimpac* **1995**.

134 Nair, K. P. R.; Hoeft, J. *J. Phys. B: At. Mol. Phys.* **1984**, *17*, 735.

135 Nair, K. P. R.; Hoeft, J. *J. Chem. Phys. Lett.* **1982**, *102*, 438.

136 Hebert, A. J.; Lovas, F. J.; Melendres, C. J.; Hollowell, C. D.; Story, T. L.; Street, K. *J. Chem. Phys.* **1968**, *48*, 2824.

137 Deleeuw, F. H.; Van Wachem, R.; Dymanus, A. *J. Chem. Phys.* **1969**, *50*, 1393.

Appendix A

Quantum number assignments and Transition Frequencies for XeCuF

Table A.1: Quantum number assignments and transition frequencies in MHz for $^{129}Xe^{63}CuF$

J' – J"	F' – F"	Frequency (MHz)	Obs. – Calc. (kHz)
4-3	11/2-9/2	9009.1338	-2.5
4-3	9/2-7/2	9009.1338	2.5
4-3	7/2-5/2	9010.5026	0.1
4-3	5/2-3/2	9010.5026	0.7
5-4	13/2-11/2	11261.5783	-3.9
5-4	11/2-9/2	11261.5783	0.8
5-4	9/2-7/2	11262.3861	-0.5
5-4	7/2-5/2	11262.3861	2.3
6-5	15/2-13/2	13513.9565	-2.6
6-5	13/2-11/2	13513.9565	1.9
6-5	11/2-9/2	13514.4909	-1.2
6-5	9/2-7/2	13514.4909	2.3

Table A.2: Quantum number assignments and transition frequencies in MHz for $^{132}Xe^{63}CuF$

J' – J"	F' – F"	Frequency (MHz)	Obs. – Calc. (kHz)
4-3	11/2-9/2	8937.4819	-2.4
4-3	9/2-7/2	8937.4819	2.7
4-3	7/2-5/2	8938.8555	-0.3
4-3	5/2-3/2	8938.8555	0.3
5-4	13/2-11/2	11172.0171	-2.4
5-4	11/2-9/2	11172.0171	2.4
5-4	9/2-7/2	11172.8252	-1.7
5-4	7/2-5/2	11172.8252	1.0
6-5	15/2-13/2	13406.4845	-2.0
6-5	13/2-11/2	13406.4845	2.5
6-5	11/2-9/2	13407.0203	-1.3
6-5	9/2-7/2	13407.0203	2.2
7-6	17/2-15/2	15640.8986	-3.2
7-6	15/2-13/2	15640.8986	1.2
7-6	13/2-11/2	15641.2813	-1.7
7-6	11/2-9/2	15641.2813	2.2
9-8	19/2-17/2	20109.5906	-2.5
9-8	17/2-15/2	20109.5906	1.9
9-8	15/2-13/2	20109.8126	-1.4
9-8	13/2-11/2	20109.8126	2.7

10-9	23/2-21/2	22343.8663	-1.3
10-9	21/2-19/2	22343.8663	3.1
10-9	19/2-17/2	22344.0404	-3.1
10-9	17/2-15/2	22344.0404	1.0

Table A.3: Quantum number assignments and transition frequencies in MHz for $^{134}Xe^{63}CuF$

J' – J"	F' – F"	Frequency (MHz)	Obs. – Calc. (kHz)
4-3	11/2-9/2	8891.3936	-2.7
4-3	9/2-7/2	8891.3936	2.4
4-3	7/2-5/2	8892.7671	-0.9
4-3	5/2-3/2	8892.7671	-0.4
5-4	13/2-11/2	11114.4080	-2.4
5-4	11/2-9/2	11114.4080	2.3
5-4	9/2-7/2	11115.2179	-0.1
5-4	7/2-5/2	11115.2179	2.6
6-5	15/2-13/2	13337.3546	-2.4
6-5	13/2-11/2	13337.3546	2.2
6-5	11/2-9/2	13337.8900	-2.1
6-5	9/2-7/2	13337.8900	1.4

Table A.4: Quantum number assignments and transition frequencies in MHz for $^{136}Xe^{63}CuF$

J' – J"	F' – F"	Frequency (MHz)	Obs. – Calc. (kHz)
4-3	11/2-9/2	8846.6025	-2.4
4-3	9/2-7/2	8846.6025	2.6
4-3	7/2-5/2	8847.9730	-0.5
4-3	5/2-3/2	8847.9730	0.0
5-4	13/2-11/2	11058.4178	-2.7
5-4	11/2-9/2	11058.4178	2.0
5-4	9/2-7/2	11059.2254	-0.9
5-4	7/2-5/2	11059.2254	1.9
6-5	15/2-13/2	13270.1666	-2.1
6-5	13/2-11/2	13270.1666	2.5
6-5	11/2-9/2	13270.7006	-2.0
6-5	9/2-7/2	13270.7006	1.5

Table A.5: Quantum number assignments and transition frequencies in MHz for $^{129}Xe^{65}CuF$

J' – J"	F' – F"	Frequency (MHz)	Obs. – Calc. (kHz)
4-3	11/2-9/2	8939.4746	-3.2
4-3	9/2-7/2	8939.4746	2.0
4-3	7/2-5/2	8940.7412	-1.1
4-3	5/2-3/2	8940.7412	0.3
5-4	13/2-11/2	11174.4934	-1.0
5-4	11/2-9/2	11174.4934	4.0
5-4	9/2-7/2	11175.2367	-1.7
5-4	7/2-5/2	11175.2367	1.6
6-5	15/2-13/2	13409.4416	-3.8
6-5	13/2-11/2	13409.4416	1.0
6-5	11/2-9/2	13409.9369	-1.1
6-5	9/2-7/2	13409.9369	2.8

Table A.6: Quantum number assignments and transition frequencies in MHz for $^{132}Xe^{65}CuF$

J' – J"	F' – F"	Frequency (MHz)	Obs. – Calc. (kHz)
4-3	11/2-9/2	8867.3195	-3.4
4-3	9/2-7/2	8867.3195	1.9
4-3	7/2-5/2	8868.5895	-1.3
4-3	5/2-3/2	8868.5895	0.1
5-4	13/2-11/2	11084.3018	-1.5
5-4	11/2-9/2	11084.3018	3.5
5-4	9/2-7/2	11085.0487	-0.6
5-4	7/2-5/2	11085.0487	2.6
6-5	15/2-13/2	13301.2165	-3.0
6-5	13/2-11/2	13301.2165	1.9
6-5	11/2-9/2	13301.7112	-2.1
6-5	9/2-7/2	13301.7112	1.8

Table A.7: Quantum number assignments and transition frequencies in MHz for $^{131}Xe^{63}CuF$

J' – J"	F_1' – F_1"	F' – F"	Frequency (MHz)	Obs – Calc. (kHz)
4-3	9/2-7/2	6-5	8961.3690	-2.8
4-3	7/2-7-2	5-4	8961.5122	-1.4
4-3	11/2-9/2	4-3	8961.6655	5.3
4-3	11/2-9/2	7-6	8961.6739	3.2
4-3	11/2-9/2	6-5	8961.9618	-1.4
4-3	11/2-9/2	5-4	8962.3593	0.6
5-4	9/2-7/2	3-2	11200.5701	4.6
5-4	7/2-5/2	4-3	11200.7082	-1.3
5-4	11/2-9/2	6-5	11201.1957	-3.7
5-4	9/2-7/2	5-4	11201.2350	-2.4
5-4	9/2-7/2	6-5	11201.2971	-1.2
5-4	11/2-9/2	7-6	11201.7068	-1.2
6-5	9/2-7/2	5-4	13441.2409	-0.6
6-5	11/2-9/2	4-3	13441.3277	4.1
6-5	11/2-9/2	7-6	13441.4978	1.5
6-5	11/2-9/2	6-5	13441.6088	1.6
6-5	11/2-9/2	5-4	13441.6685	-0.3
6-5	13/2-11/2	7-6	13441.8089	0.6
6-5	13/2-11/2	8-7	13441.9811	-10.9
6-5	15/2-13/2	9-8	13442.0977	0.3

6-5	15/2-13/2	6-5	13442.1817	3.0
6-5	15/2-13/2	8-7	13442.1970	-0.7
6-5	13/2-11/2	5-4	13442.4289	2.0
6-5	15/2-13/2	7-6	13442.5109	1.4

Appendix B

Quantum number assignments and Transition Frequencies for XeCuCl

Table B.1: Quantum number assignments and transition frequencies in MHz for $^{129}Xe^{63}Cu^{35}Cl$

J' – J"	F_1' – F_1"	F' – F"	Frequency (MHz)	Obs. – Calc. (kHz)
6-5	15/2-13/2	7-6	9087.3256	2.6
6-5	15/2-13/2	8-7	9087.5015	3.8
6-5	15/2-13/2	6-5	9087.5103	-8.2
6-5	15/2-13/2	9-8	9087.5567	4.5
6-5	13/2-11/2	8-7	9087.6083	2.0
6-5	11/2-9/2	6-5	9087.7293	0.3
6-5	11/2-9/2	7-6	9087.8560	-0.7
6-5	11/2-9/2	4-3	9087.8836	0.0
7-6	17/2-15/2	9-8	10602.1085	5.5
7-6	17/2-15/2	10-9	10602.1434	4.2
7-6	15/2-13/2	9-8	10602.1770	1.8
7-6	17/2-15/2	8-7	10601.9529	-9.1
7-6	15/2-13/2	6-5	10601.9657	-12.8
7-6	13/2-11/2	8-7	10602.3933	-1.5
7-6	11/2-9/2	6-5	10602.4403	2.9
7-6	11/2-9/2	7-6	10602.6432	-1.2
8-7	17/2-15/2	8-7	12116.4436	1.5

8-7	19/2-17/2	9-8	12116.5711	2.5
8-7	17/2-15/2	7-6	12116.5811	2.8
8-7	19/2-17/2	11-10	12116.7134	4.9
8-7	17/2-15/2	9-8	12116.7344	0.4
8-7	15/2-13/2	7-6	12116.7938	-3.1
8-7	15/2-13/2	8-7	12116.8308	1.6
8-7	15/2-13/2	9-8	12116.9196	1.4
8-7	13/2-11/2	7-6	12116.9387	-2.4
8-7	13/2-11/2	8-7	12117.0819	-1.1
9-8	19/2-17/2	9-8	13631.0561	0.8
9-8	19/2-17/2	8-7	13631.1540	0.8
9-8	21/2-19/2	9-8	13631.2281	4.6
9-8	21/2-19/2	12-11	13631.2550	-4.9
9-8	19/2-17/2	11-10	13631.2765	-1.6
9-8	17/2-15/2	9-8	13631.3625	0.1
9-8	17/2-15/2	10-9	13631.4312	1.3
9-8	15/2-13/2	9-8	13631.5463	-1.0

Table B.2: Quantum number assignments and transition frequencies in MHz for $^{132}Xe^{63}Cu^{35}Cl$

J' – J"	F_1' – F_1"	F' – F"	Frequency (MHz)	Obs. – Calc. (kHz)
5-4	13/2-11/2	6-5	7508.9290	-1.1
5-4	11/2-9/2	4-3	7508.9919	-1.2
5-4	13/2-11/2	7-6	7509.1405	0.4
5-4	13/2-11/2	5-4	7509.2082	1.5
5-4	13/2-11/2	8-7	7509.2283	1.0
5-4	11/2-9/2	7-6	7509.3139	-0.2
5-4	9/2-7/2	5-4	7509.4496	-0.1
5-4	11/2-9/2	6-5	7509.4701	3.7
5-4	9/2-7/2	6-5	7509.5466	-2.3
5-4	7/2-5/2	4-3	7509.7527	-1.0
5-4	9/2-7/2	3-2	7509.8062	2.3
6-5	13/2-11/2	6-5	9010.5853	-3.0
6-5	15/2-13/2	7-6	9010.8617	0.4
6-5	13/2-11/2	5-4	9010.8903	-1.2
6-5	15/2-13/2	8-7	9011.0378	2.5
6-5	15/2-13/2	9-8	9011.0916	2.0
6-5	13/2-11/2	8-7	9011.1440	0.4
6-5	13/2-11/2	7-6	9011.1904	0.8
6-5	11/2-9/2	6-5	9011.2632	-1.4
6-5	11/2-9/2	7-6	9011.3912	-1.6

6-5	11/2-9/2	4-3	9011.4197	0.8
6-5	9/2-7/2	5-4	9011.4929	12.6
7-6	15/2-13/2	7-6	10512.5743	-1.3
7-6	17/2-15/2	8-7	10512.7565	0.0
7-6	17/2-15/2	9-8	10512.8980	1.0
7-6	17/2-15/2	10-9	10512.9332	0.1
7-6	15/2-13/2	9-8	10512.9679	-1.1
7-6	15/2-13/2	8-7	10512.9837	3.0
7-6	13/2-11/2	5-4	10513.1460	0.0
7-6	11/2-9/2	6-5	10513.2250	-4.5
7-6	11/2-9/2	7-6	10513.4343	-1.7
8-7	17/2-15/2	8-7	12014.4922	-1.1
8-7	19/2-17/2	9-8	12014.6190	-0.6
8-7	17/2-15/2	7-6	12014.6323	3.0
8-7	19/2-17/2	11-10	12014.7638	4.7
8-7	17/2-15/2	10-9	12014.7841	0.0
8-7	13/2-11/2	7-6	12014.8530	-1.1
8-7	15/2-13/2	8-7	12014.8771	-1.5
8-7	15/2-13/2	9-8	12014.9673	-0.4
8-7	13/2-11/2	7-6	12014.9804	-9.9
8-7	13/2-11/2	8-7	12015.1302	-1.7
9-8	19/2-17/2	9-8	13516.3615	-1.8
9-8	19/2-17/2	8-7	13516.4601	-1.0
9-8	21/2-19/2	9-8	13516.5313	0.0

9-8	21/2-19/2	12-11	13516.5628	-4.6
9-8	19/2-17/2	11-10	13516.5893	3.7
9-8	17/2-15/2	9-8	13516.6654	-3.6
9-8	15/2-13/2	9-8	13516.8499	-3.6
10-9	21/2-19/2	10-9	15018.1973	1.1
10-9	23/2-21/2	11-10	15018.2671	2.5
10-9	23/2-21/2	10-9	15018.3258	2.7
10-9	21/2-19/2	12-11	15018.3776	7.0
10-9	17/2-15/2	7-6	15018.4207	4.1
10-9	19/2-17/2	8-7	15018.4387	-2.9
10-9	19/2-17/2	10-9	15018.4450	0.5
10-9	17/2-15/2	10-9	15018.5787	-4.2

Table B.3: Quantum number assignments and transition frequencies in MHz for $^{134}Xe^{63}Cu^{35}Cl$

J' – J"	F_1' – F_1"	F' – F"	Frequency (MHz)	Obs. – Calc. (kHz)
7-6	15/2-13/2	7-6	10455.1420	-2.3
7-6	17/2-15/2	8-7	10455.3242	0.5
7-6	17/2-15/2	9-8	10455.4661	2.6
7-6	15/2-13/2	9-8	10455.5356	0.2
7-6	13/2-11/2	8-7	10455.7540	0.1
7-6	11/2-9/2	6-5	10455.7944	-2.2
7-6	11/2-9/2	7-6	10456.0031	1.3
8-7	17/2-15/2	8-7	11948.8567	-2.7
8-7	19/2-17/2	9-8	11948.9835	-0.9
8-7	17/2-15/2	7-6	11948.9940	-0.2
8-7	19/2-17/2	11-10	11949.1259	2.6
8-7	17/2-15/2	10-9	11949.1470	-1.3
8-7	15/2-13/2	7-6	11949.2183	6.4
8-7	15/2-13/2	8-7	11949.2421	-2.1
8-7	15/2-13/2	9-8	11949.3312	-0.9
8-7	13/2-11/2	8-7	11949.4944	-1.1
9-8	21/2-19/2	10-9	13442.6193	1.0
9-8	17/2-15/2	9-8	13442.8378	4.8
9-8	15/2-13/2	9-8	13443.0103	-5.6

Table B.4: Quantum number assignments and transition frequencies in MHz for $^{136}Xe^{63}Cu^{35}Cl$

J' – J"	F_1' – F_1"	F' – F"	Frequency (MHz)	Obs. – Calc. (kHz)
7-6	15/2-13/2	7-6	10399.2882	1.8
7-6	17/2-15/2	9-8	10399.6081	0.05
7-6	17/2-15/2	10-9	10399.6397	-4.3
7-6	13/2-11/2	5-4	10399.8495	-5.3
7-6	11/2-9/2	6-5	10399.9464	7.8
8-7	17/2-15/2	8-7	11885.0206	-0.4
8-7	19/2-17/2	9-8	11885.1489	1.4
8-7	19/2-17/2	11-10	11885.2898	3.1
8-7	17/2-15/2	10-9	11885.3111	-0.6
8-7	15/2-13/2	7-6	11885.3701	-3.0
8-7	15/2-13/2	9-8	11885.4940	-0.2
8-7	13/2-11/2	8-7	11885.6578	-0.4
9-8	19/2-17/2	9-8	13370.7037	-4.9
9-8	21/2-19/2	10-9	13370.8056	5.3
9-8	17/2-15/2	8-7	13370.9868	6.3
9-8	17/2-15/2	9-8	13371.0114	-1.1
9-8	15/2-13/2	9-8	13371.1915	-5.6

Table B.5: Quantum number assignments and transition frequencies in MHz for $^{129}Xe^{65}Cu^{35}Cl$

J' – J"	F_1' – F_1"	F' – F"	Frequency (MHz)	Obs. – Calc. (kHz)
8-7	17/2-15/2	8-7	12074.2798	0.3
8-7	17/2-15/2	7-6	12074.4253	2.5
8-7	19/2-17/2	8-7	12074.5228	-2.0
8-7	19/2-17/2	10-9	12074.5329	3.2
8-7	17/2-15/2	10-9	12074.5782	-0.3
8-7	15/2-13/2	8-7	12074.6475	-1.7
8-7	15/2-13/2	6-5	12074.6875	3.8
8-7	15/2-13/2	9-8	12074.7468	-3.2
8-7	13/2-11/2	8-7	12074.9140	-2.5
9-8	19/2-17/2	9-8	13583.6241	-2.3
9-8	21/2-19/2	10-9	13583.7235	-1.9
9-8	19/2-17/2	8-7	13583.7292	-1.1
9-8	21/2-19/2	9-8	13583.8087	0.2
9-8	21/2-19/2	11-10	13583.8247	4.8
9-8	21/2-19/2	12-11	13583.8312	-6.5
9-8	19/2-17/2	11-10	13583.8585	3.1
9-8	17/2-15/2	8-7	13583.8910	-2.8
9-8	17/2-15/2	7-6	13583.9327	0.0
9-8	17/2-15/2	10-9	13584.0049	6.5

Table B.6: Quantum number assignments and transition frequencies in MHz for $^{132}Xe^{65}Cu^{35}Cl$

J' – J"	F_1' – F_1"	F' – F"	Frequency (MHz)	Obs. – Calc. (kHz)
7-6	15/2-13/2	7-6	10475.0767	-2.3
7-6	17/2-15/2	8-7	10475.2722	-1.3
7-6	15/2-13/2	6-5	10475.2863	0.0
7-6	17/2-15/2	9-8	10475.4156	0.9
7-6	17/2-15/2	10-9	10475.4493	-0.3
7-6	15/2-13/2	9-8	10475.4838	-0.5
7-6	13/2-11/2	7-6	10475.5585	2.4
7-6	13/2-11/2	5-4	10475.6339	2.4
7-6	13/2-11/2	8-7	10475.6870	-0.1
7-6	11/2-9/2	6-5	10475.7187	-0.1
7-6	11/2-9/2	7-6	10475.9335	-0.8
8-7	17/2-15/2	8-7	11971.6404	-0.3
8-7	19/2-17/2	9-8	11971.7779	-0.1
8-7	17/2-15/2	7-6	11971.7859	0.5
8-7	19/2-17/2	10-9	11971.8961	3.3
8-7	17/2-15/2	9-8	11971.9358	-0.4
8-7	15/2-13/2	8-7	11972.0036	-4.0
8-7	15/2-13/2	6-5	11972.0437	0.6
8-7	15/2-13/2	9-8	11972.1103	-0.4
8-7	13/2-11/2	7-6	11972.1305	2.8

8-7	13/2-11/2	8-7	11972.2753	-2.4
9-8	19/2-17/2	9-8	13468.1547	-0.1
9-8	21/2-19/2	10-9	13468.2592	3.9
9-8	21/2-19/2	9-8	13468.3402	0.3
9-8	21/2-19/2	12-11	13468.3613	-6.4
9-8	19/2-17/2	11-10	13468.3891	3.8
9-8	17/2-15/2	10-9	13468.5249	-1.4

Table B.7: Quantum number assignments and transition frequencies in MHz for $^{132}Xe^{63}Cu^{37}Cl$

J' – J"	F_1' – F_1"	F' – F"	Frequency (MHz)	Obs. – Calc. (kHz)
8-7	17/2-15/2	8-7	11671.1812	-2.3
8-7	19/2-17/2	9-8	11671.2661	0.9
8-7	19/2-17/2	10-9	11671.3546	0.6
8-7	17/2-15/2	9-8	11671.4141	0.9
8-7	13/2-11/2	6-5	11671.4551	-1.2
8-7	15/2-13/2	8-7	11671.5373	2.3
8-7	15/2-13/2	9-8	11671.5732	-1.6
8-7	13/2-11/2	7-6	11671.6099	0.7
8-7	13/2-11/2	8-7	11671.7069	-0.2
9-8	21/2-19/2	10-9	13130.1826	1.9
9-8	21/2-19/2	9-8	13130.2279	-0.6
9-8	15/2-17/2	7-6	13130.3369	-1.1
9-8	17/2-15/2	8-7	13130.3649	2.2
9-8	17/2-15/2	9-8	13130.4004	-1.0
9-8	17/2-15/2	10-9	13130.4344	-1.5

Table B.8: Quantum number assignments and transition frequencies in MHz for $^{131}Xe^{63}Cu^{35}Cl$

J' – J"	F_1' – F_1"	F_2' – F_2"	F' – F"	Frequency (MHz)	Obs – Calc. (kHz)
6-5	13/2-11/2	7-6	17/2-15/2	9036.4805	0.9
6-5	15/2-13/2	8-7	17/2-15/2	9036.4972	2.5
6-5	15/2-13/2	9-8	21/2-19/2	9036.5251	-3.4
8-7	13/2-11/2	8-7	17/2-15/2	12047.6464	-2.7
8-7	13/2-11/2	8-7	19/2-17/2	12047.8177	-2.3
8-7	15/2-13/2	9-8	19/2-17/2	12047.9815	9.0
8-7	19/2-17/2	11-10	21/2-19/2	12048.2695	-10.8
8-7	19/2-17/2	11-10	23/2-21/2	12048.3588	5.1
8-7	19/2-17/2	10-9	17/2-15/2	12048.3750	1.8
8-7	19/2-17/2	10-9	21/2-19/2	12048.3934	-12.1
8-7	19/2-17/2	11-10	25/2-23/2	12048.4322	9.2
8-7	17/2-15/2	9-8	21/2-19/2	12048.4600	-3.2
8-7	19/2-17/2	10-9	23/2-21/2	12048.4851	0.3
8-7	19/2-17/2	9-8	17/2-15/2	12048.4959	2.8
8-7	19/2-17/2	8-7	19/2-17/2	12048.5537	4.3
8-7	19/2-17/2	9-8	21/2-19/2	12048.6289	4.1
8-7	17/2-15/2	8-7	19/2-17/2	12048.7823	-3.2
8-7	17/2-15/2	7-6	17/2-15/2	12048.8190	-2.3